Relaxation Dynamics of the Two-Dimensional q-State Potts Model:

a contribution to the description of non-equilibrium properties in first-order phase transitions

Ezequiel Ferrero

Advisor: Sergio A. Cannas

Submitted to the Faculty of Mathematics, Astronomy and Physics as partial fulfillment of the requirements for the degree of Doctor in Physics of the

Universidad Nacional de Córdoba

March 2011

©FaMAF - UNC 2011

Abstract

We analyze the two-dimensional q-state Potts model, a paradigmatic model in the study of the Statistical Mechanics of Critical Phenomena and Phase Transitions, which exhibits temperature-driven magnetic phase transitions of first order ($q > 4$) and second order ($q \leq 4$), and which has demonstrated a remarkably rich dynamical phenomenology. We work primarily with Monte Carlo numerical simulations, for which we have implemented a variety of algorithmic techniques, both traditional and novel, including an implementation designed to run on graphics processing units (GPUs). Nevertheless, we also present analytical results in those cases where such an approach has been feasible.

We study Short-Time Dynamics (STD) within the Mean-Field approximation for the 2-state Potts model (the Curie–Weiss model) by solving exactly the Fokker–Planck equation associated with Glauber dynamics. We obtain closed-form expressions for the first moments of the order parameter, both near the critical point and near the spinodal points, starting from different initial conditions. We confirm the validity of the short-time dynamical scaling hypothesis in both cases.

We demonstrate that it is possible to define the spinodal point through the short-time dynamical behavior of the system, and that our definition applies equally to mean-field systems and to systems with short-range interactions. We study the metastability associated with the first-order phase transition in the q-state Potts model for $q > 4$. We show that the spinodal point is clearly separated from the transition point for all $q > 4$, thereby delimiting a temperature interval capable of sustaining metastable states. We provide numerical evidence for the existence of such metastable states associated with the first-order phase transition, and analyze the relaxation mechanism from these states to equilibrium.

We conduct a systematic study of the nonequilibrium dynamics of the Potts model on the square lattice following a quench from infinite temperature to subcritical temperatures. We analyze the long-time behavior of the energy and the relaxation time over a wide range of quench temperatures and system sizes. For $q > 4$ we identify the existence of distinct dynamical regimes depending on the temperature range. We characterize these regimes and the corresponding states of the system, and analyze in detail the finite-size scaling properties of the various relaxation times involved, as well as their temperature dependence.

Keywords: Relaxational dynamics, Potts model, Numerical Simulations, GPU computing (GPGPU), Metastable States, Spinodal points, Short-Time Dynamics, Fokker–Planck equation, Phase transitions, Non-equilibrium Statistical Mechanics.

PACS: 05.10.Gg, 05.10.Ln, 05.50.+q, 05.70.Fh, 75.10.Hk, 75.40.Cx, 75.60.Ch.

Publications Associated with This Thesis

The majority of the results presented in this thesis have been submitted for publication in international peer-reviewed journals.

The following works, listed in reverse chronological order, constitute the basis of this thesis:

- [1] E. E. Ferrero, J. P. De Francesco, N. Wolovick and S. A. Cannas
  "q-state Potts model metastability study using optimized GPU-based Monte Carlo algorithms", arXiv:1101.0876, submitted to *Computer Physics Communications* (2011).

- [2] C. Anteneodo, E. E. Ferrero, and S. A. Cannas
  "Short-time dynamics of finite-size mean-field systems"
  J. Stat. Mech. P07026 (2010).

- [3] E. S. Loscar, E. E. Ferrero, T. S. Grigera and S. A. Cannas
  "Nonequilibrium characterization of spinodal points using short time dynamics"
  J. Chem. Phys. **131**, 024120 (2009).

- [4] E. E. Ferrero and S. A. Cannas
  "Long-term ordering kinetics of the two-dimensional q-state Potts model"
  Phys. Rev. E **76**, 031108 (2007).

- [5] M. I. de Berganza, E. E. Ferrero, S. A. Cannas, V. Loreto and A. Petri
  "Phase separation of the Potts model in the square lattice"
  Eur. Phys. J. Special Topics **143**, 273 (2007).

Contents

Abstract **ii**

Publications Associated with This Thesis **iii**

Table of Contents **viii**

1 Introduction **1**

I Theoretical Framework **7**

2 First-Order Phase Transitions **9**
2.1 General characteristics 10
2.1.1 Classification 10
2.1.2 Order parameter 11
2.1.3 Phenomenology 12
2.2 Analytical approximations 14
2.2.1 Landau theory 14
2.3 Metastable states 17
2.3.1 Metastability from the perspective of equilibrium statistical mechanics 18
2.3.2 Metastability from the perspective of non-equilibrium dynamics. 19
2.4 The extended free energy F_3 20
2.5 Spinodal points 21

2.5.1 Spinodal points in systems with long-range interactions . . 23

3 The q-State Potts Model 27
3.1 The Potts model . . . 28
3.1.1 Our notation . . . 30
3.2 Applications . . . 32

4 Dynamical Relaxation Processes 35
4.1 Domain growth . . . 37
4.1.1 Scaling hypothesis . . . 37
4.1.2 Coarsening . . . 38
4.1.3 Activated processes and logarithmic growth . . . 40
4.1.4 Nucleation . . . 40
4.1.5 Two dynamical scenarios — or more? . . . 42
4.2 Frustration . . . 43
4.2.1 Geometric frustration . . . 43
4.2.2 Dynamical frustration . . . 44

5 Short-Time Dynamics in Critical Systems 45
5.1 Short-Time Dynamics (STD) . . . 47
5.1.1 Power-law behavior in STD . . . 48
5.2 STD as a technique for locating critical points . . . 50

II Results 53

6 Short-Time Dynamics in Mean-Field Models 55
6.1 Introduction . . . 56
6.2 Formal solution of the FPE and moment expansion . . . 57
6.3 Paradigmatic mean-field model: Curie–Weiss . . . 58
6.4 STD near the critical point . . . 59
6.4.1 Ornstein–Uhlenbeck approximation . . . 60
6.4.2 Quartic drift potential approximation . . . 62
6.4.3 Other initial conditions . . . 63
6.5 STD near the spinodal . . . 63
6.6 Chapter conclusions . . . 67

7 Metastability in the Two-Dimensional q-State Potts Model 71
7.1 Introduction . . . 72
7.2 Using STD at spinodal points . . . 74

7.2.1 STD at spinodal points of systems with long-range interactions . . . 74
7.2.2 Spinodal points in the short-range Potts model . . . 78
7.3 Metastability in the Potts model . . . 85
7.3.1 Hysteresis . . . 86
7.3.2 The Binder criterion and the two possible scenarios . . . 86
7.3.3 Response to Binder's question about metastability . . . 87
7.4 Relaxation from the metastable state: nucleation . . . 89
7.5 Chapter conclusions . . . 92

8 Relaxation in the Two-Dimensional q-State Potts Model 93
8.1 Introduction . . . 94
8.2 Relaxation in the Potts model . . . 96
8.2.1 Relaxation at intermediate temperatures and blocked states: characterization and scaling . . . 97
8.2.2 Probability of blocked states . . . 104
8.2.3 Relaxation at low temperatures: glassy state . . . 107
8.2.4 Boundary conditions . . . 110
8.3 Chapter conclusions . . . 111

III Conclusions 113

9 Conclusions 115

IV Appendices 119

A Supplementary Calculations for STD in Mean-Field Systems 121
A.1 Quartic potential approximation near the critical point . . . 122
A.2 Moment calculations near the spinodal . . . 123

B The Continuous-Time Monte Carlo Method 127
B.1 Motivation . . . 128
B.2 The n-fold way technique . . . 128
B.3 CTMC implementation for the q-state Potts model . . . 130
B.3.1 Justification of the time increment . . . 131
B.4 Validation and performance . . . 131

C GPU Implementation of the q-State Potts Model **135**
C.1 What is GPGPU? What is CUDA? 136
C.2 Device architecture and GPGPU programming overview 137
C.3 Optimized GPU-based Monte Carlo algorithm for the q-state Potts model 139
C.3.1 Random Number Generator 139
C.3.2 Spin update 140
C.3.3 Computation of energy, magnetization, and associated moments 141
C.4 Algorithm validation 141
C.5 Algorithm performance 144
C.6 Appendix summary 146

References **147**

Acknowledgements and Dedication **161**

Acknowledgements **161**

Dedication **163**

CHAPTER 1

INTRODUCTION

The study of Non-Equilibrium Statistical Mechanics remains, to this day, one of the great challenges in the broad field of Condensed Matter Physics. We generally understand the equilibrium states of different systems, their characteristics and properties, but in many cases we know surprisingly little about how these same systems respond when placed out of equilibrium — which is, in fact, the predominant situation found in nature.

In this thesis we propose a study of relaxation toward equilibrium in systems exhibiting first-order phase transitions, along with related phenomena such as metastability and spinodal points.

Our analysis is grounded in the study of the two-dimensional ferromagnetic q-state Potts model, which has served for decades as a paradigmatic model in the study of the Statistical Mechanics of Critical Phenomena and Phase Transitions. It is of particular theoretical interest because, by varying the number of accessible states q for the spin variable, the model displays temperature-driven magnetic phase transitions of both first order ($q > 4$) and second order ($q \leq 4$) at zero field. Despite being a simple ferromagnetic model (with nearest-neighbor ferromagnetic interactions), the Potts model has proven to exhibit a remarkably rich dynamical phenomenology, due in large part to the degeneracy of its ground state. Thanks to this simplicity in its equilibrium properties, the Potts model allows us to characterize purely dynamical processes arising from collective phenomena, while at the same time contrasting them with phenomena (perhaps more extensively studied in the literature) that are dominated by defects, vacancies, or competitive interactions explicitly built into the model.

The results presented in this thesis are based primarily on Monte Carlo numerical simulations, for which we implemented various algorithmic techniques, both traditional and novel. In addition, we present analytical results in those cases where such an approach was feasible — in particular, we obtain analytical results for the dynamics of the Potts model with $q = 2$ in the Mean-Field approximation (the Curie–Weiss model).

The contents of this thesis are the product of five years of work, carried out in collaboration with Dr. Sergio A. Cannas (advisor) and, to a significant extent, with colleagues at our institution and other institutions (whom we acknowledge at the appropriate points). The majority of these results have been submitted for publication in international journals.

Structure of the thesis

Part I presents the Theoretical Framework in which the results of this thesis are situated. It is organized as follows:

In **Chapter 2** we introduce the topic of Phase Transitions, reviewing their well-known general properties while attempting to view them from our own perspective. Notably, the introduction of the concept of metastable states is perhaps somewhat non-standard, and we believe that a degree of originality is present in the discussion of *spinodal points* associated with first-order phase transitions — approached here via an extended free energy, distinguishing finite-range systems from the classic double-well picture of Mean-Field theories.

Chapter 3 is dedicated to briefly presenting the q-state Potts model, introducing our notation, and highlighting the fields of application of the model.

In **Chapter 4** we provide a general overview of the known dynamical relaxation processes. We describe the characteristic features of the mechanisms that govern the relaxation of a system toward equilibrium when it is initially placed out of equilibrium, and characterize these mechanisms according to the nature of the system and the range of values of the externally imposed parameters. While this chapter also serves as a review of topics familiar in Statistical Mechanics, we approach it from our own perspective — in particular, we introduce in our own terms the concept of *dynamical frustration*, distinguishing it from geometrical frustration and from that generated by explicit disorder in the model.

In **Chapter 5**, being fundamental ingredients of the development of this thesis, we review the concepts of Short-Time Dynamics (STD), its scaling laws, and its use as a technique for identifying and characterizing critical points.

Part II presents the original results of this thesis:

In **Chapter 6** we study Short-Time Dynamics for a mean-field model with a non-conserved order parameter (Curie–Weiss model with Glauber dynamics) by solving exactly the associated Fokker–Planck equation. We obtain closed-form expressions for the first moments of the order parameter, both near the critical point and near the spinodal points, starting from different initial conditions. This allows us to confirm the validity of the Short-Time Dynamics scaling hypothesis in both cases. Although the procedure is shown for a particular mean-field model, our results extend straightforwardly to generic models with a single or-

der parameter.

In **Chapter 7** we study the metastability associated with the first-order phase transition in the q-state Potts model for $q > 4$. First-order phase transitions are generally accompanied by hysteresis and metastability, and the Potts model is no exception. The metastable phase can only be observed in a region close to the transition, bounded by what we call the spinodal. However, the concept of the spinodal is rigorously defined only in systems with infinite-range interactions (mean field). In this chapter we show that it is possible to define the spinodal point through the behavior of Short-Time Dynamics, and that this definition applies equally to mean-field systems — where the resulting spinodal agrees with the traditionally defined spinodal point — and to systems with short-range interactions. Moreover, the very existence, in the thermodynamic limit, of metastable states associated with the phase transition in the two-dimensional q-state Potts model has been a long-standing controversy. On this point, we show that the spinodal is separated from the transition point for all $q > 4$, delimiting a temperature interval capable of sustaining metastable states that remains finite even in the thermodynamic limit. We are also able to address the controversy directly by means of a criterion proposed *ad hoc* for this problem, which would not have been possible without a Monte Carlo algorithm that runs in parallel on GPU accelerators. As a result, we provide numerical evidence in favor of the existence of metastable states associated with the first-order phase transition, and analyze the relaxation mechanism from these states to equilibrium.

In **Chapter 8** we carry out a systematic study of the nonequilibrium dynamics of the q-state Potts model on the square lattice following a quench from infinite temperature to subcritical temperatures. Using a Continuous-Time Monte Carlo algorithm, we analyze the long-time behavior of the energy and relaxation time over a wide range of quench temperatures and system sizes. For $q > 4$ we identify the existence of distinct dynamical regimes depending on the temperature range. At low (but finite) temperatures and very long times, Lifshitz–Allen–Cahn-type domain growth is interrupted with finite probability and the system becomes trapped in highly symmetric metastable states that induce thermal activation in domain growth. Furthermore, at very low temperatures the system always becomes trapped at early times in highly disordered metastable states with a finite lifetime, which have been identified as glassy states. We analyze in detail the finite-size scaling properties of the various relaxation times involved and their temperature dependence.

Part III summarizes the main conclusions of this thesis and discusses the implications and possible extensions of the work presented here.

Three appendices complement this manuscript, collected in **Part IV**. Appendix A contains supplementary calculations to the development of Chapter 6. The Continuous-

Time Monte Carlo algorithm used to obtain the majority of the results in Chapter 8 is described in Appendix B. Finally, in Appendix C we present our implementation of the q-state Potts model for simulation on GPU accelerators, used in part of Chapter 7.

It is our hope that this thesis contributes to the theoretical understanding of the dynamical mechanisms associated, in general, with systems undergoing first-order phase transitions. To this end, we have endeavored to highlight those results which we believe are of broad generality in Statistical Mechanics, and which extend beyond the particular models employed here.

Part I

Theoretical Framework

CHAPTER 2

FIRST-ORDER PHASE TRANSITIONS

The matter surrounding us exists in an incredibly diverse range of natural states. From ancient times, long before the advent of science, people classified materials according to their properties — distinguishing gases, liquids, and solids, and their different behaviors. More recently, scientists have distinguished ordinary liquids from superfluids, conductors from semiconductors and insulators, gases from plasmas, and so on; they have studied an enormous variety of magnetic materials, liquid crystals, ferroelectrics, and many other states of matter.

The branch of physics concerned with the properties and phenomenological behavior of matter at this observable, macroscopic level is *Condensed Matter Physics*. This discipline builds conceptual bridges, methods, and mathematical formalisms connecting the fundamental laws governing the behavior of microscopic matter — such as atoms, ions, and electrons — to the macroscopic properties of systems (whether a substance is solid or liquid, whether it conducts electricity, and so forth).

Broadly speaking, the forces and fields that act on microscopic matter give rise to a wide variety of modes of aggregation and organization of particles. Distinct states of aggregation of matter, which differ qualitatively or functionally in their macroscopic properties, are called *thermodynamic phases*, or simply *phases*. These phases are determined by thermodynamic conditions in the surrounding environment, such as temperature, pressure, magnetic fields, electric fields, and so on.

In particular, the area of theoretical physics devoted to the study of the phases of matter and the transitions between them is *Statistical Mechanics*.

A *phase transition* is defined as an abrupt change in the internal structure and properties of a system caused by variations in its environment. Paradigmatic examples include the gas-to-liquid transition, the liquid-to-solid transition, the normal-to-superconducting transition, and the paramagnetic-to-ferromagnetic transition. Although these are, in general, very familiar phenomena, some of their fundamental physical aspects are still not fully understood, so the study of phase transitions remains of great theoretical and technological interest.

2.1 General characteristics of phase transitions

2.1.1 Classification

Historically, phase transitions were classified as *first-order transitions*, *second-order transitions*, and *higher-order transitions* according to the proposal of Ehrenfest [6]. This classification names a phase transition according to the lowest-order deriva-

tive of the thermodynamic potential (e.g., the Helmholtz free energy) that is discontinuous at the transition. If the discontinuity occurs in a first derivative of the thermodynamic potential, the transition is called first-order; if it occurs in a second derivative, second-order; and if discontinuities appear only at the n-th derivative with $n > 2$, it is called a higher-order transition.

We now know that the Ehrenfest classification is inadequate, since in most transitions that we call "second-order," one or more second derivatives of the potential — rather than exhibiting a discontinuity — concretely *diverge* at the transition. These transitions are more correctly called *continuous phase transitions*. Correspondingly, first-order phase transitions are also known as *discontinuous phase transitions*. The Ehrenfest classification has nonetheless been so widely used historically that both terminologies continue to coexist.

For illustration: the various solid/liquid/gas transitions are first-order (discontinuous), because they involve a discontinuous change in density, which is the first derivative of the free energy with respect to the chemical potential. The ferromagnetic transition in metals such as iron — where the magnetization (first derivative of the free energy with respect to the applied magnetic field) grows continuously from zero as the temperature is lowered — is a second-order (continuous) transition, with the magnetic susceptibility (second derivative of the free energy with respect to the field) diverging at the critical temperature.

2.1.2 Order parameter

To describe phase transitions in a general way, one commonly refers to an *order parameter*. Although this term was coined in Landau theory (see e.g. [7]) and is inspired by magnetic systems, we can define it broadly as a quantity that vanishes in one of the phases involved in the transition and is nonzero in the other.

In the paramagnet-to-ferromagnet transition a suitable order parameter is the net magnetization (zero in the high-temperature phase, nonzero in the low-temperature phase), while for the liquid-gas transition the order parameter is the difference in density between the liquid and the gas along the coexistence curve. In these examples the order parameters, as noted, are first derivatives of the corresponding thermodynamic potential with respect to the thermodynamic variable governing the transition, and they are scalar quantities.

Other types of phase transitions require more elaborate order parameters of various mathematical natures; for instance, structural transitions in liquid crystals are described by a tensorial order parameter [7].

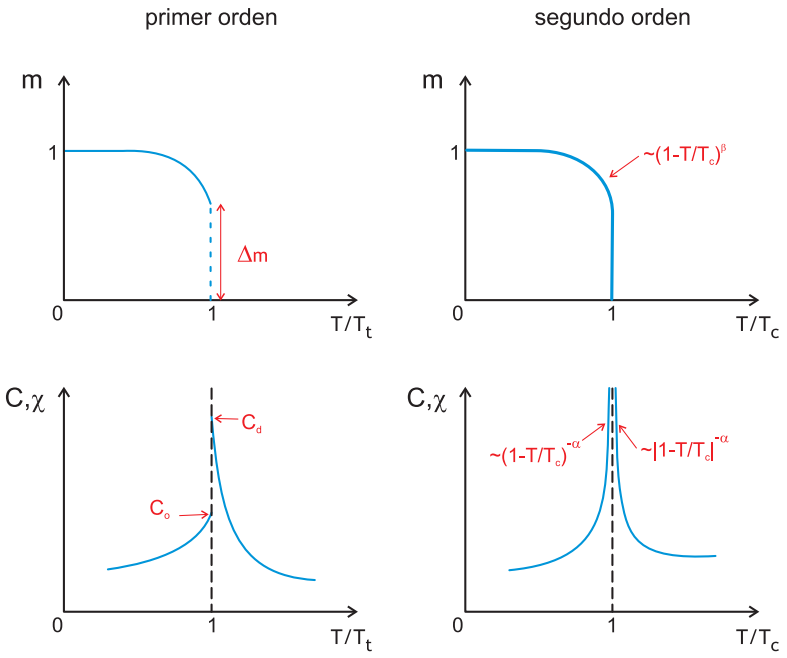


FIGURE 2.1: Schematic of the order parameter m (left) and susceptibility χ (right) as functions of temperature for a second-order transition (top row) and a first-order transition (bottom row).

2.1.3 Phenomenology

The principal characteristics of first- and second-order phase transitions are illustrated schematically in Fig. 2.1. In a second-order transition, the order parameter m changes continuously from 0 to 1 as the temperature is lowered from high values toward $T = 0$. However, its derivative with respect to the magnetic field B evaluated at $B = 0$, the susceptibility $\chi(T)$, diverges at the critical temperature $T = T_c$. In a first-order transition, by contrast, m undergoes a discontinuous jump at the transition temperature $T = T_t$, and the one-sided susceptibilities $\chi^{\pm}(T)$ remain finite. The same holds for the derivative of the entropy with respect to temperature (i.e., the specific heat C_B): it diverges at a second-order transition and remains finite on both sides of a first-order transition.

This phenomenology gives rise to the distinctive aspects of each type of transition: critical phenomena in continuous transitions, and phase coexistence and metastability in discontinuous ones.

Continuous transitions

Second-order phase transitions are characterized by the divergence of second derivatives of the thermodynamic potential. Quantities such as the magnetic susceptibility and specific heat diverge at the transition point — the *critical point* — as power laws with nontrivial exponents, the *critical exponents*. For example, in the second-order transition of Fig. 2.1:

$$\chi(T) \propto |1 - T/T_c|^{-\gamma}, \qquad C_B \propto |1 - T/T_c|^{-\alpha}, \tag{2.1}$$

where α and γ are the critical exponents associated with the specific heat and susceptibility, respectively. The critical exponents for different divergent quantities are related by scaling relations, and vastly different systems can share identical sets of critical exponents — a property called *universality*. The universality class of a system depends only on very general properties such as spatial dimensionality and the symmetry of the order parameter, and not on the microscopic details of the interactions. This remarkable universality stems from the divergence of the correlation length near the critical point, which renders the microscopic scale irrelevant.

Discontinuous transitions

First-order transitions involve a discontinuity in a first derivative of the thermodynamic potential. During the transition the temperature of the system remains constant while a fixed amount of energy is absorbed or released as heat — the latent heat. Associated with first-order transitions, one finds mixed-phase regimes in which distinct phases coexist, with neither dominating. A classic example is the coexistence of liquid water and ice at $0°$C and atmospheric pressure. Moreover, as we shall discuss in detail, first-order phase transitions admit the possibility of *metastable* phases — phases that persist in the "thermodynamic territory" of the other — in a window of the control parameter around the transition, accompanied by hysteresis. Unlike continuous transitions, first-order transitions generally do not exhibit diverging correlation lengths, and universality of thermodynamic functions near the transition cannot be expected *a priori*. Nevertheless, approaches rooted in critical phenomena — such as the Renormalization Group — have contributed significantly to the understanding of first-order transitions. It is worth emphasizing that, although second-order transitions and their associated critical phenomena have generated enormous theoretical, numerical, and experimental activity over the past 40 years, the great majority of phase transitions occurring in nature are first-order.

2.2 Analytical approximations

Bridging the laws governing microscopic behavior and macroscopic phenomena such as phase transitions requires approximations. Even when all effective atomic interactions are known, it is generally not possible to predict theoretically under what thermodynamic conditions a phase transition will occur, since the problem involves the simultaneous interaction of an enormous number ($\sim 10^{23}$) of individual components.

2.2.1 Landau theory

Motivated by the structural similarities in the asymptotic expansions near the critical point in earlier mean-field theories [8, 9] (such as the van der Waals and Curie–Weiss approaches), Lev Landau proposed that the same type of reasoning could be applied to all phase transitions. The resulting framework is known as the Landau phenomenological theory. It postulates that, once the order parameter has been identified, any phase transition can be described through a variational principle associated with a functional $\mathcal{F}(\{K_i\}, \phi)$ — the *Landau functional* — that depends on the order parameter ϕ and the system parameters $\{K_i\}$. The equilibrium state is determined by the absolute minimum of this functional with respect to ϕ.

Landau proposed that the form of $\mathcal{F}$ can be deduced phenomenologically from two premises: (i) the functional must be consistent with the symmetries of the system's Hamiltonian, and (ii) near the transition it must be an analytic function of ϕ, admitting a power-series expansion for small ϕ:

$$\mathcal{F}(\{K\}, \phi) = \sum_{n=0}^{\infty} a_n \left(\{K\}, T\right) \phi^n \tag{2.2}$$

Second-order transitions

For the Ising case, using results from mean-field theory [8], it suffices to keep terms up to order $O(4)$ in (2.2). The most general form at zero field (where the Z_2 symmetry of the Ising Hamiltonian requires all odd-order coefficients to vanish) is:

$$\mathcal{F}(\{K\}, \phi) = a_0(\{K\}, T) + a_2(\{K\}, T)\phi^2 + a_4(\{K\}, T)\phi^4 \,. \tag{2.3}$$

The coefficient a_4 is a smooth positive function of T, and can be taken as constant near T_c. Since the coefficients must be analytic near the transition, we

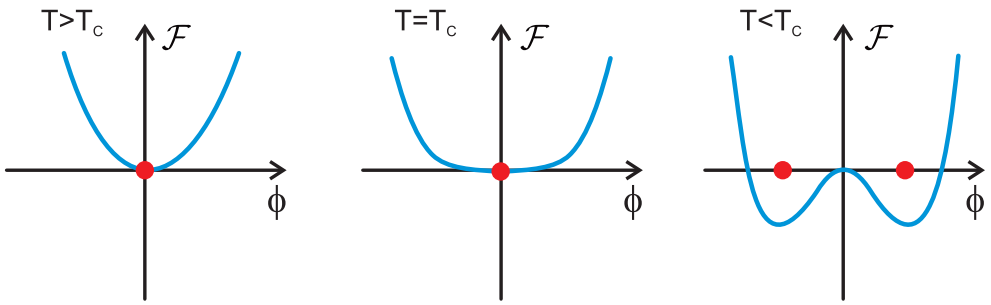


FIGURE 2.2: The Landau free energy $\mathcal{F}$ for various values of T at $h = 0$. Red dots indicate the values of ϕ at which $\mathcal{F}$ reaches its global minimum. The continuous phase transition occurs as T varies from above to below T_c.

can expand a_2 in a Taylor series around $T - T_c$:

$$a_2 = a_2^0 + a_2^1 \frac{T - T_c}{T_c} + O((T - T_c)^2)\,. \tag{2.4}$$

Minimizing $\mathcal{F}$ with respect to ϕ gives solutions $\phi = 0$ and $\phi = \pm\sqrt{-a_2(T)/2a_4}$. For $a_2(T) > 0$, $\mathcal{F}$ has a unique minimum at $\phi = 0$ (disordered phase); for $a_2(T) < 0$, two symmetric minima appear at $\pm\phi_0$ (see Fig. 2.2). Since at $T \geq T_c$ the equilibrium value of ϕ must be zero, we require $a_2^0 = 0$ and $a_2^1 > 0$.

There is therefore a continuous phase transition from a disordered state ($\phi = 0$) to an ordered state ($|\phi| > 0$) as T crosses T_c. Including an external field $h \neq 0$, the Landau functional for second-order transitions near the critical region takes the standard form:

$$\mathcal{F} = \frac{1}{2} a\tau\phi^2 + b\phi^4 - h\phi \tag{2.5}$$

where $\tau \equiv (T - T_c)/T_c$ is the reduced temperature and $a, b > 0$ are phenomenological coefficients. From this one recovers the usual mean-field asymptotic behavior and critical exponents.

First-order transitions

The cubic term in the Taylor expansion (2.2) was discarded above on the basis of Ising-type symmetry. If this symmetry is absent, odd powers of ϕ must be included. In particular, a cubic term can give rise to a first-order transition[1].

[1]This is the case for the Potts model with $q \geq 3$, which in the mean-field approximation corresponds to a first-order transition.

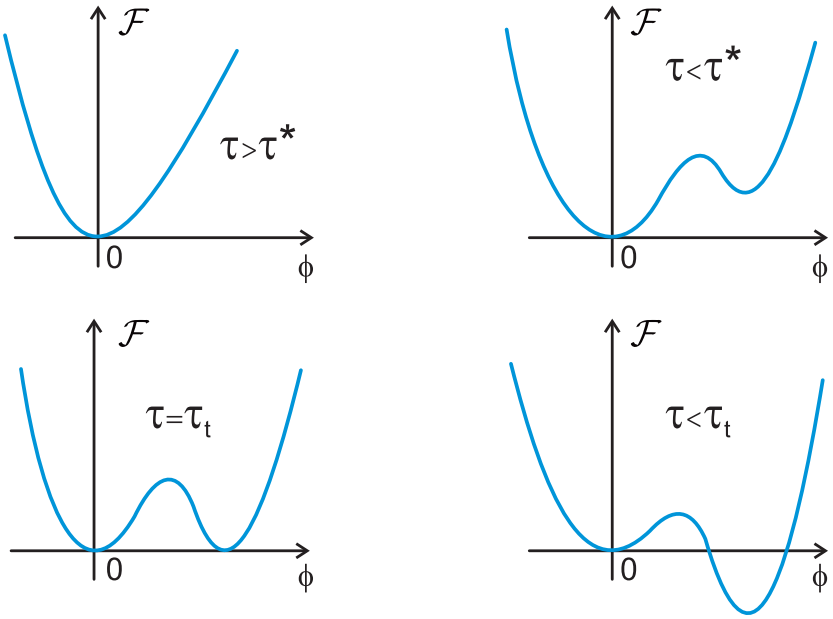


FIGURE 2.3: The Landau free energy $\mathcal{F}$ as a function of ϕ for various temperatures, illustrating a first-order phase transition.

Consider generically a Landau expansion of the form:

$$\mathcal{F}(\phi) = \frac{1}{2}a\tau\phi^2 - \frac{1}{3}c\phi^3 + \frac{1}{4}b\phi^4 + \dots \tag{2.6}$$

where $a, b, c > 0$ and $\tau = (T - T_c')/T_c'$ (T_c' being the temperature at which the second-order transition would occur in the absence of the cubic term). The extremality condition gives:

$$\frac{\partial \mathcal{F}}{\partial \phi} = \phi\left(a\tau - c\phi + b\phi^2\right) = 0 \tag{2.7}$$

with solutions $\phi = 0$ or $\phi_\pm = \frac{c}{2b} \pm \sqrt{\left(\frac{c}{2b}\right)^2 - \frac{a\tau}{b}}$.

A second real positive solution exists when $\tau < \tau^* = c^2/(4ab)$.

Since $\tau^* > 0$, this occurs at a temperature $T > T_c'$, i.e., before the second-order transition would occur. The evolution of $\mathcal{F}$ as T varies is shown schematically in Fig. 2.3. For $\tau > \tau^*$ there is a unique minimum at $\phi = 0$ (disordered phase). When $\tau = \tau^*$ a second (local) minimum appears at $\phi_+(\tau) > 0$, which becomes more pronounced as the temperature decreases. At $\tau = \tau_t$ this minimum reaches the same free energy as the $\phi = 0$ solution, and a discontinuous transition occurs

from a disordered phase ($\phi = 0$) to an ordered phase ($\phi > 0$), since for $\tau < \tau_t$ the global minimum lies at $\phi_+(\tau)$.

The local minima in Fig. 2.3 represent metastable states associated with the first-order phase transition in Landau theory. Although from the thermodynamic point of view these local minima do not contribute to the partition function and disappear when we construct the thermodynamic potential from the minimum of the Landau functional (see Eq. (2.14)), they are relevant from a dynamical point of view: in the absence of order-parameter fluctuations (as in the Landau and all mean-field approximations), a system prepared in a state with $\phi_+(\tau) > 0$, for $\tau_t < \tau < \tau^*$, will remain in that local minimum without undergoing any transition.

We now discuss metastable states and their limits of existence — the spinodal points — in greater depth.

2.3 Metastable states near a first-order phase transition

First-order phase transitions are accompanied by hysteresis and metastability. Consider a system undergoing a first-order transition driven by a control variable φ (which could be the magnetic field H for the field-driven Ising transition at $T < T_c$, or the temperature T for the temperature-driven Potts transition with $q > 4$). Although the thermodynamic transition occurs at $\varphi = \varphi_t$, when φ is varied slowly from an "initial" value $\varphi_i > \varphi_t$ to a "final" value $\varphi_f < \varphi_t$, the system may remain in the phase corresponding to thermodynamic equilibrium at $\varphi > \varphi_t$ (and vice versa when φ is varied in the opposite direction). A phase that survives having been taken outside its thermodynamic "territory" is said to be *metastable*.

Metastable phases have a finite lifetime, but this lifetime can be very long. Well-known examples are diamond at ambient temperature and pressure, and supercooled glass-forming liquids (which can be so long-lived that they are practically indistinguishable from equilibrium phases for almost all purposes). In general, however, a metastable phase cannot persist for all φ and is not observed below some value $\varphi_{\rm sp}$ — the *spinodal point*.

There are essentially two main ways of approaching the study of metastable states, which we now describe.

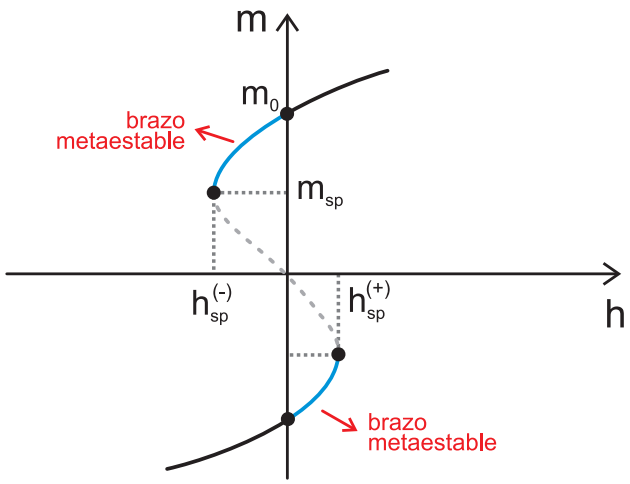


FIGURE 2.4: Schematic of the metastable branches of the equation of state $m(h)$ around a first-order transition driven by the magnetic field h at a temperature below the critical temperature of the second-order transition. $h_{sp}^{\pm}$ are the corresponding limits of metastability.

2.3.1 Metastability from the perspective of equilibrium statistical mechanics

In mean-field theories, metastable states and the spinodal points at which they cease to exist are well defined. The best-known example is the famous van der Waals loop for the gas–liquid transition (see e.g. [8]). As we saw, in the framework of Landau theory these states appear as stable solutions of the order parameter, corresponding to a local minimum of the Landau functional.

In Fig. 2.4 we see the magnetic analogue of the van der Waals loop. Here m is the order parameter (magnetization) and the control parameter is the magnetic field h, at fixed $T < T_c$. The thermodynamic transition occurs at $h = 0$, but it is possible to obtain a metastable state with $m > 0$ ($m < 0$) for $h \lesssim 0$ ($h \gtrsim 0$).

Unfortunately, while the description of metastability seems so straightforward in mean-field theories, this is not the case within more rigorous frameworks. Statistical mechanics is built to yield equilibrium states.

Consider the partition function for a system of volume V and N components at temperature T:

$$Z(N, V, T) = \exp(-\beta F) = \sum_i \exp(-\beta E_i) \tag{2.8}$$

where F is the Helmholtz free energy and the sum is over all possible configurations of the system. In the thermodynamic limit, metastable states contribute neg-

ligibly to this sum [10]. To study them within this framework one must restrict the sum to "reasonably uniform" configurations — for example, by excluding configurations containing droplets of the competing phase larger than a critical nucleus. Several approaches have been suggested in this direction [11].

2.3.2 Metastability from the perspective of non-equilibrium dynamics.

A fundamentally different approach to metastability arises from the observation that what one measures experimentally are time averages, which coincide with ensemble averages only in equilibrium. A metastable state is a non-equilibrium situation, yet it is observable; it is therefore natural to *define* it through non-equilibrium, dynamical properties — specifically, through the relaxation dynamics of the system [12]. This is the approach we adopt throughout this thesis.

To fix ideas, consider the Ising model and associate a stochastic dynamics with it. We assume a Markovian Master Equation for the probability $P(s_1, \ldots, s_N, t)$ of a spin configuration $\{s_1, \ldots, s_N\}$ occurring at time t [13,14]:

$$\begin{aligned} \frac{d}{dt}P(s_1,\ldots,s_N,t) &= -\sum_{i=1}^{N} w(s_i \to -s_i)P(s_1,\ldots,s_i,\ldots,s_N,t) + \\ &+ \sum_{i=1}^{N} w(-s_i \to s_i)P(s_1,\ldots,-s_i,\ldots,s_N,t) \end{aligned} \tag{2.9}$$

with transition probability $w(s_i \to -s_i)$ (Glauber dynamics):

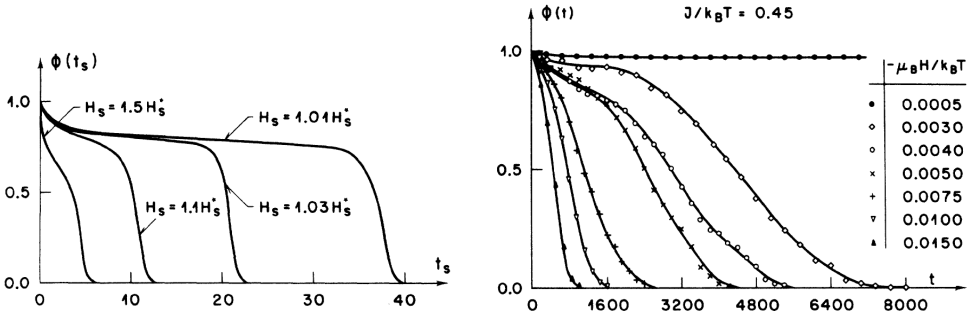
$$w(s_i \to -s_i) = (2\tau_s)^{-1}\left[1 - \tanh(\delta E/2k_BT)\right] \tag{2.10}$$

where τ_s sets the time unit and δE is the energy change produced by flipping the spin.

We consider relaxation after a sudden change in field h, starting from an ordered state of *up* spins, from $h_i > 0$ to $h_f = h_i + \Delta h < 0$. We define a "non-equilibrium relaxation function":

$$\phi_m(t) = \frac{\langle m(t)\rangle - \langle m(\infty)\rangle}{\langle m(0)\rangle - \langle m(\infty)\rangle} \tag{2.11}$$

In $\phi_m(t)$, metastability manifests itself through a two-stage relaxation: after a short time of order t_{eq} (the equilibrium relaxation time), the system settles near m_{ms} (the metastable order parameter value); then on a much longer timescale



(A) (B)

FIGURE 2.5: (A) Non-equilibrium relaxation function $\phi(t_s)$ plotted versus the rescaled time t_s, obtained from a time-dependent Ginzburg–Landau equation, for several values of the rescaled magnetic field $H_s \equiv h/k_BT$. (B) Non-equilibrium relaxation function $\phi(t)$ vs. time (in Monte Carlo steps) at $J/k_BT = 0.45$, after a sudden change from $H_i = 0$ to $H_f = H$, for several values of $\mu_B H/k_BT$. Both figures taken from [15].

t_{ms} — the metastable lifetime — it decays to equilibrium. This two-stage behavior produces a well-defined plateau in $\phi_m(t)$, as illustrated in Fig. 2.5. The condition for metastability is simply that these two timescales be clearly separated: Binder [12] places this at $t_{ms} \geq 10^2\, t_{eq}$; in general the condition is $t_{ms} \gg t_{eq}$.

This dynamical definition of metastability allows us to speak of metastable states whenever the system rests for a measurable time in a quasi-stationary state with its own distinct properties — even far from the transition, as we shall see in Chapter 8.

2.4 The extended free energy F_3

As a basis for the subsequent discussion of spinodal points, we introduce in this section the three-parameter extended free energy F_3. For simplicity we focus on the magnetic case.

For a magnetic system we have the free energy $F(T,h) \equiv -k_BT \ln Z$, from which the equation of state $M = -(\partial F/\partial h)_T$ follows.

The formal equilibrium approach *excludes* metastable states. However, to define the spinodal point precisely as the point at which metastable states become unstable, we need to include them in our scheme. To this end we consider an

extended or generalized three-variable free energy $F_3(T, h, M)$, defined by:

$$e^{-\beta F_3(T,h,M)} = \sum_{\{s_i\}} \delta\left(\left(\sum_i s_i\right),\ M\right) e^{-\beta\left(H_0 - h\sum_i s_i\right)} \tag{2.12}$$

where $\delta(\cdot,\cdot)$ is the Kronecker delta and $H = H_0 - h\sum_i s_i$ is the system Hamiltonian. The probability P that the system is in a state with magnetization per spin $m = M/N$ is:

$$P(T, h, m) = \frac{e^{-\beta N f_3(T,h,m)}}{Z} \tag{2.13}$$

where $f_3(T, h, m) = F_3(T, h, M)/N$ is the extended free energy per spin.

One can show that the sum defining Z is dominated in the thermodynamic limit by the M that minimizes F_3, so in equilibrium:

$$F(h, T) = \min_M F_3(T, h, M). \tag{2.14}$$

The extended free energy F_3 is applicable in both equilibrium and *non-equilibrium* situations. According to Eq. (2.13), the most probable value of m is the one that minimizes f_3, so this extended free energy acts as an effective potential governing the dynamics of the order parameter. Its local minima correspond to metastable states.

For infinite-range (mean-field) systems, f_3 is an analytic function of m with the double-well structure of the Landau functional, and it can be shown that f_3 acts as an exact potential for Glauber or Metropolis dynamics [16]. In this case, a finite barrier in f_3 implies an infinite barrier in $F_3 = N f_3$ as $N \to \infty$, so metastable states have infinite lifetime in the thermodynamic limit. For finite-range interactions the situation is far more subtle, and the possibility of describing metastable states through f_3 is not immediately clear — a point we return to in the following section.

2.5 Spinodal points

At the mean-field level, spinodal points are well defined.

In mean-field, and in the limit $N \to \infty$, f_3 has two minima as a function of m for T below some critical temperature T_c and h within a certain range $-h_{\text{sp}} < h < h_{\text{sp}}$ [9, 11]. As a function of h, the first-order transition occurs at $h = h_t = 0$. When $h = 0$, the two minima are symmetric. When $h \neq 0$, the absolute minimum corresponds to the thermodynamic equilibrium (stable) phase, while the secondary local minimum defines the metastable phase (higher free energy but dynamically stable).

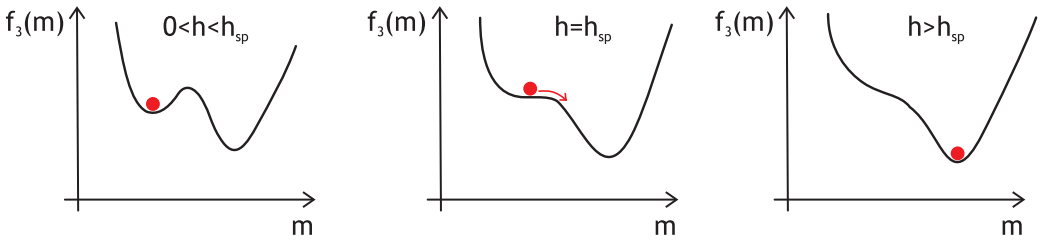


FIGURE 2.6: Schematic of the double-well potential of f_3 near a field-driven first-order transition. When $h < h_{sp}$ a system in the local minimum (here corresponding to negative magnetization) is metastable with infinite lifetime; at $h = h_{sp}$ the minimum becomes an inflection point and the metastable state ceases to exist.

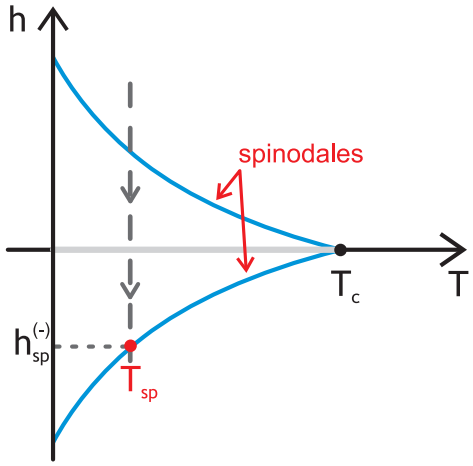


FIGURE 2.7: Schematic of the spinodal lines surrounding a 1st order transition. At $T < T_c$ one can vary h from $h > h_t = 0$ to $h < 0$ while keeping the system in the positive-magnetization state, but not beyond $h_{sp}^{(-)}$, where that state becomes unstable.

When it exists, the metastable phase (in mean field) has infinite lifetime. At $h = h_{\rm sp}$ the secondary minimum disappears (becomes an inflection point) and the metastable phase becomes unstable (see Fig. 2.6): a system prepared with a magnetization different from that of the thermodynamic equilibrium state evolves toward equilibrium. For $|h| \geq h_{\rm sp}$, f_3 has only one minimum. Thus, in mean field, the spinodal point (where the metastable state becomes unstable, in the sense that the second derivative of f_3 with respect to m vanishes, see Fig. 2.7) is also the limit of metastability, i.e., the point beyond which the metastable phase can no longer be observed.

For systems with finite-range interactions the situation is far more complex [11, 17]. On one hand, the metastable phase ceases to be observable *before* it becomes unstable [18–20], because as the system moves away from the transition, the metastable lifetime decreases while its relaxation time increases; when they become of the same order, the phase is unobservable. This is the metastability limit, which differs from the spinodal. This limit is also known as the *kinetic spinodal* [21], while the term *thermodynamic spinodal* is sometimes used to denote the spinodal as defined above (the appearance of an instability).

On the other hand, the order parameter can fluctuate in space. Although f_3 can still be defined (and used to compute true equilibrium properties), in the thermodynamic limit it has no change of convexity and has a unique minimum; it therefore cannot be used to define a spinodal point.

The spinodal is thus beyond the metastability limit, and therefore outside the domain of thermodynamics and quasi-equilibrium treatments. Because of these difficulties it has been concluded that the spinodal is meaningful only in mean field [22] or in finite systems [17].

However, it is possible to detect signs of an instability in (meta)equilibrium measurements: the susceptibility and the relaxation time of the metastable phase grow as one moves deeper into the metastable region, and when extrapolated with a power law appear to diverge at a point beyond the metastability limit called the *pseudospinodal* [22, 23].

In [3] and as we discuss in Chapter 7, far from abandoning the idea of a spinodal in finite-range systems, we propose to *define* it through out-of-equilibrium properties of the system.

2.5.1 Spinodal points in systems with long-range interactions

In this section we consider models where each spin interacts with all others. For such systems, mean-field theory is exact. We briefly review the analytical results on spinodal points in mean field.

The Curie–Weiss model

We first consider the Curie–Weiss model, or fully-connected version of the Ising model. In the presence of a homogeneous external magnetic field, the Hamiltonian is:

$$\begin{aligned}\mathcal{H}_{CW} &= -\frac{J}{2N}\sum_{i\neq j} s_i s_j - h\sum_{i=1}^{N} s_i \\ &= -\frac{J}{2N}\left(\sum_{i}^{N} s_i\right)^2 - h\sum_{i=1}^{N} s_i + \text{const},\end{aligned} \tag{2.15}$$

where N is the number of spins ($s_i = \pm 1$), h is the external magnetic field, and $J > 0$.

The extended free energy per spin (2.12) can be computed exactly, since $\mathcal{H}_{CW}$ is an explicit function of the total magnetization $M = \sum_i s_i$ and the partition function can be evaluated at fixed M. In the limit $N \to \infty$:

$$\begin{aligned}f_3(T,m,h) =& \frac{1}{\beta}\left[\frac{1+m}{2}\ln\frac{1+m}{2} + \frac{1-m}{2}\ln\frac{1-m}{2}\right] \\ &- \frac{J}{2}m^2 - hm,\end{aligned} \tag{2.16}$$

where $\beta = 1/T$ (with $k_B = 1$) and $m = M/N$.

The absolute minimum of f_3 with respect to m defines the stable (equilibrium) solution $m(T,h)$. The model has a second-order transition at $h = h_c = 0$ and critical temperature $T_c = J$. For $T < T_c$, there is a line of first-order transitions at $h = 0$ where $m(T,h)$ is singular. However, there exist analytic continuations $m_+(T,h)$ of positive-h values to negative h, and $m_-(T,h)$ vice versa, as long as $|h|$ is not too large. These analytic continuations are the metastable states, corresponding to local minima of f_3.

The conditions

$$\frac{\partial f_3(T,m,h)}{\partial m} = 0, \qquad \frac{\partial^2 f_3(T,m,h)}{\partial m^2} > 0, \tag{2.17}$$

define the (meta)stable states. The secondary minimum (and hence the metastable solution) ceases to exist when $h < h_{\text{sp}}^{(-)} = -h_{\text{sp}}$, where the spinodal field h_{sp} is given by:

$$\left.\frac{\partial^2 f_3(T,m,h)}{\partial m^2}\right|_{h=h_{\text{sp}}^{(-)}} = 0. \tag{2.18}$$

Since $\partial^2 f_3/\partial m^2 = \chi_T^{-1}$, the susceptibility diverges at $h_{\rm sp}^{(-)}$, and one can show directly that for $h - h_{\rm sp}^{(-)} \ll 1$:

$$\chi_T \sim (h - h_{\rm sp}^{(-)})^{-1/2}. \tag{2.19}$$

This singularity can be treated analogously to an ordinary critical point. For fixed T:

$$C_h \sim (h - h_{\rm sp}^{(-)})^{-1/2} \tag{2.20}$$

$$\Delta m \sim (h - h_{\rm sp}^{(-)})^{1/2} \tag{2.21}$$

where C_h is the specific heat and $\Delta m = m - m_{\rm sp}^{(-)}$, with $m_{\rm sp}^{(-)} = m(h_{\rm sp}^{(-)})$ (note that $\Delta m > 0$).

Fixing h and expanding for $0 < T_{\rm sp} - T \ll 1$:

$$\Delta m \sim (T_{\rm sp} - T)^{1/2} \tag{2.22}$$

$$C_h \sim (T_{\rm sp} - T)^{-1/2} \tag{2.23}$$

$$\chi_T \sim (T_{\rm sp} - T)^{-1/2} \tag{2.24}$$

Taking Δm as an order parameter, the singular behavior near the spinodal point can be characterized exactly as at a genuine critical point. The set of critical exponents is:

$$\beta = 1/2, \qquad \alpha = 1/2, \qquad \gamma = 1/2, \qquad \delta = 2, \tag{2.25}$$

satisfying the Rushbrooke and Widom scaling relations:

$$\alpha + 2\beta + \gamma = 2, \tag{2.26}$$

$$\gamma = \beta(\delta - 1). \tag{2.27}$$

Assuming $\eta = 0$ as in mean-field critical points, and using Fisher's scaling relation $\gamma = \nu(2 - \eta)$, we get $\nu = 1/4$. From the Josephson hyperscaling relation $\nu d = 2 - \alpha$, we deduce an upper critical dimension $d_c = 6$, confirmed by a renormalization group analysis [24].

The Curie–Weiss–Potts model

The Curie–Weiss–Potts model is defined by the Hamiltonian:

$$\mathcal{H}_{\rm CWP} = -\frac{J}{N} \sum_{i \neq j} \delta(\sigma_i, \sigma_j), \tag{2.28}$$

where $J > 0$, $\sigma_i = 1, 2, \ldots, q$, and $\delta(\sigma_i, \sigma_j)$ is the Kronecker delta. The extended free energy per spin f_3 for this model can also be computed exactly [25] (at zero field):

$$f_3(m,T) = -\frac{J(q-1)}{2\,q}m^2 + \frac{1}{\beta\,q}\left\{[1+(q-1)\,m]\ln\left[\frac{1+(q-1)\,m}{q}\right] + (q-1)(1-m)\ln\left[\frac{1-m}{q}\right]\right\}. \tag{2.29}$$

The order parameter m is defined as in Eq. (3.14).

The extended free energy (2.29) has two local minima (and hence a first-order transition) for $q \geq 3$, where the transition occurs at $T_t = J(q-2)\ln(q-1)/[2(q-1)]$ [26].

For $T_{\rm sp}^{(-)} < T < T_t$ (with $T_{\rm sp}^{(-)} = J/q$) there exists a metastable disordered solution with $m = 0$ (supercooled paramagnet), and for $T_t < T < T_{\rm sp}^{(+)}$ a metastable ordered solution with $m = m_{\rm sp} \neq 0$, where the spinodal temperatures are obtained from Eq. (2.18) with $h = 0$. An analysis analogous to the above shows that near the upper spinodal $T_{\rm sp}^{(+)}$, the order parameter Δm, the specific heat, and the susceptibility display the same critical behavior (2.22)–(2.24) with the same critical exponents (2.25).

The same set of exponents is obtained in other mean-field approximations: the Landau ϕ^4 model and — for the upper spinodal — the Landau ϕ^6 model. Renormalization group techniques [24, 27] confirm these exponent values.

Near the lower spinodal temperature $T_{\rm sp}^{(-)}$, the behavior is different: the susceptibility shows a power-law divergence with exponent $\gamma = 1$, while the magnetization and specific heat remain finite. In principle, one should not expect the same critical exponents at both spinodals.

CHAPTER 3

THE q-STATE POTTS MODEL

The q-state Potts model [25, 28] is, after the Ising model, perhaps the most fruitful magnetic model in the Statistical Mechanics of phase transitions. It arises as a generalization of the Ising model [29] to more than two possible values for the spin variable, allowing each spin to adopt q different states $s = 1, 2, \ldots, q$. Historically, the first study of a version of the model (with four components) was carried out by the mathematicians Julius Ashkin and Edward Teller [30] in 1943. The general q-component model, however, bears its current name from 1952, when Renfrey B. Potts proposed it in his doctoral thesis as a response to a slightly different problem suggested by his advisor Cyril Domb. The problem was treated independently two years later by Kihara et al. [31].

The model attracted little attention in its early years, but in the mid-1970s, following the seminal work of Rodney J. Baxter [32, 33] on rigorous results for the model, it gained the interest of many researchers in statistical physics. It was subsequently adopted and modified in other areas of physics and even in other disciplines entirely.

Today the Potts model remains of great theoretical interest, in particular due to the possibility of tuning the nature of the phase transition by varying q, and due to its simplicity and suitability for the study of non-equilibrium phenomena — including domain growth kinetics, nucleation from metastable states, and slow dynamics. It is also employed in practical modeling applications such as soap foams and bubbles, genetic segregation, cellular behavior and tumor cell migration, image analysis, neural networks, and even social and demographic behavior. Its known exact results and extensive literature make it an ideal testing ground for new numerical methods and approximations in the theory of phase transitions.

3.1 The Potts model

We present a brief history of the Potts model following [25] and then formulate it in the notation we will use throughout the rest of the thesis.

The original problem proposed by Domb started from viewing the Ising model as a system of interacting spins that could be parallel or antiparallel. A natural generalization is therefore to consider a system of planar spins, each pointing along one of q equally spaced directions given by the angles:

$$\Theta_n = \frac{2\pi n}{q} \ , \ n = 0, 1, \ldots, q-1 \tag{3.1}$$

In its most general form, the interaction between nearest neighbors depends only on the relative angle between the two vectors. This is generally known as a $Z(q)$-symmetry system with Hamiltonian:

$$H = -\sum_{<ij>} J(\Theta_{ij}) \tag{3.2}$$

where the function $J(\Theta)$ is 2π-periodic and $\Theta_{ij} = \Theta_{n_i} - \Theta_{n_j}$ is the angle between two spins at neighboring sites i and j.

Domb's original proposal was:

$$J(\Theta) = -\epsilon_1 \cos(\Theta) \tag{3.3}$$

Using a Kramers–Wannier analysis [34], Potts determined the critical point of this model on the square lattice for $q = 2, 3, 4$. Unable to extend this result to $q > 4$, Potts reported as a concluding remark in his publication the critical point for all q of the following model:

$$J(\Theta_{ij}) = \epsilon_2 \, \delta(n_i, n_j) \tag{3.4}$$

where

$$\delta(n_i, n_j) = \begin{cases} 1 & \text{if } n_i = n_j \\ 0 & \text{otherwise} \end{cases}$$

is the Kronecker delta. This version of the model is the one that has attracted by far the greatest attention and is known as the *standard Potts model*, or simply the *Potts model*. For historical reasons it is sometimes found under the name *Ashkin–Teller–Potts model*. Version (3.3) is called the *planar Potts model* or the *Clock model*.

The Potts model is ferromagnetic if $\epsilon_2 > 0$ and antiferromagnetic if $\epsilon_2 < 0$. In addition to two-site interactions, there can in general be multi-site interactions, distance-dependent interactions, or interactions with external fields. For example, the Potts model on an (in principle arbitrary) lattice $\mathbf{G}$ of N sites with pair, triple, and external-field interactions takes the form:

$$-\beta H = L \sum_i \delta(\sigma_i, 0) + K \sum_{(i,j)} \delta(\sigma_i, \sigma_j) + K_3 \sum_{(i,j,k)} \delta(\sigma_i, \sigma_j, \sigma_k) + \cdots \tag{3.5}$$

where $\beta = \frac{1}{kT}$ and $\sigma_i = 0, 1, \ldots, q-1$ specifies the state of the spin at site i, $K = \beta\epsilon_2$ and K_n with $n \geq 3$ measure the strength of n-site interactions, and L is an external field applied to spin state 0.

Its partition function is:

$$Z_{\mathbf{G}}(q; L, K, K_n) = \sum_{\sigma_1=0}^{q-1} \dots \sum_{\sigma_N=0}^{q-1} e^{-\beta H}. \tag{3.6}$$

From it one can derive, for example:

The free energy per site

$$f(q; L, K, K_n) = \lim_{N\to\infty} \frac{1}{N} \log Z_G(q; L, K, K_n) \tag{3.7}$$

The internal energy per site

$$E(q; L, K, K_n) = -\frac{\partial}{\partial\beta} f(q; L, K, K_n) \tag{3.8}$$

The magnetization per site

$$M(q; L, K, K_n) = -\frac{\partial}{\partial L} f(q; L, K, K_n) \tag{3.9}$$

As is usual in Statistical Mechanics, however, we do not know how to compute the partition function exactly for this model. Exact computation of physical quantities is possible only in a few very particular cases; in general the system is analyzed using analytical approximations of various kinds or numerical simulations.

The Potts model should not be confused with the *chiral Potts model*, for whose order parameter an exact solution is known [35]. In the mathematical area of Graph Theory, much effort goes into finding exact results for the partition function of the Potts model by interpreting it as an evaluation of the Tutte polynomial [36].

3.1.1 Our notation

In this thesis we analyze the simple case where $\mathbf{G}$ is a two-dimensional square lattice of N sites (numbered $1, \dots, N$), with each site i associated to a quantity s_i (we say there is a spin at site i with spin variable s_i) that can take q different values, $s_i = 1, 2, \dots, q$. Interactions are restricted to adjacent spins, s_i, s_j, which interact with energy $-J_P\delta(s_i, s_j)$ (the constant J_P replaces ϵ_2 in (3.4)). We also include, when relevant, an external field h favoring orientation $s = 1$ arbitrarily. The Hamiltonian is then:

$$\mathcal{H}_P = -J_P \sum_{<i,j>} \delta(s_i, s_j) - h\sum_{i=1}^{N} \delta(s_i, 1), \qquad s_i = 1, 2, \dots, q \tag{3.10}$$

where the first sum runs over all nearest-neighbor pairs in the lattice. Unlike equation (3.5), we have chosen each s_i to take values $1, \ldots, q$, but any q distinct numbers would serve equally well.

In particular, for $q = 2$ we can allow each s_i to take the values $+1$ or -1, so that $\delta(s, s') = \frac{1}{2}(1 + ss')$; substituting this into (3.10) we obtain, up to an additive constant:

$$\mathcal{H}_I = -J_I \sum_{<ij>} s_i s_j - h' \sum_{i=1}^{N} s_i, \qquad s_i = -1, 1 \tag{3.11}$$

which is nothing other than the Ising Hamiltonian, with $J_I = J_P/2$ and where a factor of 2 has been absorbed into the external field variable h'. Thus for $q = 2$ we recover the Ising model as expected, keeping in mind that quantities such as the critical temperature computed from the Potts Hamiltonian will differ by a factor of 2 from the well-known values for the Ising model.

In two dimensions, the ferromagnetic version ($J_P > 0$) of model (3.10) at zero field $h = 0$,

$$\mathcal{H}_P = -J_P \sum_{<i,j>} \delta(s_i, s_j), \tag{3.12}$$

exhibits a **first-order** phase transition at a finite temperature when $q > 4$, while for $q \leq 4$ the transition is **continuous** [25]. This is the version used throughout almost the entire thesis.

We define the internal energy per spin as

$$e = \langle H \rangle / N \tag{3.13}$$

where $\langle \cdot \rangle$ denotes the average over configurations, and the order parameter [37] as

$$m = \frac{(qN_{max}/N - 1)}{q - 1} \tag{3.14}$$

where $N_{max} = \max(N_1, N_2, \ldots, N_q)$ and N_i is the number of spins in state i. Thus $m = 1$ for a fully ordered system ($N_{max} = N$, all spins aligned), and $m = 0$ for a fully disordered system (all q spin states equally populated).

Several equilibrium properties of the two-dimensional model are known exactly, though restricted to the transition point. For example, the transition temperature on the square lattice in the thermodynamic limit for all $q \geq 2$ is given by [32]:

$$\frac{k_B T_c}{J_P} = \frac{1}{\ln(1 + \sqrt{q})} \tag{3.15}$$

where k_B is Boltzmann's constant. Henceforth, for simplicity, we work in units where $k_B = J_P = 1$.

The latent heat for $q > 4$ is known exactly [32]:

$$e_d - e_o = 2\left(1 + \frac{1}{\sqrt{2}}\right) \tanh\frac{\Theta}{2} \prod_{n=1}^{\infty} (\tanh\, n\Theta)^2 \tag{3.16}$$

where $\Theta = \arccos(\sqrt{q}/2)$ and

$$e_d = \lim_{N\to\infty} \frac{1}{N} \lim_{T\to T_c^+} \langle H \rangle, \tag{3.17}$$

$$e_o = \lim_{N\to\infty} \frac{1}{N} \lim_{T\to T_c^-} \langle H \rangle. \tag{3.18}$$

Additionally [31]:

$$e_d + e_o = -2(1 + 1/\sqrt{q}) \tag{3.19}$$

from which the individual values of e_d and e_o can be extracted.

The jump in the order parameter at the transition (for $q > 4$) is given by [38]:

$$\Delta m = 1 - q^{-1} - 3q^{-2} - 9q^{-3} - 27q^{-4} - \ldots \tag{3.20}$$

Since the order parameter in the disordered phase equals zero even at the transition ($m_d = 0$), this expression gives the exact value of the order parameter in the ordered phase at T_t.

A review of the known properties of the Potts model in other dimensions, as well as results for the model under mean-field approximations, high-temperature series, and renormalization group can be found in [25, 39].

3.2 Applications

For many years interest in the Potts model rested primarily on its theoretical properties. With time, however, it has become ubiquitous across Statistical Physics as a model capable of underpinning the study of specialized and practically relevant problems.

On the experimental side, various realizations of Potts universality have been identified in adsorbed monolayers on crystalline surfaces [40–42], in cubic ferromagnets in diagonal magnetic fields [43, 44], in certain structural transitions [45], in martensitic transitions [46], and elsewhere. When seeking the experimental

correlate of a spin model, the universality class (set of critical exponents) is typically used to associate the theoretical model with the experimental system.

On the purely theoretical side, the Potts model has become a model of choice due to its simplicity and the versatility afforded by varying q to tune the nature of the phase transition. It is widely used in the study of domain growth dynamics [4, 47–50] and of nucleation as an equilibration mechanism [51–53].

The Potts model has also attracted interest from the QCD community [54–62], since an effective model for the Polyakov loop shares the $Z(3)$ symmetry of $SU(3)$ gauge theory (the 3d, $q = 3$ Potts model), and its weak first-order transition plays an important role in studies of the deconfinement transition of heavy quarks.

Beyond physics, the model has been adapted for practical applications involving soap foams and bubbles [63, 64], genetic segregation [65], cellular behavior and tumor cell migration [66, 67], image analysis [68], neural networks [69], and social and demographic behavior [70, 71].

Its exactly known critical properties make it an effective benchmark for new algorithms and approximate analytical methods.

CHAPTER 4

DYNAMICAL RELAXATION PROCESSES

Most undergraduate and graduate courses in Statistical Mechanics and Thermodynamics focus on the theoretical study of macroscopic systems in thermodynamic equilibrium. Yet in many experimental realizations — perhaps the most interesting ones — the situation is very different: systems are in contact with an equilibrated environment but, for one reason or another, cannot equilibrate with it. They therefore evolve in time while remaining out of equilibrium [72].

The list of systems evolving out of equilibrium is very long, as are the reasons why equilibration may not be achieved. The most common cases are those in which the time required to equilibrate the system exceeds the available experimental observation window — as in systems undergoing domain growth, phase separation, and classical or quantum glass formation. Another important cause is the action of external forces that drive the system away from equilibrium, as in the rheological properties of glass-forming liquids and the forced dynamics of granular materials.

Although a complete and consistent theory for non-equilibrium states, analogous to the Statistical Mechanics of ensembles for equilibrium states, does not yet exist, nearly five decades of research in this area provide a broadly optimistic picture, and several non-equilibrium mechanisms have been well catalogued and understood.

We focus here on what has come to be called the Theory of Phase-Ordering Kinetics [73]: the systematic study of the mechanisms by which a system brought suddenly from one equilibrium condition (typically a homogeneous, disordered high-temperature phase) to another (typically a symmetry-broken, low-temperature phase) "orders" itself through the growth and coarsening of domains.

To fix ideas, consider a system with an order–disorder or ferromagnet–paramagnet phase transition, which having been equilibrated in a disordered (homogeneous) high-temperature state is suddenly cooled[1] to a temperature below the transition temperature T_c (see Fig. 4.1). Since at this temperature there exist (at least[2]) two different equilibrium states, the question is which one the system selects and how it does so. The way the system adapts to its new environmental conditions depends on the nature of the system and its associated dynamics, on the interactions between its components, and fundamentally on the environmental conditions (i.e., the magnitudes of external parameters such as temperature and magnetic field). A diverse range of dynamical mechanisms manifests in systems with varying degrees of complexity.

[1] This rapid cooling or quenching process is known as a *quench* and will appear throughout the text.

[2] In the Potts model, for example, there are q.

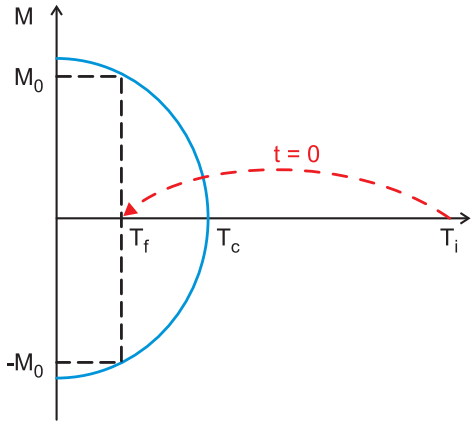


FIGURE 4.1: Schematic of the magnetization of the zero-field Ising model as a function of temperature, showing the spontaneous symmetry breaking at T_c. The arrow illustrates a quench at time $t = 0$ from T_i to T_f (image adapted from [73]).

4.1 Domain growth

The most commonly observed phenomenon in condensed matter for the evolution of a system seeking equilibrium is domain growth. By a *domain* we mean a region of the system dominated by a particular phase, bounded by a domain wall (an interface of dimension $d - 1$), and characterized by a linear size ℓ. In a non-equilibrium situation or within a coexistence region, several domains of different phases may coexist simultaneously, and their characteristic sizes $\ell_i(t)$ carry the information needed to characterize the non-equilibrium mechanisms.

Following a rapid temperature quench from the disordered high-temperature phase into the ordered low-temperature region, the system reorganizes into progressively larger ordered structures. This temporal evolution is governed by thermal, diffusive, and curvature-driven processes, and the effective growth law depends on general characteristics of the system such as the presence of quenched disorder, the dimensionality of the order parameter, and whether it is conserved or not.

4.1.1 Scaling hypothesis

The scaling hypothesis states that, at long times in a macroscopic system, there exists a unique characteristic length scale $\ell(t)$ such that the domain structure is (in a statistical sense) time-independent when all lengths are rescaled by $\ell(t)$. Concretely, the pair correlation function $C(\mathbf{r}, t) = \langle \phi(\mathbf{x} + \mathbf{r}, t)\phi(\mathbf{x}, t) \rangle$ and its Fourier

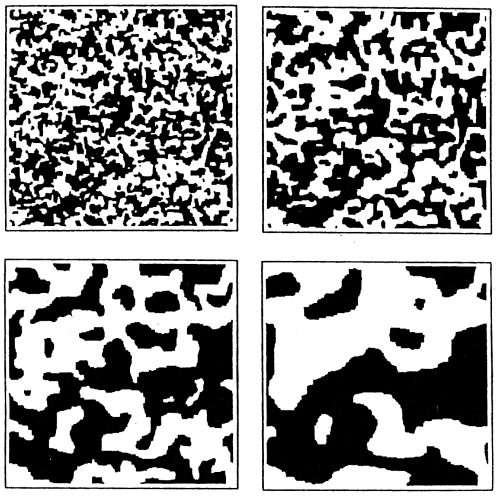


FIGURE 4.2: Monte Carlo simulations of domain growth in the 2d Ising model at $T = 0$, after a quench from $T = \infty$. Black encodes regions of *up* spins, white for *down* spins. The system is 256×256 spins and images correspond to 5, 15, 60, and 200 MCS (top to bottom, left to right). Image taken from [73].

transform (the structure factor $S(\mathbf{k}, t)$) take scaling forms:

$$C(\mathbf{r}, t) = f(r/\ell), \qquad S(\mathbf{k}, t) = \ell^d \, g(k\ell). \tag{4.1}$$

One of the fascinating consequences of phase-ordering kinetics is that, in the thermodynamic limit, the final equilibrium state is never fully reached — the longest relaxation time diverges with system size in the ordered phase, reflecting ergodicity breaking. Instead, an intricate network of domains of the equilibrium phases forms, with the characteristic length scale growing with time. The sequence of domain patterns observed at successive times resembles a spatial zoom-in sequence, manifesting the dynamic scaling hypothesis.

4.1.2 Coarsening

Many domain-growth processes are governed by curvature-driven growth (coarsening), where thermal effects play a secondary role. Phenomenological equations for the time evolution of the coarse-grained order parameter are obtained from a Landau free-energy functional [73]:

$$F[\phi] = \int d^d x \left[\frac{1}{2} |\nabla \phi|^2 + V(\phi) \right], \tag{4.2}$$

with a double-well potential. Two cases are distinguished: conserved and non-conserved order parameter.

Conserved order parameter (Cahn–Hilliard equation):

$$\begin{aligned} \frac{\partial \phi}{\partial t} &= \nabla^2 \frac{\delta F}{\delta \phi} \\ &= -\nabla^2 [\nabla^2 \phi - V'(\phi)]. \end{aligned} \tag{4.3}$$

Characteristic of phase separation in binary alloys, where the total number of each species is conserved.

Non-conserved order parameter (time-dependent Ginzburg–Landau / model A):

$$\begin{aligned} \frac{\partial \phi}{\partial t} &= -\frac{\delta F}{\delta \phi} \\ &= \nabla^2 \phi - V'(\phi). \end{aligned} \tag{4.4}$$

Characteristic of order–disorder or ferromagnetic–paramagnetic transitions. The same equations with Langevin thermal noise on the right-hand side are known as model B and model A respectively in the Hohenberg–Halperin classification [74].

For the non-conserved case, Allen and Cahn [75] derived from (4.4) the local interface velocity:

$$v = -\nabla \cdot \hat{g} = -K\,, \tag{4.5}$$

where v is the wall velocity in the direction of increasing ϕ, $\hat{g}$ is a unit vector normal to the wall surface, and $K \equiv \nabla \cdot \hat{g}$ is $(d-1)$ times the mean curvature of the wall. According to this law, all interfaces move with a local velocity proportional to the local curvature, directed toward lower curvature, so interfaces tend to shrink and disappear.

The scaling hypothesis suggests an intuitive derivation of growth laws for $\ell(t)$. If there is a unique characteristic length ℓ, the wall velocity scales as $v \sim d\ell/dt$ and the curvature as $K \sim 1/\ell$. Substituting and integrating gives $\ell(t) \sim t^{1/2}$ for non-conserved scalar fields (model A). For conserved fields an analogous argument [76] gives $\ell(t) \sim (\sigma t)^{1/3}$.

Inspired by the analogy with critical phenomena, we write the general scaling law:

$$\ell(t) \propto t^n. \tag{4.6}$$

Two universality classes have been delineated: $n = 1/2$ (Lifshitz–Allen–Cahn law [77,78], for non-conserved order parameter, e.g. the Ising model with Glauber dynamics) and $n = 1/3$ (Lifshitz–Slyozov law [79], for conserved order parameter, e.g. spinodal decomposition in binary fluids).

4.1.3 Activated processes and logarithmic growth

Not all scalar-field models fall within the two universality classes described above. Systems with quenched disorder (such as the random-field or random-bond Ising model) exhibit logarithmically slow coarsening. More generally, Lai, Mazenko, and Valls [80] classified domain-growth kinetics into four classes based on how free-energy barriers F_B grow with ℓ:

- **Class 1** (no barriers): $\ell(t) \sim t^{1/2}$, persisting even at $T = 0$. Canonical example: Ising model with spin-flip dynamics.
- **Class 2** (barriers independent of ℓ): For a unique barrier height F_B, $\ell(t) = \sqrt{\ell_0^2 + a_0 t/t_a(T)}$, where $t_a(T) = e^{F_B/k_B T}$ is the activation time. At long times crosses over to power-law growth $\ell \sim t^{1/2}$ (with strongly temperature-dependent prefactor).
- **Class 3** (barriers linear in ℓ): $\ell(t) \sim (T/f_B)\ln(t)$. Typical of the random-field Ising model.
- **Class 4** (barriers $\propto \ell^m$, $m \neq 1$): $\ell(t) \sim T[\ln(t)]^{1/m}$. Typical of spin glasses and systems with frozen disorder.

When curvature-driven growth is insufficient, thermally activated processes allow relaxation via an Arrhenius law [81]:

$$t_a^i \propto \exp[F_i/k_B T]. \tag{4.7}$$

We will encounter this type of behavior in Chapter 8.

4.1.4 Nucleation

As discussed in Chapter 2, the presence of metastable states associated with a first-order phase transition induces a two-timescale relaxation. The most widely accepted mechanism for the decay of a metastable state to equilibrium is *nucleation* of the stable phase.

Classical Nucleation Theory

The standard framework [11] considers droplets as macroscopic objects described by a volume term and a surface term. Classical Nucleation Theory (CNT) postulates that a droplet of radius R of the stable phase appears with probability $P(R)$ proportional to the Boltzmann factor:

$$P(R) \sim g(L)\exp[-\beta \Delta F(R)], \tag{4.8}$$

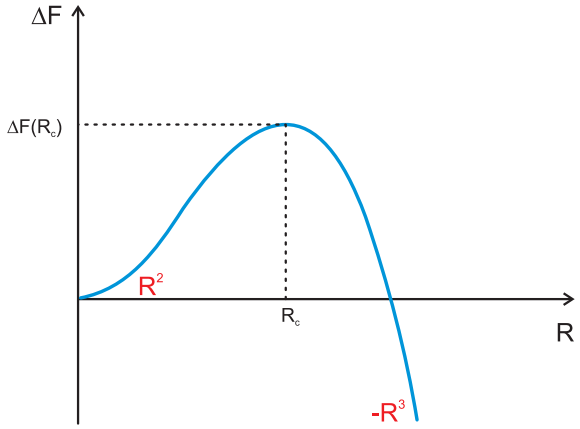


FIGURE 4.3: Excess free energy (4.9) from a droplet of one phase in a sea of the other, for $d = 3$. A droplet spontaneously formed by fluctuations with radius greater than R_c will grow; otherwise it shrinks.

where $g(L)$ is a non-exponential prefactor (in principle a function of the system linear size L) and $\Delta F(R)$ is the excess free energy due to the droplet:

$$\Delta F(R) = a(f_1 - f_2)R^d + bsR^{d-1} \tag{4.9}$$

where s is the surface (interface) tension, f_1 and f_2 are the free energies per unit volume inside and outside the droplet respectively, and a and b are positive geometric constants. Since $(f_1 - f_2) < 0$, there is a competition between the volume and surface terms. The critical radius

$$R_c = \frac{bs(d-1)}{a(f_2 - f_1)d} \tag{4.10}$$

is a maximum of $\Delta F(R)$ (see Fig. 4.3). Droplets with $R > R_c$ grow and invade the system; those with $R < R_c$ shrink and dissolve.

CNT postulates that the nucleation time $t_n(L)$ is inversely proportional to the probability of generating a critical droplet:

$$t_n(L) \propto g(L)^{-1} \exp(\beta \Delta F(R_c)) \tag{4.11}$$

The L-dependence of the nucleation time (4.11) is observed only in not-too-large systems ($L \gtrsim R_c$), the so-called "nucleation regime," where a single droplet forms and expands to cover the whole system. In 2D, $g(L) \sim L^2$ in this regime [52]. At larger sizes ($L \gg R_c$) many droplets form simultaneously in different regions and coalesce — the "coalescence regime," in which the equilibration time becomes size-independent.

Extensions of CNT

The basic CNT considers only spherical droplets in a homogeneous "sea" of the other phase (homogeneous nucleation). In inhomogeneous systems, impurities, vacancies, or system boundaries act as nucleation centers where the effective surface energy is lower, so nucleation occurs with higher probability (heterogeneous nucleation). Extensions incorporating anisotropic surface tensions and non-spherical droplets also exist; in those cases the equilibrium shape of the critical droplet is given by the Wulff construction [82].

"Non-classical" nucleation

Several non-classical nucleation theories exist, including scaling theories, density-functional theories, and diffuse-interface theories [83]. We anticipate here a comment based on our own evidence about the nucleation mechanism in the q-state Potts model.

While CNT assumes that droplets of the stable phase form in the metastable sea purely by thermal fluctuations, our preliminary evidence indicates that *before* the critical nucleus appears, spatial correlations begin to grow in the system, constituting strong "precursor effects" for nucleation. The nucleation time would then be associated not with the waiting time for the spontaneous appearance of a critical-radius droplet, but rather with a collective, self-organized process of spins in a region of the system driven by growing spatial correlations.

4.1.5 Two dynamical scenarios — or more?

A common assumption in the literature on first-order phase transitions is that a quench from high temperature leads to either nucleation (if the quench endpoint lies between the coexistence curve and the spinodal) or coarsening (if it lies beyond the spinodal). The expectation is that the size of the nucleation region grows with the strength of the first-order transition: for a strong transition the nucleation region is wide, while for a weak one the coarsening regime is more likely to be reached.

As we shall see in Chapter 8, this binary picture is, at least, incomplete — even in simple systems like the Potts model. At long times the dynamics depends strongly on the quench temperature range. Additional characteristic temperatures beyond the spinodal enter the dynamics, and several distinct dynamical regimes can be identified.

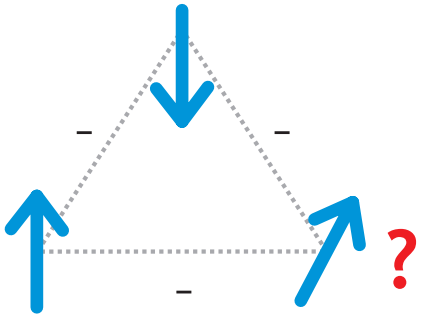


FIGURE 4.4: Typical example of frustration in magnetic spin systems: three spins are placed at the vertices of an equilateral triangle and interact antiferromagnetically. Once two of them are anti-aligned, the third is frustrated.

4.2 Frustration

In certain situations the dynamics of a system can be impeded by local phenomena that prevent relaxation to equilibrium. This is the case of geometric frustration or intrinsic disorder, as in spin glasses. Below, we briefly review geometric frustration and introduce the concept of *dynamical* (or spontaneous) *frustration*, for which pre-existing disorder in the model is not required.

4.2.1 Geometric frustration

Geometric frustration (or simply frustration) in condensed matter refers to the phenomenon in which the geometric properties of the crystal lattice and/or competing interatomic interactions prevent the simultaneous minimization of all interaction energies at a given site.

A simple example is shown in Fig. 4.4: three spins with antiferromagnetic interactions at the vertices of a triangle. Once two are antiparallel, the third cannot be antiparallel to both neighbors simultaneously. Replicating this triangle into a lattice yields a highly degenerate ground state with nonzero zero-temperature entropy.

Frustration is also present in spin-glass models (the Edwards–Anderson $\pm J$ model), where stochastic disorder in the interactions plays the key role [84], and in spatially modulated magnetic superstructures (the ANNNI model) [85].

For completeness: we distinguish between *quenched* (frozen) disorder, where the interaction parameters are random variables that do not evolve in time, and *annealed* disorder, where these variables can change with time.

4.2.2 Dynamical frustration

In certain situations, even when a well-defined, non-frustrated ground state exists, the dynamics can trap the system in a frustrated state from which equilibrium is never reached — a phenomenon we term *dynamical* (or spontaneous) *frustration*.

A first example is the 3D Ising model quenched to $T = 0$: contrary to naive expectation, the system never orders and persists indefinitely in a topologically complex state of interpenetrating regions of positive and negative magnetization, containing "blinkers" — spins that flip *ad infinitum* between their two states at zero energy cost [86, 87].

As we shall see in Chapter 8, analogous dynamically frustrated states arise at low temperatures in the 2D Potts model for $q > 4$. At $T = 0$ the system never orders, and at low but finite temperatures it remains trapped for very long times in states of planar, rectangular domain walls with truncated vertices occupied by blinkers. Escape from these states requires thermal activation, so the lifetime diverges as $T \to 0$. The origin of dynamical frustration in the Potts model is the high degeneracy of its ground state and the multiplicity of accessible frustrated configurations. Notably, the dynamical frustration grows stronger with increasing q.

This phenomenon is not merely an artifact of model dynamics: glassy freezing by dynamical frustration has been observed experimentally via inelastic neutron scattering in the stoichiometric metallic compound $PrAu_2Si_2$ [88], where the authors attribute freezing not to site disorder or vacancies but to dynamical fluctuations of crystal-field levels that destabilize induced magnetic moments.

The common denominator in all cases of dynamical frustration is the *multiplicity* of accessible frustrated states — from a thermodynamic perspective, they have significant measure in phase space and are observed for entropic reasons.

CHAPTER 5

SHORT-TIME DYNAMICS IN CRITICAL SYSTEMS

For systems *in equilibrium*, the spatial correlation length diverges at the critical temperature T_c. Microscopic details of the system become irrelevant for large-scale behavior, and a universal scaling form emerges — the hallmark of critical phenomena.

For a *dynamical* system in the *long-time* regime, a universal dynamical scaling form is likewise known to hold. This is because the *correlation time* (the time required for the system to reach equilibrium) diverges and the spatial correlation length is also very large at long times.

For a magnetic system, e.g. the Ising model, the finite-size dynamical scaling form for an observable O is [74, 89]:

$$O(t, \tau, L) = b^{-x} O(b^{-z} t, b^{1/\nu} \tau, b^{-1} L), \tag{5.1}$$

where t is time, $\tau = (T - T_c)/T_c$ is the reduced temperature, L is the system size, b is the scaling factor, x and ν are static exponents, and z is the dynamical exponent. It is worth noting that long-time dynamical scaling is independent of initial conditions.

Consider the two-time autocorrelation function for a spin system $s_i = \pm 1$:

$$A(t, t') = \frac{1}{L^d} \left\langle \sum_i s_i(t') s_i(t + t') \right\rangle. \tag{5.2}$$

In a finite system, $A(t, t')$ decays exponentially with t at the critical temperature ($\tau = 0$):

$$A(t, t') \sim e^{-t/\zeta_t}, \tag{5.3}$$

where ζ_t is the correlation time. This exponential decay is independent of t', and applying the finite-size scaling ansatz Eq. (5.1) to $A(t, t')$ gives:

$$\zeta_t \sim L^z. \tag{5.4}$$

Typically the dynamical exponent is $z \approx 2$ (for instance, for the majority of single-spin-flip Monte Carlo algorithms for the Ising model). As a result, ζ_t grows rapidly with L, the two-time autocorrelation remains close to 1, and it becomes difficult to generate independent configurations with Monte Carlo, and therefore to advance toward equilibrium. This is the well-known *critical slowing down*, which makes equilibrium simulations near a critical point very costly and also affects measurements of dynamical observables.

Traditionally it was thought that this universal scaling behavior only emerged in the long-time limit of the evolution. However, it has been demonstrated in recent years that the scaling hypothesis can be extended to the short-time regime [90, 91], which requires the introduction of one new independent critical exponent.

As we shall see, the validity of this scaling hypothesis in the early stages of the dynamics allows one to locate critical points and their associated exponents without costly equilibrium measurements, but simply through careful observation of the non-equilibrium dynamics of the system. The study of criticality through this short-time scaling is known as *Short-Time Dynamics* (STD).

5.1 Short-Time Dynamics (STD)

In 1989 Janssen et al. [90], using Renormalization Group (RG) techniques with an ϵ-expansion to second-loop order[1], rigorously established for a model-A system (a ϕ^4 Hamiltonian with Langevin dynamics) the following scaling form valid in the *macroscopic short-time regime* for the n-th moment of the magnetization:

$$m^{(n)}(t, \tau, L, m_0) = b^{-n\beta/\nu} m^{(n)}(b^{-z}t, b^{1/\nu}\tau, L/b, b^{\mu}m_0). \tag{5.5}$$

Here m_0 is the initial value of the order parameter and μ is a new, independent universal exponent describing the short-time behavior, while β, ν, and z are the usual critical exponents. This scaling form is valid only for a very small initial magnetization $m_0 \ll 1$.

After its first appearance, the short-time scaling form was validated by numerical simulations [92–94], and shown to be of great generality beyond model-A systems [95, 96].

When discussing universal behavior in the short-time critical dynamics, we must keep in mind that there are two different time scales: the *macroscopic* and the *microscopic*. Universal behavior emerges only after a period of time that is sufficiently long in the microscopic sense — the so-called microscopic time scale t_{mic}, during which the system dynamics sheds its "short-wave" behavior dominated by microscopic details. The scaling form (5.5) is expected to hold for times t such that $t_{mic} \ll t \ll t_{mac}$, where $t_{mac} \sim L^z$. Numerical simulations of various models show t_{mic} to be in the range 10–300 MCS.

In the short-time regime at a critical point, the spatial correlation length is still small in the macroscopic sense and does not induce the same kind of scaling as when it diverges at long times. Nevertheless, a scaling already manifests in the system, attributed exclusively to the large correlation *time* near the critical temperature.

[1] In 2008 Prudnikov et al. [91] extended the proof to third-loop order in the RG description.

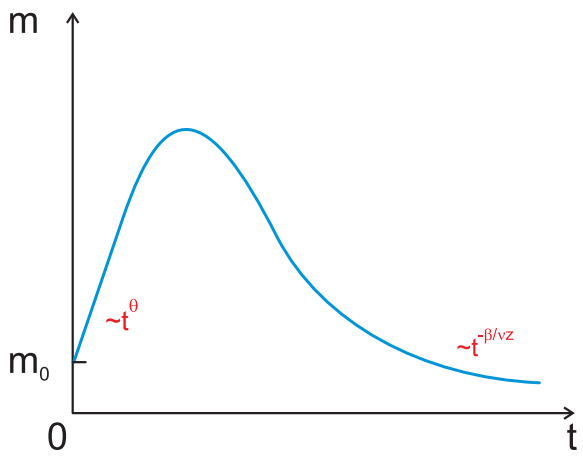


FIGURE 5.1: Schematic of the time evolution of the magnetization near the critical point, starting from a small but nonzero initial value.

5.1.1 Power-law behavior in STD

The scaling properties of short-time dynamics depend on the initial preparation, i.e., on the scalar field m_0.

Disordered initial state ($m_0 \ll 1$)

Starting from Eq. (5.5), in the thermodynamic limit ($L \to \infty$), choosing $b = t^{1/z}$, we obtain for the magnetization ($n = 1$):

$$m(t, \tau, m_0) = t^{-\beta/\nu z} m(1, t^{1/\nu z}\tau, t^{\mu/z} m_0). \tag{5.6}$$

For small values of $t^{\mu/z} m_0$, expanding the right-hand side to first order and using $m(t^{\mu/z} m_0 = 0) = 0$, we obtain:

$$\begin{aligned} m(t, \tau, m_0) &= t^{-\beta/\nu z} t^{\mu/z} m_0 F(t^{1/\nu z}\tau) + O((t^{\mu/z} m_0)^2) \\ &\simeq m_0\, t^{\theta} F(t^{1/\nu z}\tau), \qquad \theta = \frac{\mu - \beta/\nu}{z}. \end{aligned} \tag{5.7}$$

Both RG calculations and simulations observe $\theta \geq 0$. Therefore, at the critical point ($\tau = 0$) one generally observes an initial power-law increase of the magnetization $m \sim m_0 t^{\theta}$, as shown schematically in Fig. 5.1.

This initial increase lasts while $t^{\mu/z} m_0 \lesssim 1$. The magnetization has a maximum near the characteristic time $t_0 \sim m_0^{-z/\mu}$ and then gradually crosses over to the familiar long-time behavior $m(t) \sim t^{-\beta/\nu z}$.

For the second moment ($n = 2$), at the critical point $\tau = 0$:

$$m^{(2)}(t, L, m_0) = b^{-2\beta/\nu} m^{(2)}(b^{-z}t, L/b, b^{\mu}m_0). \tag{5.8}$$

Since $m^{(2)} \sim N^{-1} = L^{-d}$ in the large-L limit (d is the spatial dimension):

$$\begin{aligned} m^{(2)}(t, L, m_0) &\sim (L/b)^{-d} b^{-2\beta/\nu} F(b^{-z}t, b^{\mu}m_0) \\ &\sim \frac{1}{N} b^{d-2\beta/\nu} F(b^{-z}t, b^{\mu}m_0). \end{aligned} \tag{5.9}$$

Choosing $b = t^{1/z}$ and neglecting the m_0 dependence for $m_0 \ll 1$:

$$m^{(2)}(t) \sim N^{-1}\, t^{d/z - 2\beta/z\nu}. \tag{5.10}$$

Furthermore, from (5.7), taking the logarithm and differentiating with respect to τ:

$$\partial_\tau \log m(t, \tau, m_0)|_{\tau=0} = t^{1/\nu z}\, \partial_{\tau'} \log F(\tau')\big|_{\tau'=0}\,, \tag{5.11}$$

with $\tau' = t^{1/\nu z}\tau$. Thus the logarithmic derivative of m (which can be computed numerically as finite differences) also exhibits power-law growth and gives access to the exponent $1/(\nu z)$.

Fully ordered initial state ($m_0 = 1$)

The scaling hypothesis (5.1) also applies when the system starts in the fully ordered state, i.e., $m_0 = 1$.

Consistent with numerical simulation results [95, 97], it is generally assumed that the homogeneity relation

$$m^{(n)}(t, \tau, L) = b^{-n\beta/\nu} m^{(n)}(b^{-z}t, b^{1/\nu}\tau, L/b), \tag{5.12}$$

holds even at short (but macroscopic) time scales.[2]

In the large-L limit:

$$m(t) = t^{-\beta/\nu z} G(t^{1/\nu z}\tau), \tag{5.13}$$

and taking the logarithmic derivative:

$$\left.\frac{\partial \log m(t, \tau)}{\partial \tau}\right|_{\tau=0} \sim t^{1/\nu z}, \tag{5.14}$$

consistent with the disordered initial state case Eq. (5.11).

[2] As we show in Chapter 6, in [2] we provide analytical evidence that this is indeed the case.

5.2 STD as a technique for locating critical points

Looking at Eq. (5.7) for $\tau \neq 0$ but still in the critical region, the power law $m \sim t^{\theta}$ will be modified by the scaling function $F(t^{1/\nu z}\tau)$. This can be exploited to determine the critical temperature.

The method, originally implemented by Schülke and Zheng [98], consists of recording curves of m vs. t for different temperatures, sweeping a wide range of T, in order to identify the temperature at which a power-law behavior is observed at short times.

Starting from a state with $m_0 \ll 1$ but nonzero: if $T < T_c$ the system orders, and does so with a growth of m at short times that is faster than $m \sim t^{\theta}$. If $T > T_c$, m will grow initially but more slowly than $m \sim t^{\theta}$, and before the characteristic time $t_0 \sim m_0^{-z/\mu}$ it will begin to decrease back toward its equilibrium value $m = 0$. These deviations from the $T = T_c$ case, for which the power law holds exactly at short times, are more pronounced the larger $|\tau|$ is. As a result, if one plots m vs. t on a log–log scale for several temperatures (spanning a range including T_c), one observes a "fan" of curves, among which one stands out by exhibiting linear behavior on this scale up to times near t_0. In that same time window, some curves deviate from linearity concavely ($T > T_c$) while others deviate convexly ($T < T_c$).

For the ordered initial state, the procedure is analogous. Now the power law at T_c is decreasing from $m = 1$, and the fan of curves on the log–log scale opens around the straight line $\log m = -\beta/\nu z \, \log t + \text{const}$, which occurs exactly when $\tau = 0$.

Identifying T_c is therefore a very graphical process. In essence, one progressively brackets the temperature between the curves showing one or the other concavity, until a temperature is found that faithfully follows the power law within the estimated error.

In Chapters 6 and 7 we will see examples of the application of the STD technique. To illustrate the fan of curves that allows identification of the critical temperature, Fig. 5.2 shows m vs. t curves for different temperatures for a two-dimensional Heisenberg model with z-direction anisotropy. There it is possible to determine the critical temperature by identifying the curve that after t_{mic} follows a power law without any tendency toward concavity or convexity.

Once T_c is known, independent measurements as functions of time are carried out: m starting from $m_0 \ll 1$, m starting from $m_0 = 1$, and the logarithmic derivative of m with respect to τ. According to Eqs. (5.7), (5.13), and (5.14), fitting

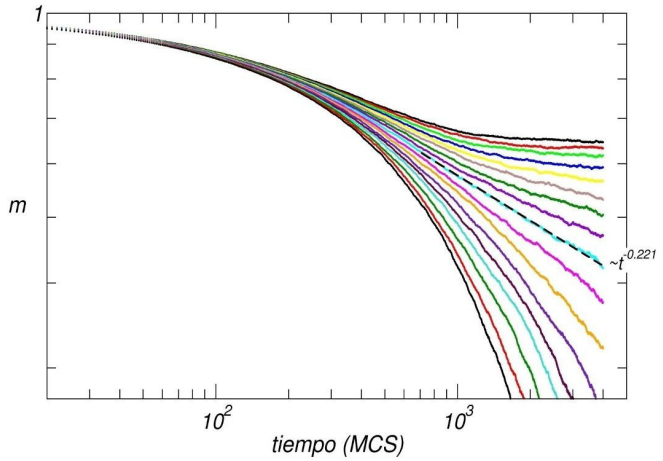


FIGURE 5.2: Example of the determination of T_c for a system with Hamiltonian $H = -J\sum_{<i,j>}\vec{s_i}\cdot\vec{s_j} - D\sum_i (s_i^z)^2$. Curves correspond to different values of T for $D/J = 5$. Using this procedure it is possible to find a second-order line and construct a phase diagram. The curve identified as T_c is highlighted with a dotted line together with the corresponding exponent. Note that for this model $t_{mic} \approx 300$ MCS.

these curves yields the critical exponent combinations $(\mu - \beta/\nu)/z$, $\beta/\nu z$, and $1/\nu z$.

To determine each critical exponent individually, one still needs to identify ν or z separately. This requires the L-dependence of the scaling law. One option [95] is to extract the dynamical exponent z from the finite-size scaling of the time-dependent fourth-order Binder cumulant of the magnetization:

$$U_m(t, L) = 1 - \frac{M^{(4)}}{3\left(M^{(2)}\right)^2} \tag{5.15}$$

Setting $\tau = m_0 = 0$ in (5.5) gives the finite-size relation:

$$U_m(t, L) = U_m(b^{-z}, b^{-1}L) \tag{5.16}$$

and z can be extracted from a collapse of the cumulants [99] for different sizes L.

Although the STD framework has been introduced using a magnetic system with a temperature-driven transition as a paradigm, the entire argument applies in the general case of any phase transition characterized by a generic order parameter m and governed by its associated reduced thermodynamic variable τ.

In Chapters 6 and 7 we will show that the short-time scaling law can be extended to spinodal points in first-order phase transitions.

Part II

Results

CHAPTER 6

SHORT-TIME DYNAMICS IN MEAN-FIELD MODELS

In this chapter we study Short-Time Dynamics for a mean-field model with a non-conserved order parameter (the Curie–Weiss model with Glauber dynamics) by solving the associated Fokker–Planck equation. We obtain closed-form expressions for the first moments of the order parameter near critical and spinodal points, starting from different initial conditions. This allows us to confirm the validity of the Short-Time Dynamics scaling hypothesis in both cases. Although the procedure is demonstrated for a particular mean-field model, our results extend directly to generic models with a single order parameter.

This chapter is based on joint work with Dr. Celia Anteneodo (UFRJ, Brazil) [Anteneodo et al., *J. Stat. Mech.* P07026 (2010)].

6.1 Introduction

As introduced in Chapter 5, in the short-time regime several power laws for the moments of the order parameter follow from the homogeneity relation (5.5), from which critical exponents associated with a second-order transition can be extracted and even the transition point located if unknown.

As noted, while the scaling hypothesis starting from the disordered state was supported by both numerical simulations and RG calculations, its validity for an ordered initial state had only been verified numerically until now.

Additionally, as we shall see in detail in Chapter 7, via numerical simulations we showed [3] that the short-time scaling hypothesis (5.5) holds not only near a critical point, but also near spinodal points in systems with first-order transitions, whether mean-field or short-range models. This is particularly interesting as it suggests the existence of some kind of diverging correlation length associated with the spinodal point.

Since the very concept of a spinodal in systems with short-range interactions remains debated (see Section 2.5), a deeper understanding of the microscopic mechanism behind short-time scaling may shed some light on the problem. One route to this goal is to seek exact solutions for particular models. A first step in this direction is to analyze mean-field models (i.e., with infinite-range interactions), for which the concept of spinodal is well defined. This is the objective of the present chapter: we analyze the exact behavior of short-time relaxation dynamics for mean-field models far from equilibrium with non-conserved order parameter.

Non-equilibrium phenomena in physics are commonly studied using Fokker–Planck equations (FPEs). In particular, aspects of the non-equilibrium dynamics of phase transitions can be analyzed via a FPE associated with the master equa-

tion describing the microscopic dynamics [16,100,101]. This tool has proven very useful in describing relaxation of metastable states [16], finite-size effects [102], and the impact of fluctuations in control parameters [103], and has been applied to mean-field spin models [16, 104] and coupled oscillators [102], among many others.

If the degrees of freedom of the system can be reduced to a few relevant ones, a low-dimensional FPE can be found. Although this description is valid for properties that do not depend on the details of the dynamics (or for mean-field kinetics), many of the conclusions are expected to hold in more general instances.

For a single order parameter m, the FPE for its probability $P = P(m, t|m_0, 0)$ is:

$$\partial_t P = [-\partial_m D_1(m) + \partial_{mm} D_2(m)]\, P \equiv L_{FP}(m) P\,, \tag{6.1}$$

where the drift and diffusion coefficients are determined by the Hamiltonian and the particular dynamics (e.g., Glauber or Metropolis).

Following this stochastic approach, we study here the scaling of the short-time relaxation dynamics in the vicinity of critical and spinodal points.

As a first approximation, the drift coefficient $D_1(m)$ ($= -dV/dm$) is generically linear near a critical point and quadratic at the spinodal, giving rise to quadratic and cubic drift potentials V, respectively. Typically in various models the noise intensity $D_2(m)$ scales as $\epsilon \sim 1/N$ [16, 102]. Thus, although we present STD for a particular spin model, our results can be extended directly to more general mean-field models.

6.2 Formal solution of the FPE and moment expansion

The formal solution of the FPE (6.1), for initial condition $P(m, 0|m_0, 0) = \delta(m - m_0)$, is [105]:

$$P(m, t|m_0, 0) = \mathrm{e}^{t\, L_{FP}(m)} \delta(m - m_0)\,. \tag{6.2}$$

The average of an arbitrary quantity $Q(m)$ can be derived directly from the FPE, via the adjoint Fokker–Planck operator $L^\dagger_{FP}(m) \equiv D_1 \partial_m + D_2 \partial_{mm}$:

$$\begin{aligned} \langle Q \rangle(m_0, t) &= \int Q(m)\, P(m, t|m_0, 0) dm \\ &= \mathrm{e}^{t\, L^\dagger_{FP}(m_0)} Q(m_0) = \\ &= \sum_{k \geq 0} [L^\dagger_{FP}(m_0)]^k Q(m_0)\, t^k/k!\,. \end{aligned} \tag{6.3}$$

The first two moments of the order parameter are then:

$$\begin{aligned} \langle m \rangle &= m_0 + D_1 t + \frac{1}{2}[D_1 D_1' + D_2 D_1'']t^2 + \dots , \\ \langle m^2 \rangle &= \langle m \rangle^2 + 2D_2 t + [2D_2 D_1' + D_1 D_2' + D_2 D_2'']t^2 + \dots , \end{aligned} \tag{6.4}$$

where D_1, D_2 and their derivatives are evaluated at m_0. Note that if D_1 and D_2 are state-independent, the expansion is exact to first order.

Alternatively, evolution equations for the moments can be obtained by integrating Eq. (6.1), after multiplying each side by the quantity to be averaged:

$$\frac{d\langle m^n \rangle}{dt} = n \left\langle m^{n-1} D_1(m) \right\rangle + n(n-1) \left\langle m^{n-2} D_2(m) \right\rangle . \tag{6.5}$$

For $n = 1$:

$$\frac{d\langle m \rangle}{dt} = \langle D_1(m) \rangle . \tag{6.6}$$

Eqs. (6.5) generally lead to a coupled hierarchy of equations for the moments. Only for a few special cases (when D_1 and D_2 are polynomials in m of degree at most one and two, respectively) do these equations decouple. In general, approximate methods are needed to solve the dynamics.

6.3 Paradigmatic mean-field model: Curie–Weiss

We develop our STD analysis for a system of N fully-connected Ising spins (Curie–Weiss model) subject to a magnetic field H, with Hamiltonian:

$$\mathcal{H} = -\frac{J}{2N} M^2 - HM. \tag{6.7}$$

Since the Hamiltonian depends only on the total magnetization M, the master equation for this model can be written in closed form for M [16,104]. In the large-N limit, treating the magnetization per spin $m = M/N$ as a continuous variable, expanding the master equation to first order in the perturbative parameter $\epsilon = 1/N$ leads to a FPE (6.1) for Glauber dynamics with [104]:

$$\begin{aligned} D_1(m) &= -m + \tanh[m'] - \epsilon\beta J m \operatorname{sech}^2[m'] , \\ D_2(m) &= \epsilon\big(1 - m \tanh[m']\big) , \end{aligned} \tag{6.8}$$

where we define $m' = \beta(Jm + H)$, with $\beta = 1/(k_B T)$.

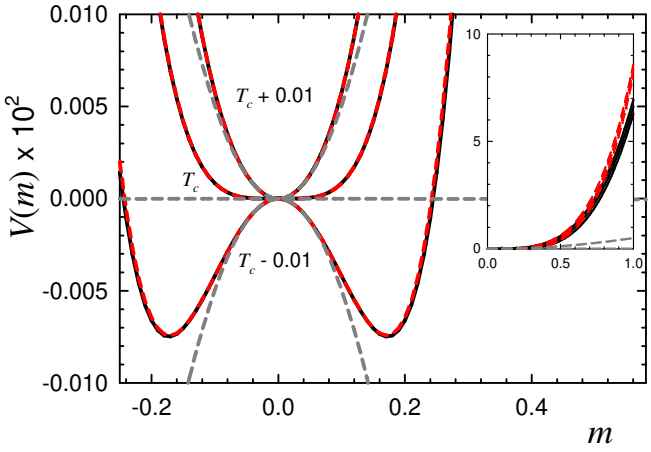


FIGURE 6.1: Drift potential $V(m)$ for different values of T near T_c (as indicated). $V(m)$ was obtained (up to an arbitrary additive constant) by integrating D_1 from Eqs. (6.8) (solid black lines), (6.9) (dashed red lines) and (6.10) (dashed grey lines). Inset: zoom of the region near $m = 1$.

In what follows we derive asymptotic solutions for the FPE with these coefficients, both near the critical point ($H = 0$ and $T \approx T_c = J/k_B$) and near spinodal points for $T < T_c$. We compare analytical results with Monte Carlo simulations using the Glauber algorithm. Time is made dimensionless with the characteristic time t_0 of the transition rate $w = t_0^{-1}(1 + \exp(\beta\Delta\mathcal{H}))^{-1}$. The time unit in theoretical expressions corresponds to one MC step in simulations.

6.4 STD near the critical point

In the vicinity of the critical point (at $T \simeq T_c = J/k_B \equiv 1$ and $H = 0$), the coefficients (6.8) can be approximated for small m (i.e., $\beta J|m| \ll 1$) as:

$$\begin{aligned} D_1(m) &= -\omega(\lambda,\epsilon)\, m - \kappa(\lambda,\epsilon) m^3 + \mathcal{O}(m^5)\,, \\ D_2(m) &= \epsilon\left([1-(1-\lambda)m^2] + \mathcal{O}(m^4)\right)\,, \end{aligned} \tag{6.9}$$

where $\omega(\lambda,\epsilon) \equiv \lambda + \epsilon(1-\lambda)$ and $\kappa(\lambda,\epsilon) \equiv (\frac{1}{3} - \epsilon)(1-\lambda)^3$, with $\lambda \equiv 1 - T_c/T$.

Within the domain of validity of these approximations, $(1-\lambda)m^2 \ll 1$ and therefore $D_2 \simeq \epsilon$. As for D_1, the linear term dominates:

$$D_1(m) \simeq -\omega(\lambda,\epsilon)\, m\,, \tag{6.10}$$

when

$$|\omega| \gg \kappa\, m^2\,. \tag{6.11}$$

This implies a parabolic approximation of the drift potential $V(m) = -\int D_1(m)\, dm$.

6.4.1 Ornstein–Uhlenbeck approximation

For linear D_1 and constant D_2, the exact solution of Eq. (6.1) is [105]:

$$P(m,t|m_0,0) = \frac{1}{\sqrt{2\pi\sigma^2(t)}}\, \exp\left(-\frac{[m - m_0\exp(-\omega\, t)]^2}{2\sigma^2(t)}\right)\,, \tag{6.12}$$

where $\sigma^2(t) = \epsilon[1-\exp(-2\omega t)]/\omega$. This solution applies both for $\omega > 0$ (Ornstein–Uhlenbeck (OU) process) and $\omega < 0$, and is valid as long as the probability distribution remains a sharp peak, so that inequality (6.11) holds for any m with non-negligible probability.

Averaging over distribution (6.12) gives:

$$\langle m\rangle = m_0\exp(-\omega\, t)\,. \tag{6.13}$$

For $\omega > 0$ ($T/T_c > 1 - 1/N$), the mean magnetization decays exponentially with characteristic time $|\omega|^{-1}$. For $\omega < 0$ ($T/T_c < 1 - 1/N$), it grows exponentially. At timescales $t \ll |\omega|^{-1}$, $\langle m\rangle \sim m_0$ persists.

Since in the large-N limit $\omega \sim \lambda$, the magnetization scales as $\langle m\rangle = m_0\, F(\lambda t)$. This is consistent with Eq. (5.7) with $\theta = 0$ and $\nu z = 1$, in agreement with the mean-field exponents $\nu = 1/2$ and $z = 2$.

For higher centered moments $m^{(n)} \equiv \langle (m - \langle m\rangle)^n\rangle$ with $n \geq 2$ even:

$$m^{(n)} = \frac{\Gamma(\frac{n+1}{2})}{\sqrt{\pi}}[2\epsilon\,\omega^{-1}(1 - \exp[-2\omega\, t])]^{\frac{n}{2}}\,. \tag{6.14}$$

At short times $t \ll 1/|\omega|$:

$$m^{(n)} \sim [\epsilon\, t]^{n/2}\,. \tag{6.15}$$

In particular $m^{(2)} \sim t/N$, consistent with Eq. (5.10) with $\beta = 1/2$ and $d = 4$ (the upper critical dimension).

The characteristic timescale for STD behavior is $t \ll \tau_{STD}$ with:

$$\tau_{STD} \approx \frac{1}{|\lambda + \epsilon|} = \frac{N}{|1 + N\,\lambda|}\,. \tag{6.16}$$

If $|\lambda N| \gg 1$ then $\tau_{STD} \sim 1/|\lambda| \ll N$; if $|\lambda N| \ll 1$ then $\tau_{STD} \sim N$.

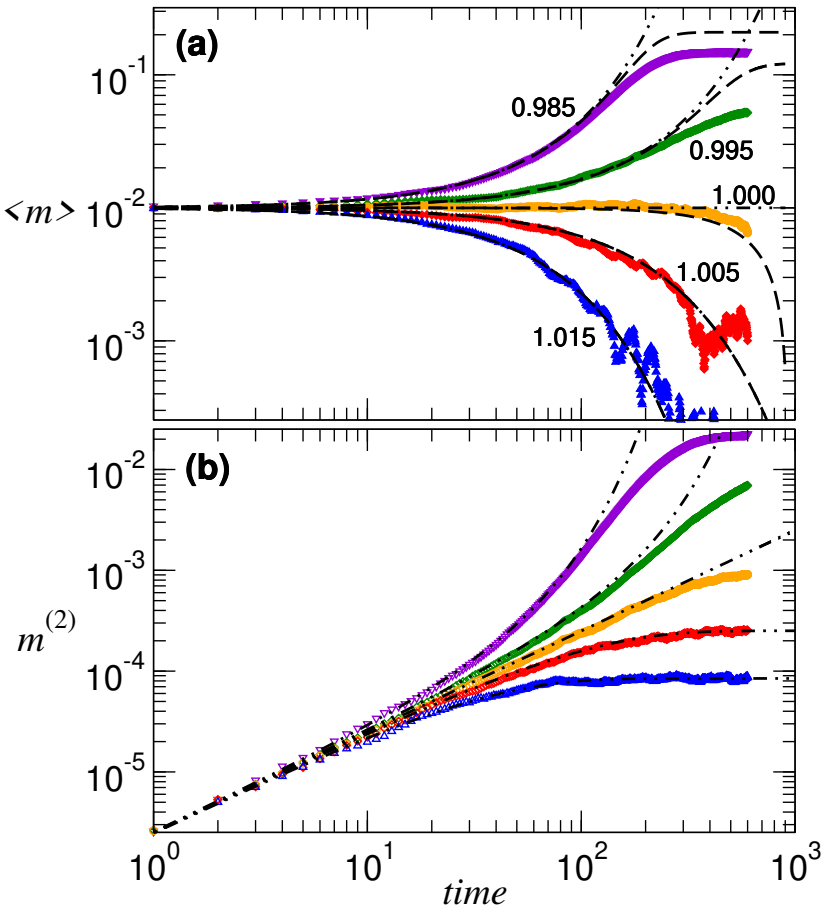


FIGURE 6.2: First and second moments of the order parameter as a function of time t, for $m_0 = 0.01$ and different values of $T \simeq T_c = 1$. (a) Magnetization: dash-dot lines correspond to Eq. (6.13) and dashed lines to Eq. (6.17). (b) Second moment: dash-dot lines correspond to Eq. (6.14). Numerical simulations used Glauber dynamics for $N = 8 \times 10^5$ (colored symbols).

Fig. 6.2 shows a comparison between numerical simulations and the OU approximation, Eqs. (6.13) and (6.14), for $N = 8\times10^5$, $m_0 = 0.01$, and various values of $T \simeq T_c$ with $|\lambda N| \gg 1$. The OU approximation shows very good agreement with simulations for timescales up to $t \sim \tau_{STD}$. Curves are averages over 1000 independent realizations.

6.4.2 Quartic drift potential approximation

When (6.11) does not apply, the cubic contribution to D_1 cannot be discarded. As shown in Appendix A.1, including the cubic correction in the drift coefficient (6.9) leads, for $\epsilon \ll 1$, to:

$$\langle m\rangle = \frac{m_0 \mathrm{e}^{-\omega t}}{\sqrt{1 + m_0^2\kappa(1-\mathrm{e}^{-2\omega t})/\omega}}\,. \tag{6.17}$$

This solution is exact in the thermodynamic limit $\epsilon \to 0$, as can be verified by direct integration of the deterministic version of Eq. (6.6) [16]:

$$\frac{d\langle m\rangle}{dt} = D_1\left(\langle m\rangle\right). \tag{6.18}$$

Note that expanding Eq. (6.17) to first order in m_0 reproduces Eq. (6.13).

In Fig. 6.2 we also show the performance of Eq. (6.17), which reproduces simulation results at longer times, predicting the stable state. The saturation level observed in simulations for $T < T_c$, lower than predicted by (6.17), is due to fluctuations that carry some trajectories to the negative-magnetization equilibrium state, while the deterministic equation stabilizes at the nearest local minimum.

At $T = T_c$ ($\omega = 0$), from Eq. (6.17) in the limit $\omega \to 0$:

$$\langle m\rangle = \frac{m_0}{\sqrt{1 + 2m_0^2\kappa t}}\,. \tag{6.19}$$

As shown in Appendix A.1, finite-size corrections do not change the STD scaling of $\langle m\rangle$.

For the second moment:

$$m^{(2)} \equiv \langle m^2\rangle - \langle m\rangle^2 = 2\epsilon t\frac{(1+z)(1+2z+2z^2)}{(1+2z)^3} + \mathcal{O}(\epsilon^2, \epsilon\omega)\,, \tag{6.20}$$

where $z \equiv \kappa m_0^2 t$. Up to a typical timescale $1/(2\kappa m_0^2)$, the approximation $m^{(2)} \simeq 2\epsilon t$ holds. For $\kappa m_0^2 t \gg 1$, a crossover to a second diffusive regime with a different coefficient $m^{(2)} \simeq \epsilon t/2$ is predicted, though this is typically beyond the STD region.

6.4.3 Other initial conditions

To extend the analytical support for STD scaling to other initial conditions, we analyze the STD behavior when $m_0 = 1$.

As seen in the inset of Fig. 6.1, the cubic approximation is valid even near $m = 1$, so expression (6.17) is also expected to hold in this case, as verified in Fig. 6.3a.

For finite systems, the fluctuation intensity is state-dependent according to Eq. (6.8), so the finite-size corrections derived under $D_2 \simeq \epsilon$ no longer apply. However, at very short times we still expect $m^{(2)} \sim 2D_2(m_0)t$ according to Eq. (6.4), as verified by numerical simulations and illustrated in Fig. 6.3b.

From Eq. (6.17), $m(t) \sim t^{-1/2}(1 - \lambda t)$ for $t \ll 1/|\lambda|$, consistent with Eq. (5.13). The excellent agreement between Eq. (6.17) and simulations confirms our previous assumptions when $|\lambda N| \gg 1$.

6.5 STD near the spinodal

When $T < T_c$ the model has a line of first-order transitions at $H = 0$ and metastable stationary solutions for a range of H values (see schematic Fig. 2.7). Without loss of generality, we restrict ourselves to metastable solutions with positive magnetization — the analytic continuations of the equilibrium magnetization from positive to negative H. Defining $h \equiv \beta H$, the metastable state exists while $h > h_{SP}$, where the spinodal field is given by:

$$\begin{aligned} h_{SP} &= -\beta J m_{SP} + \frac{1}{2} \ln \frac{1 + m_{SP}}{1 - m_{SP}} \\ m_{SP} &= \sqrt{1 - \frac{1}{\beta J}} \, . \end{aligned}$$

Suppose we start the evolution from the fully ordered state $m_0 = 1$, with $T < T_c$ and $h > h_{SP}$, and define $\Delta m \equiv m - m_{SP}$ and $\Delta h \equiv h - h_{SP}$. Treating Δm as an order parameter, as we shall see in Chapter 7, numerical simulations show that close to the spinodal ($|\Delta h| \ll 1$), its moments obey the scaling form (5.12) with $\tau = \Delta h / h_{SP}$.

For temperatures sufficiently close to T_c, the spinodal magnetization m_{SP} is close to 1 and we can expand D_1 and D_2 in powers of Δh and Δm. Near the spinodal we can also neglect finite-size corrections to D_1 [104]. From Eqs. (6.8),

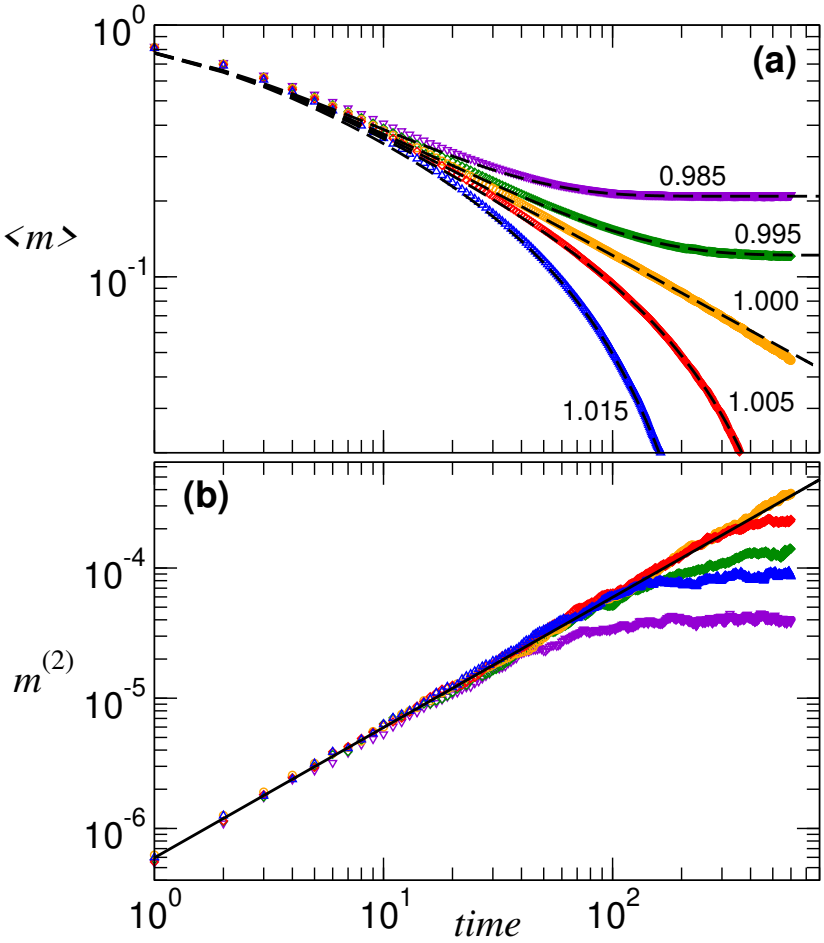


FIGURE 6.3: First and second moments as a function of t for $m_0 = 1$ and various values of $T \simeq T_c = 1$. (a) Magnetization: dashed lines correspond to Eq. (6.17). (b) Second moment: solid black lines represent $2D_2(m_0 = 1)t$. Numerical simulations used Glauber dynamics for $N = 8 \times 10^5$ (colored symbols).

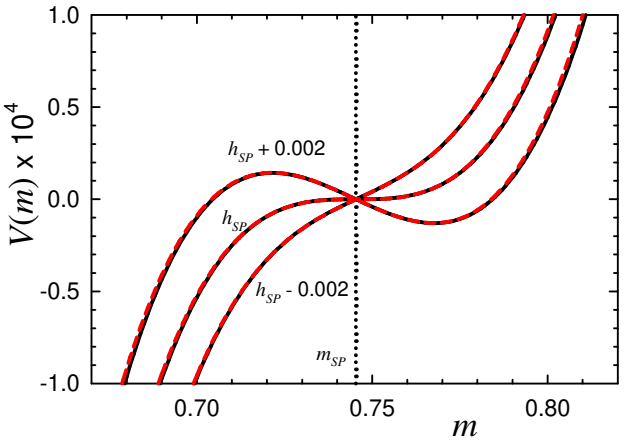


FIGURE 6.4: Drift potential $V(m)$ for different values of h near h_{SP} (as indicated) at $T = 4/9$. Computed (up to a constant) from integrating D_1 in Eq. (6.8) (solid red lines) and in the approximate Eq. (6.21) (dashed black lines).

to first order in Δh and second order in Δm:

$$\begin{aligned} D_1(m) &\simeq \frac{\Delta h}{\beta J} - 2m_{SP}\Delta m\Delta h - \beta J m_{SP}(\Delta m)^2 \,, \\ D_2(m) &\simeq \epsilon\left(\frac{1}{\beta J} - 2m_{SP}\Delta m + (\beta J - 2)(\Delta m)^2 \right. \\ &\quad \left. -\frac{m_{SP}}{\beta J}\Delta h + (2 - \frac{3}{\beta J})\Delta m\Delta h\right) . \end{aligned} \tag{6.21}$$

The moments of Δm are computed from Eq. (6.3):

$$\langle(\Delta m)^n\rangle = \sum_{k\geq 0}[D_1\partial_x + D_2\partial_{xx}]^k x^n\, t^k/k! \,, \tag{6.22}$$

where $x \equiv m_0 - m_{SP}$.

For $n = 1$ we can neglect the diffusive term to leading order (ignoring finite-size effects at short times). Using $D_1 = -A(x^2 + 2A\alpha x - \alpha)$ in Eq. (6.22), with $\alpha = \Delta h/(\beta J A)$ and $A \equiv \beta J m_{SP}$, one obtains (see Appendix A.2):

$$\langle\Delta m\rangle = \sqrt{\gamma}\,\frac{u + \tanh(\sqrt{\gamma}At)}{1 + u\,\tanh(\sqrt{\gamma}At)} - A\alpha \,, \tag{6.23}$$

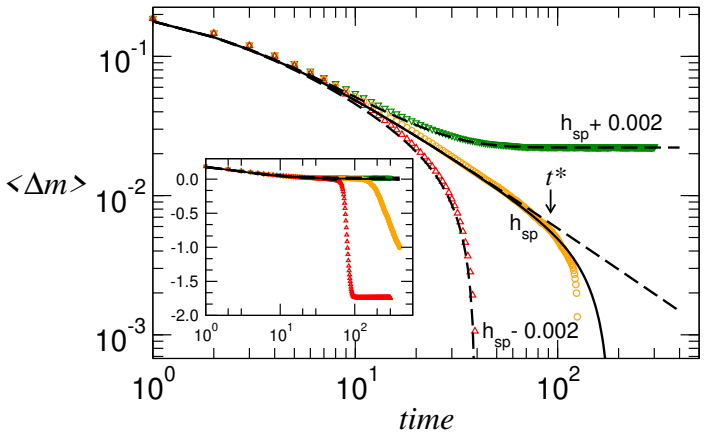


FIGURE 6.5: Mean magnetization as a function of time t, for $m_0 = 1$, $T = 4/9$, and different values of h. Dashed black lines: prediction of Eqs. (6.23), (6.24), and (6.25). Solid black lines: Eq. (A.8). Inset: same data on linear-logarithmic scale. Numerical simulations for $N = 8 \times 10^5$ (colored symbols).

where $u = (x + A\alpha)/\sqrt{\gamma}$ and $\gamma = \alpha + A^2\alpha^2$. For $\alpha < 0$ ($\gamma < 0$), Eq. (6.23) becomes:

$$\langle \Delta m \rangle = \sqrt{|\gamma|}\, \frac{u - \tan(\sqrt{|\gamma|}At)}{1 + u\, \tan(\sqrt{|\gamma|}At)} - A\alpha\,. \tag{6.24}$$

These can also be obtained by integrating Eq. (6.18). As illustrated in Fig. (6.5), they agree well with numerical simulations. One observes:

(i) For $|h| < |h_{SP}|$ ($\alpha > 0$): a plateau is reached since the potential has a local minimum, consistent with simulations (Fig. 6.5).

(ii) For $|h| > |h_{SP}|$ ($\alpha < 0$): Eq. (6.24) gives a rapid decay reaching zero at finite t, since the potential is tilted toward the absolute minimum with no local minimum.

In the limit $\alpha \to 0$, from Eq. (6.23):

$$\langle \Delta m \rangle = \frac{x}{1 + Axt}\,. \tag{6.25}$$

At the spinodal we have $\langle \Delta m \rangle(t) \sim t^{-1}$ for $t \gg 1/Ax$, consistently with Eq. (5.13) with $\beta = 1/2$ and $\nu z = 1/2$. This behavior corresponds to relaxation toward the saddle point $m = m_{SP}$. While in an infinite system this is a stationary point, finite-size fluctuations destabilize it, with a consequent exponential relaxation toward equilibrium at long times.

Including the diffusive term in Eq. (6.22) gives finite-size corrections to Eq. (6.25), computed in Appendix A.2 as Eq. (A.8). For $t \gg 1/Ax$:

$$\langle \Delta m \rangle \sim \frac{1}{At} \left[1 - \frac{\epsilon\, c\, A^2}{10}\, t^3 + \mathcal{O}(\epsilon t^2, \epsilon^2) \right] . \tag{6.26}$$

Finite-size effects become relevant only when $t \sim t^*$, with:

$$t^* = \left(\frac{10\beta J}{\epsilon A^2} \right)^{1/3} = \left(\frac{10\, N}{-\lambda} \right)^{1/3} , \tag{6.27}$$

consistent with the scaling proposed in [3] and verified numerically in Chapter 7: $t^* \propto N^{z/d_c}$, with $z = 2$ and $d_c = 6$.

For the second moment, Appendix A.2 gives Eq. (A.10), from which $\Delta m^{(2)} = \langle (\Delta m)^2 \rangle - (\langle \Delta m \rangle)^2$ is obtained via Eq. (A.11). At short times $t \ll 1/Ax$:

$$\Delta m^{(2)} \sim 2\epsilon(ax^2 + bx + c)\, t \simeq 2D(x)\, t\,, \tag{6.28}$$

consistent with Eq. (6.4). For $t \gg 1/Ax$:

$$\Delta m^{(2)} \sim \frac{2\epsilon c t}{5}\,. \tag{6.29}$$

The crossover between the two diffusive prefactors is illustrated in Fig. (6.6) for different values of m_0 at fixed temperature. The short-time prefactor $2D_2(m_0)$ varies with m_0 (panel a), while at intermediate times $1/Ax \ll t < t^*$ the prefactor becomes $\frac{2}{5}\epsilon c = \frac{2\epsilon}{5\beta J}$ independently of m_0, as evident on the linear scale (panel b).

In any case, the behavior $\Delta m^{(2)} \sim \epsilon t$ up to $t \sim t^*$ is consistent with the STD scaling hypothesis for the mean-field exponent set $z\nu = 2$, $\beta = 1/2$, $d_c = 6$, and agrees with simulation results.

6.6 Chapter conclusions

We studied Short-Time Dynamics for finite-size mean-field (infinite-range) systems with non-conserved order parameter dynamics. Solving the associated Fokker–Planck equation, we obtained closed-form expressions for the first moments of the order parameter near both critical and spinodal points. This allowed us to confirm the STD scaling hypothesis analytically in both cases and to determine its dynamic range of validity.

In particular, we confirmed analytically — for the first time — the validity of the STD scaling hypothesis when the system starts from an ordered initial

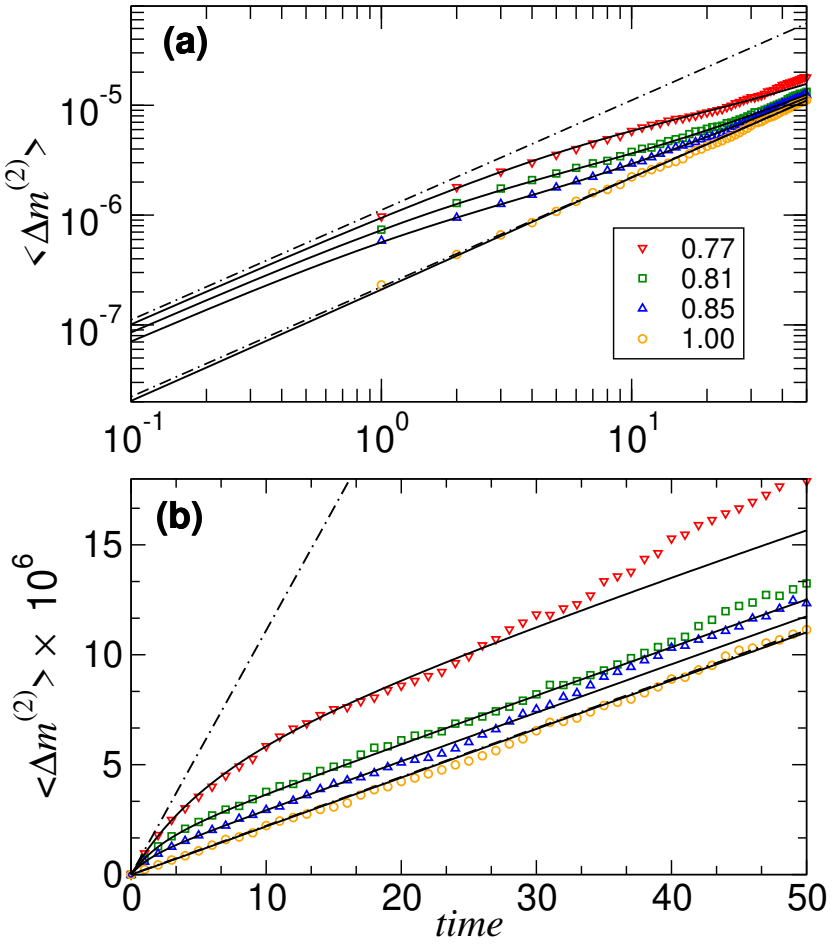


FIGURE 6.6: Second moment of the order parameter as a function of t, for $T = 4/9$, $h = h_{SP}$, and different values of m_0 (with $m_{SP} < m_0 < 1$). Panels (a) and (b) show the same data on logarithmic and linear scales, respectively. Solid black lines: prediction of Eq. (A.10). Symbols: MC simulations for $N = 8 \times 10^5$. Dash-dot lines: $2D_2(m_{sp})t$ (upper) and $\frac{2}{5}c\epsilon t$ (lower).

state. We also found that the diffusive scaling of the second moment holds for any initial value of the order parameter, with the diffusion coefficient exhibiting a crossover between two values at short and intermediate times within the STD regime.

The scaling of the first moment is governed primarily by the drift potential $V(m) = -\int D_1(m)\, dm$, and hence by the extended free energy $f_3(T, H, m)$, which has the same extremal structure as [16] $V(m)$. The scaling of higher moments, on the other hand, originates in the Gaussian character of finite-size fluctuations near singular points. Although our results were obtained for a specific model, they depend only on the form of $V(m)$ and the proportionality $D_2 \propto 1/N$, making them of broad applicability to generic mean-field models.

CHAPTER 7

METASTABILITY IN THE TWO-DIMENSIONAL q-STATE POTTS MODEL

The problem of the existence of metastability in the thermodynamic limit for the q-state Potts model is a long-standing and well-known problem in Statistical Mechanics. In this chapter we address this problem in depth, providing consistent numerical evidence for the existence of metastability from several complementary perspectives.

The chapter is divided into two parts:

In the **first part** we show that it is possible to obtain a meaningful definition of spinodal points from the short-time dynamical behavior of the system, deep inside its metastable phase, by identifying the point at which it displays critical dynamical behavior. We demonstrate that the spinodal points obtained by this method are consistent with the thermodynamic spinodal in mean-field systems and with the pseudospinodal in short-range systems. This definition allows, in general, a practical determination of the spinodal point without facing the difficulties of equilibrating the system in the metastable state. In particular, we apply this technique to obtain spinodal temperatures in the q-state Potts model. These turn out to differ from the transition temperature for $q > 4$, defining an allowed metastability region.

In the **second part** we reinforce the numerical evidence for the existence of metastability associated with the first-order phase transition in the Potts model, based on a criterion proposed by Binder [106]. To this end we implement a novel high-performance parallel numerical tool based on the use of graphics cards as computing engines.

As a complement, we investigate the phenomenon of nucleation as the relaxation mechanism from a metastable state to the equilibrium state, which shows certain non-trivial characteristics.

The first and second parts of this chapter are based respectively on a work in collaboration with Drs. Ernesto Loscar and Tomás Grigera of INIFTA (La Plata) [Loscar et al., *J. Chem. Phys.* **131**, 024120 (2009)] and on a work in collaboration with Mr. Juan Pablo De Francesco and Lic. Nicolás Wolovick of FaMAF [Ferrero et al., submitted to *Comp. Phys. Commun.* (2011)].

7.1 Introduction

In Chapter 2 we discussed the concepts of thermodynamic spinodal, pseudospinodal, and metastability limit. We saw that in mean-field systems the spinodal point is well defined, while in systems with a finite range of interactions the phenomenology is more complex. From (meta)equilibrium measurements deep inside the metastable region, and via extrapolations, it is possible to locate diver-

gences of quantities such as the susceptibility and the relaxation time, and hence a pseudospinodal. However, these measurements are not always practical, since the metastability limit intervenes and equilibrating the system in the metastable stationary state becomes impossible. We therefore proposed, rather than abandoning the idea of a spinodal in finite-range systems, to *define* it through out-of-equilibrium properties of the system.

The fundamental hypothesis underlying this study is that a spinodal point has characteristics analogous to those of a critical point: the growth of response functions (e.g., susceptibility) and of the relaxation time near a spinodal suggests the existence of a growing correlation length (whether divergent or not). Consequently, the homogeneity relations associated with critical phenomena are expected to hold in this situation as well.

It is known, as we have seen, that critical points can be detected by studying the short-time dynamical behavior of the order parameter and correlation functions [90, 97]. We propose to use the same method to identify a point well inside the metastability region that behaves, at short times, like a critical point. This pseudocritical regime (in the sense that it lasts only a finite time) does not necessarily imply the existence of a thermodynamic singularity.

To justify our proposal we show, in a mean-field model where the spinodal point is perfectly defined and can be computed analytically, that the point identified by this technique is precisely the thermodynamic spinodal. Defining the spinodal as the point at which this pseudocritical dynamics occurs, we provide a meaningful generalization of the concept of spinodal to finite-range systems.

We apply the method to the two-dimensional q-state Potts model [25] with $q > 4$, where it yields a meaningful result, identifying lower and upper spinodal temperatures T_{sp}^{-} and T_{sp}^{+}, both distinct from the transition temperature T_t, thereby providing a bound for the metastability limit. The technique has the advantage of not requiring equilibrium measurements, which are an essential prerequisite for determining the pseudospinodal.

Moreover, the spinodal only provides a bound on the metastability limit, and the question of whether metastability actually exists or not in the Potts model at infinite size remains controversial. While this phenomenon is clearly observed in finite systems, its persistence in the thermodynamic limit is still an open problem [3, 51, 60, 106, 107]. In one of the first works on the topic, Binder proposed a numerical criterion to determine whether metastability persists in the thermodynamic limit, based on the finite-size scaling properties of the average energy per site in the vicinity of the transition temperature [106]. However, a very narrow

range of temperatures in the metastable region makes high-precision calculations necessary for the criterion to work. In particular, to reduce finite-size rounding and statistical errors below an appropriate level, sufficiently large system sizes are needed.

To address this problem we implemented a parallel code to perform Monte Carlo simulations of the Potts model based on the use of GPUs (Graphics Processing Units), described in Appendix C. This algorithm allowed us to simulate systems of up to $N = 32768 \times 32768 \approx 1.073 \times 10^9$ sites, with a speedup of up to $155\times$ over an optimized serial CPU implementation.

With this algorithm we obtained positive numerical evidence for the persistence of metastability in the thermodynamic limit for $q > 4$, in accordance with the Binder criterion.

7.2 Using Short-Time Dynamics to identify spinodal points

In Chapter 5 we described the application of STD for locating critical points and their associated exponents. We now apply the STD method detailed in Section 5.2 in the same way, searching for singular behavior in the metastable region of a first-order phase transition. By tuning the appropriate control parameter (external magnetic field or temperature), we search for a value at which the power laws (5.7), (5.10), and (5.13) hold at short timescales (at very long times the approach to the corresponding equilibrium phase begins to dominate). This value of the control parameter can meaningfully be defined as a spinodal point, as we demonstrate in the cases studied in this section.

7.2.1 STD at spinodal points of systems with long-range interactions

Recalling from Section 2.5.1: we now apply the STD procedure to the Curie–Weiss model (2.15) near the *spinodal* point, using $\Delta m = m - m_{sp}$ as the order parameter. We consider the process at fixed temperature, using the magnetic field as the control variable, starting from the ordered state ($m = 1$). The analogous procedure to a quench near T_c for a second-order transition is to fix h close to $h_{\text{sp}}^{(-)}$. To determine $h_{\text{sp}}^{(-)}$, we assume scaling as in Eq. (5.5) with $\tau = (h - h_{\text{sp}}^{(-)})/h_{\text{sp}}^{(-)}$.

In this test case we can compare the STD-determined spinodal field and mag-

netization against the exact values from Eqs. (2.17) and (2.18):

$$m_{\rm sp}^{(-)} = \sqrt{1 - \frac{T}{J}}, \tag{7.1}$$

$$\beta h_{\rm sp}^{(-)} = \frac{1}{2} \ln \left[\frac{1 + m_{\rm sp}^{(-)}}{1 - m_{\rm sp}^{(-)}} \right] - \frac{m_{\rm sp}^{(-)} J}{T}. \tag{7.2}$$

We simulated the dynamics using a standard Metropolis algorithm on a system of $N = 1.6 \times 10^6$ spins. Starting with all spins up and carrying out $n \sim 10^3$ independent runs recording Δm and the second moment $\Delta m^{(2)}$.

Figure 7.1 shows the short-time behavior of Δm and $\Delta m^{(2)}$ for $T = \frac{4}{9} T_c$, where time is measured in Monte Carlo steps (MCS). From Eqs. (7.1) and (7.2) we have $\beta h_{\rm sp}^{(-)} \approx -0.714627$ and $m_{\rm sp}^{(-)} \approx 0.745356$.

For both the first and second moments [Eqs. (5.10) and (5.13)], power-law behavior $\Delta m \sim t^{-x}$ and $\Delta m^{(2)} \sim t^{y}$ is found at $h = h_{\rm sp}^{(-)}$, with exponents $x = 0.98 \pm 0.02$ and $y = 1.03 \pm 0.02$ respectively. The power laws are somewhat short in time (lasting until $t \sim 100$ MCS) and both observables deviate at longer times, but this is a finite-size effect.

Computing the logarithmic derivative of Δm with respect to the reduced field τ by finite differences at $h = h_{sp} \pm \delta h$ with $\delta h = 2 \times 10^{-4}$:

Figure 7.2 shows that the data fit a power law with exponent $w = 2.02 \pm 0.02$. Using the scaling relations Eqs. (5.13) and (5.14) and the values of x and w, we obtain:

$$\beta = 0.49 \pm 0.01, \tag{7.3}$$

and assuming $d_c = 6$, from Eqs. (5.10) and (5.13):

$$z = 2.01 \pm 0.03, \qquad \nu = 0.249 \pm 0.004. \tag{7.4}$$

In this test case, the STD-determined spinodal field and critical exponents are in excellent agreement with the theoretical results (2.25), (7.1), and (7.2).

We also studied finite-size effects, obtaining an independent estimate of z.

Figure 7.3 shows Δm at the spinodal for system sizes between $N = 1.6 \times 10^2$ and $N = 1.6 \times 10^6$. Defining t^* as the time when Δm first departs from the power law, and using the correlation-length argument $t^* \propto N^u$ with $u = z/d_c$, a fit gives $u = 0.34 \pm 0.01$, yielding $z = 2.06 \pm 0.06$ — in excellent agreement with the previous estimate.

We conclude from this test that the STD technique correctly identifies spinodal (thermodynamic) points, consistent with equilibrium results. We now proceed to a short-range model.

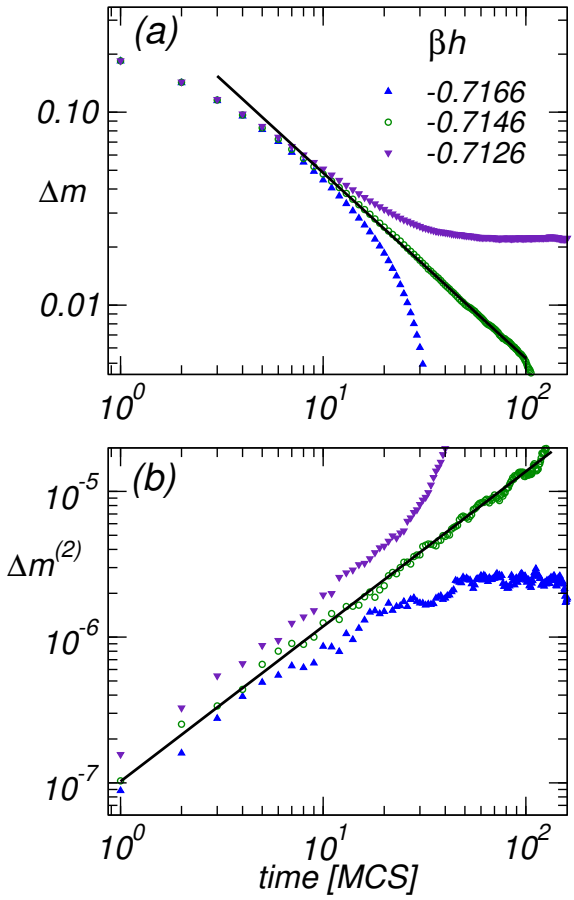


FIGURE 7.1: Short-time dynamics of the first and second moments of Δm for the Curie–Weiss Ising model at $T = \frac{4}{9}T_c$ and different magnetic fields. Solid (black) lines correspond to power-law fits at $h = -0.7146 = h_{\rm sp}^{(-)}$.

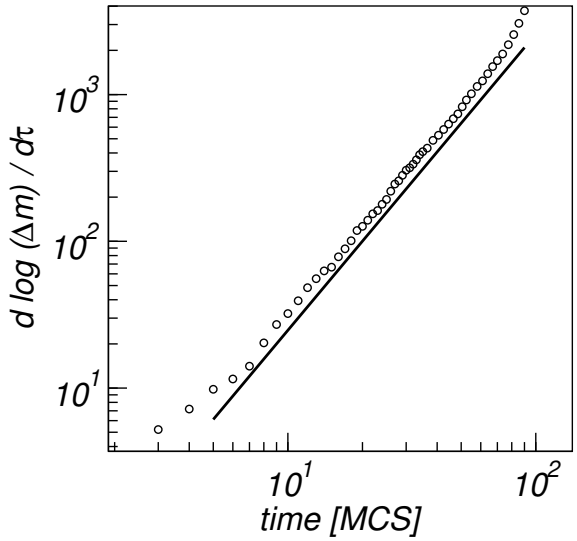


FIGURE 7.2: Short-time behavior of the logarithmic derivative of $\log \Delta m$ with respect to $\tau \equiv (h - h_{\rm sp}^{(-)})/h_{\rm sp}^{(-)}$ evaluated at $\tau = 0$; the solid line corresponds to a power law with exponent $w = 2.02$.

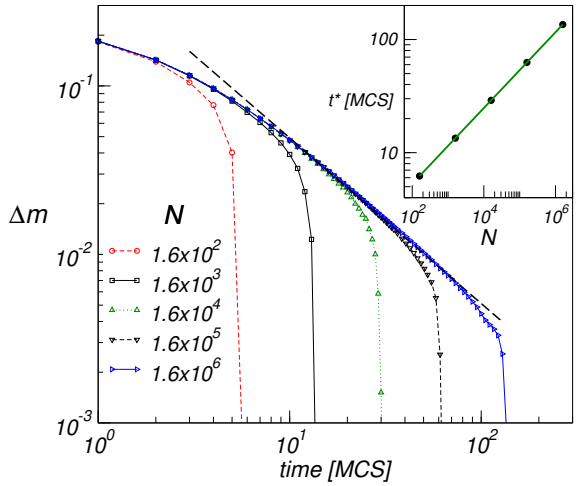


FIGURE 7.3: Short-time behavior of Δm at $h = h_{\rm sp}^{(-)}$ for different system sizes N. Dashed (black) line: power-law fit to $N = 1.6 \times 10^6$ data. Inset: t^*, defined as the time at which Δm reaches 10^{-3}, vs. N.

7.2.2 Spinodal points in the short-range Potts model

We consider the q-state Potts model with nearest-neighbor interactions on the square lattice, with zero-field Hamiltonian (3.12). The 2D Potts model has a second-order transition for $q = 2, 3, 4$ and a first-order transition for $q > 4$. On the square lattice, $T_t(q)/J = 1/\ln(1+\sqrt{q})$ exactly.

For q slightly larger than 4, the transition is very weak. As Binder already noted in 1981 [106], the pseudospinodal temperatures $T_{\rm sp}^{(+)}$ and $T_{\rm sp}^{(-)}$ are extremely close to T_t ($[T_t - T_{\rm sp}^{(-)}]/T_t \lesssim 10^{-3}$ for $q = 5, 6$), making it very difficult to establish whether the pseudospinodals differ from T_t in the thermodynamic limit.

The order parameter is defined as in Eq. (3.14). We performed Monte Carlo simulations with Metropolis dynamics on $N = L \times L$ square lattices (with L between 200 and 4000) and periodic boundary conditions, for $q = 9, 12, 24, 48, 96$, and 192. The runs are quenches from infinite temperature (random initial configuration) to constant T below $T_t(q)$.

Pseudospinodal

For a narrow range of quench temperatures $T < T_t$, the system becomes trapped in a high-energy paramagnetic metastable state, where it remains for a random time, after which it relaxes (relatively quickly) to the ferromagnetic equilibrium state through a nucleation process (see [108] and Section 7.4).

Figure 7.4 shows a typical energy vs. time curve illustrating the nucleation process. The nucleation time has a log-normal distribution [108].

To find the pseudospinodal we search for a divergence in the relaxation time of the metaequilibrium phase. We measure the two-time autocorrelation function:

$$C(t_1, t_2) = \frac{q}{q-1}\left\langle \frac{1}{N}\sum_{i}^{N} \delta\left(\sigma_i(t_1), \sigma_i(t_2)\right) - \frac{1}{q} \right\rangle, \tag{7.5}$$

which depends only on the time difference $t \equiv t_2 - t_1$ in the (meta)stationary regime. We define the relaxation time t_R as the time at which $C(t)$ falls below a threshold $C_{\rm thr}$, and fit $t_R(T)$ with the power-law-plus-correction form [8]:

$$t_R = A\left(\frac{T - T^*}{T_t}\right)^{-b}\left[1 + B\left(\frac{T - T^*}{T_t}\right)^{c}\right]. \tag{7.6}$$

From the fit we consistently obtain $T^* = (0.95 \pm 0.01)T_t$ for $q = 96$, independent of the correction term used.

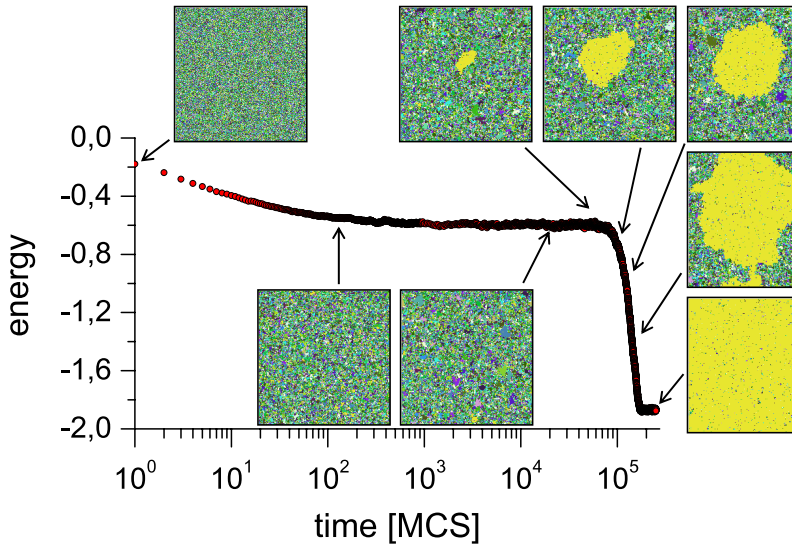


FIGURE 7.4: Energy per spin vs. time for a typical run after a quench from infinite temperature to $T = 0.99\,T_t$ for $q = 24$ and $L = 200$. System images at particular times are shown; colors encode spin states.

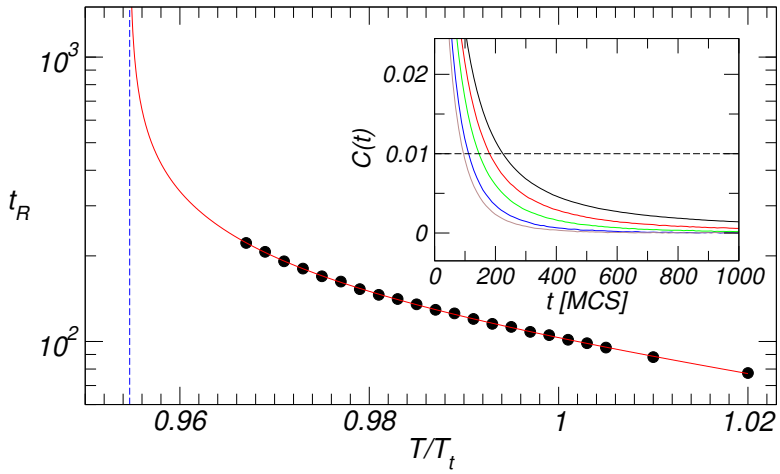


FIGURE 7.5: Relaxation time vs. T/T_t for $L = 1000$ and $q = 96$. The solid line is a fit using Eq. (7.6). Error bars are smaller than the symbol size. Inset: correlation function $C(t)$ for temperatures between $T = 1.005\,T_t$ (left) and $T = 0.967\,T_t$ (right). The vertical dashed line marks $T = T^*$.

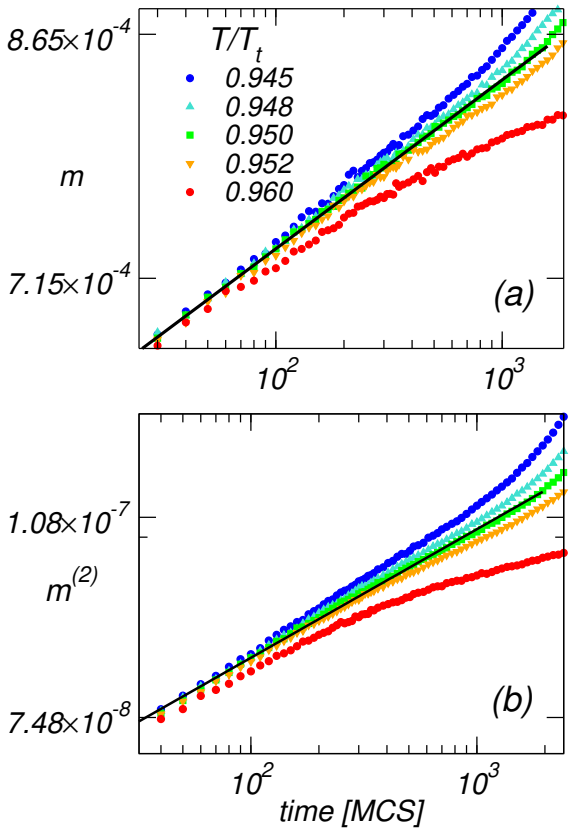


FIGURE 7.6: Short-time dynamics in a supercooled state at different temperatures for $q = 96$ and $L = 480$. Solid lines: power-law fits at $T = 0.950\,T_t$. (a) Order parameter m; (b) second moment $m^{(2)}$.

Spinodal from STD

We now apply the STD method to locate the spinodal point using the order parameter (3.14) and its second moment [95], starting from a completely disordered initial state.

Figure 7.6 shows results for $q = 96$. A clear power-law growth $m \sim t^{\theta}$ and $m^{(2)} \sim t^{\omega}$ is observed at $T = T_{\rm sp}^{(-)} = (0.950 \pm 0.002)T_t$, spanning two decades in time. The exponents found are small ($\theta \approx 0.06$ and $\omega \approx 0.1$).

Unlike the mean-field case, STD results here show no finite-size effects (Fig. 7.7): curves for $L = 480$ and 960 are practically indistinguishable, indicating that the

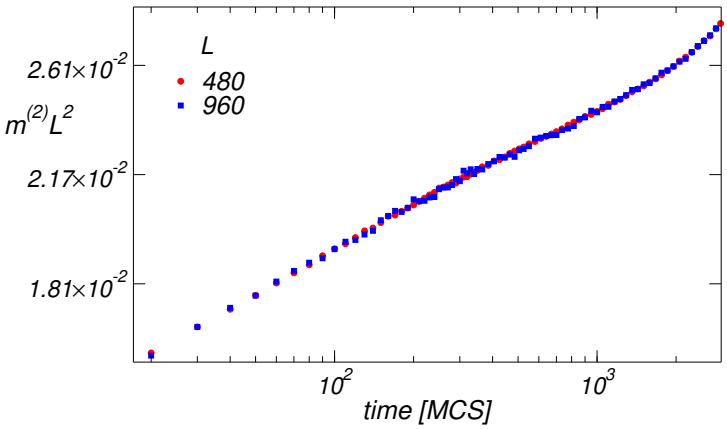


FIGURE 7.7: Short-time behavior of $m^{(2)}$ at $T = 0.95\,T_t$ for different sizes L and $q = 96$ in the Potts model.

spinodal critical regime lasts for a time independent of system size.

The STD-identified spinodal temperature $T_{\rm sp}^{(-)}$ coincides with the pseudospinodal from metaequilibrium measurements. The quasi-instability at $T_{\rm sp}^{(-)}$ is also manifest in the specific heat C_h and magnetic susceptibility χ_T, which grow in a way compatible with a divergence at $T = T_{\rm sp}^{(-)}$ (Figs. 7.8 and 7.9).

Fitting C_h and χ_T in the power-law region $(T - T_{\rm sp}^{(-)})/T_t < 0.15$ yields (pseudo)critical exponents $\alpha = 0.61 \pm 0.04$ and $\gamma = 0.19 \pm 0.04$.

For the upper spinodal, at $T = T_{\rm sp}^{(+)} > T_t$, we start from an ordered initial state. Figure 7.10 shows a clear power-law of the second moment at $T_{\rm sp}^{(+)}/T_t = 1.06 \pm 0.01$ over more than two decades, with exponent $y \approx 0.90$.

Repeating the analysis for $q = 5, 6, 9, 12, 24, 48, 96$, and 192, we find in all cases that the STD spinodal temperature $T_{\rm sp}^{(-)}$ is compatible with the pseudospinodal T^* from metaequilibrium measurements.

Figure 7.11 shows the relaxation time as a function of temperature for different q. The kinetic spinodal is strongly q-dependent, and $T_{\rm sp}^{(-)}$ departs systematically from T_t as q increases.

Figure 7.12 shows that the data can be well fit by:

$$(T_t - T_{\rm sp}^{(-)})/T_t = A \log^a(1 + q - 4)\,, \tag{7.7}$$

with $A = 0.0007$ and $a = 2.81$, in qualitative agreement with the behavior of the Curie–Weiss–Potts model and the Bethe lattice solution with coordination

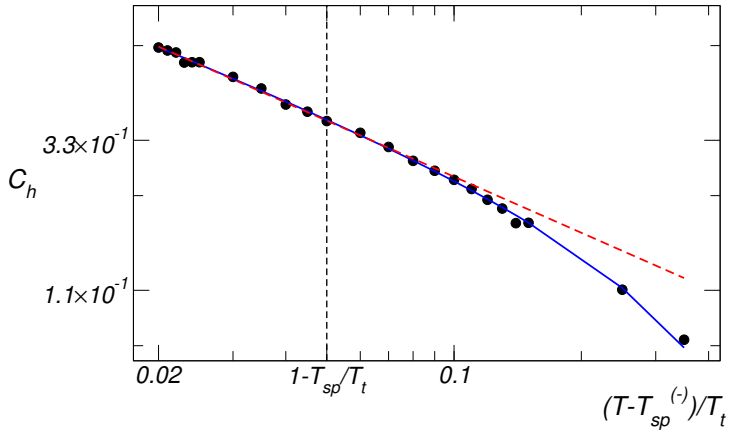


FIGURE 7.8: Specific heat as a function of $T - T_{sp}^{(-)}$ in the metastable state for $q = 96$ and $L = 480$. Solid (blue) line: fit with $A(T - T_{\rm sp}^{(-)})^{\alpha}[1 + B(T - T_{\rm sp}^{(-)})]$. Dashed (red) line: power-law fit for $(T - T_{\rm sp}^{(-)})/T_t < 0.15$. Error bars are smaller than symbol size. Vertical dashed line: $T = T_t$.

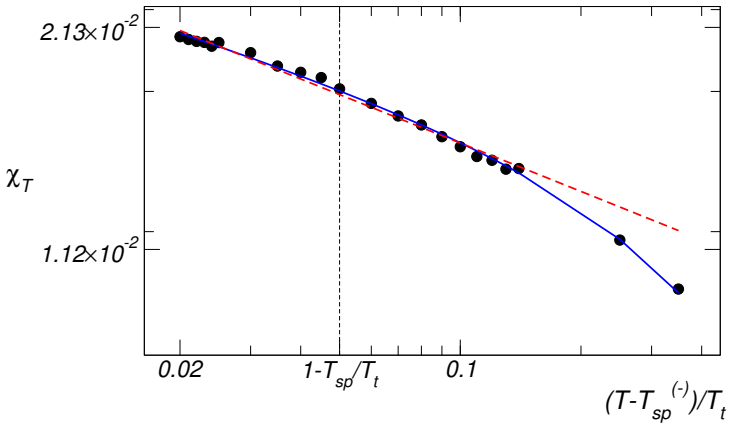


FIGURE 7.9: Magnetic susceptibility as a function of $T - T_{sp}^{(-)}$ in the metastable state for $q = 96$ and $L = 480$. Same fitting conventions as Fig. 7.8.

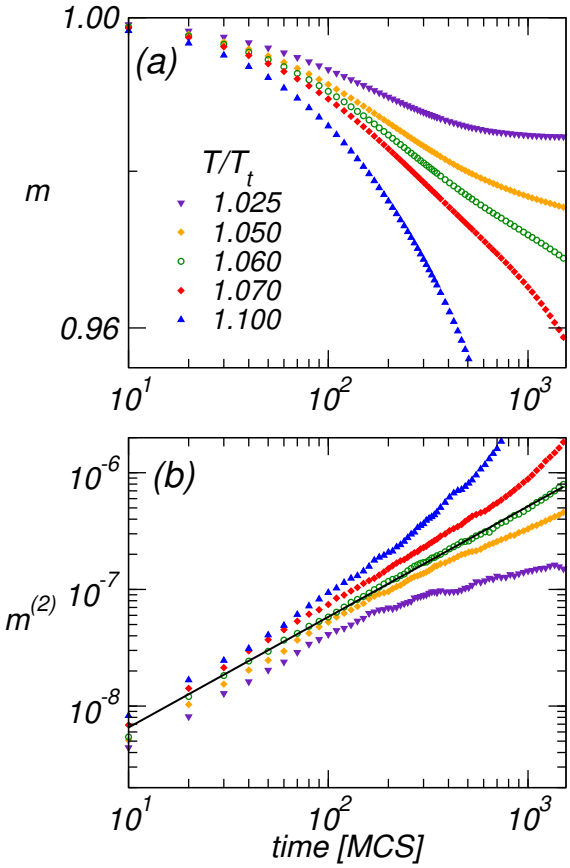


FIGURE 7.10: Short-time dynamics in a superheated state at different temperatures for $q = 96$ and $L = 480$. Solid line in (b): power-law fit at $T = 1.06\,T_t$. (a) Order parameter m; (b) second moment $m^{(2)}$.

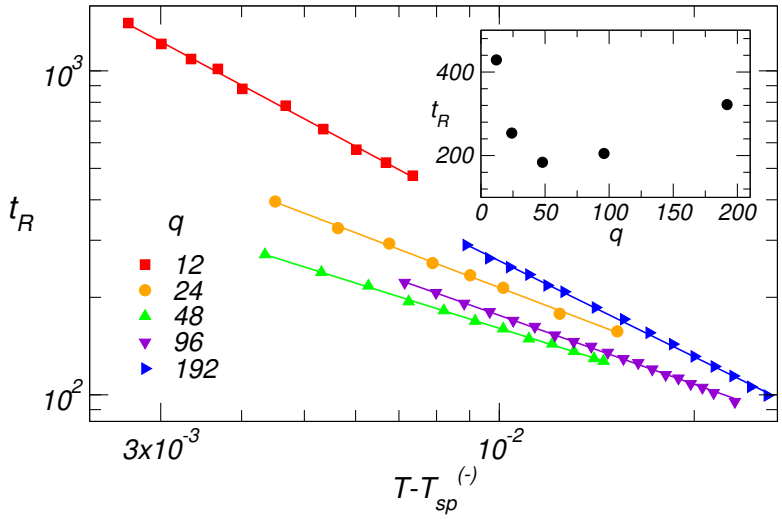


FIGURE 7.11: Relaxation time as a function of $T - T_{\rm sp}^{(-)}$ for $L = 1000$ and various q. Error bars are smaller than symbol size. Solid lines: power-law fits. Inset: t_R as a function of q at fixed $T - T_{sp} = 0.008$.

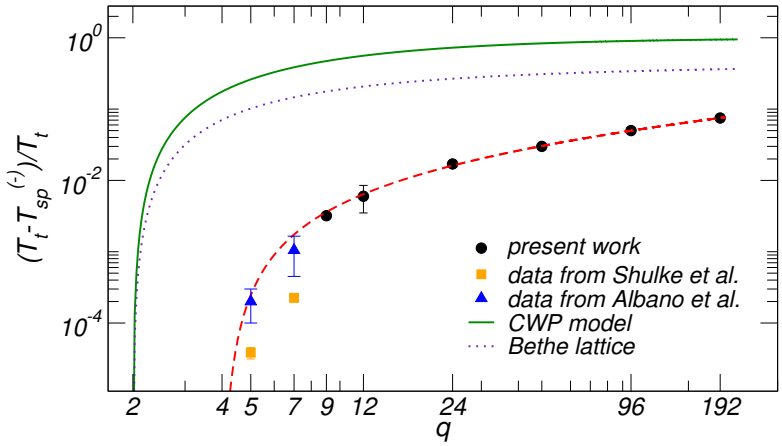


FIGURE 7.12: $(T_t - T_{\rm sp}^{(-)})/T_t$ vs. q compared to mean-field predictions. Data for $q = 5, 7$ are taken from [109] and [96]. The dashed red line is a fit to our data with the form $A \log^a(1 + q - 4)$, yielding $A = 0.0007$ and $a = 2.81$.

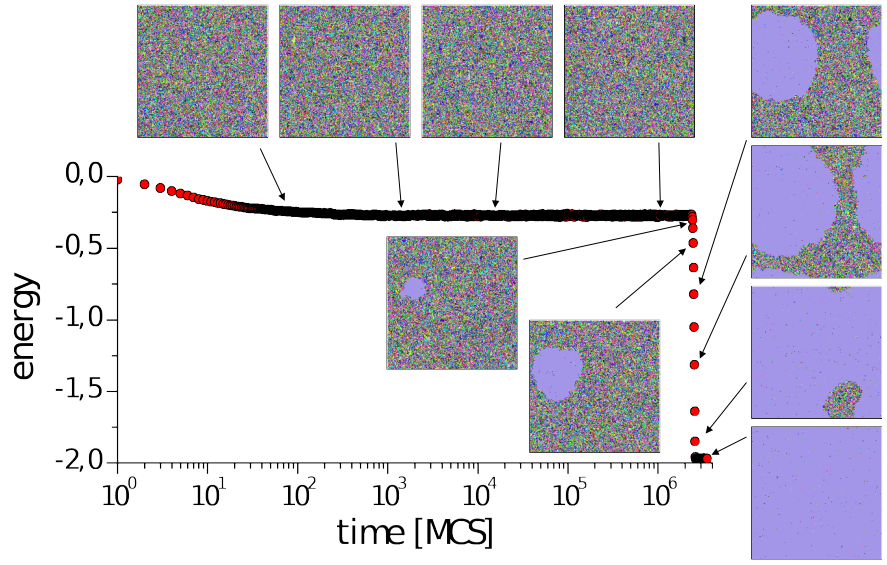


FIGURE 7.13: Energy per spin vs. time for a typical run after a quench from infinite temperature to $T = 0.975\,T_t$ for $q = 96$ and $L = 200$. System images at particular times are shown; colors encode spin states. Note the clearly visible appearance of the critical nucleus when the system escapes from the metastable state and relaxes to equilibrium.

number $z = 3$, as expected in the large-q limit where the mean-field solution becomes exact [110].

7.3 Metastability in the Potts model

Metastability in the temperature-driven transition of the 2D Potts model is well established in finite systems [4, 51, 107]: below but close to T_t the system quickly relaxes to a disordered (paramagnetic) metastable state with a finite lifetime that diverges as the quench temperature T approaches T_t [108].

In Fig. 7.4 for $q = 24$ and $T = 0.99\,T_t$, the metastability plateau extends over about three decades (10^2 to 10^5 MCS). For $q = 96$ and $T = 0.975\,T_t$ (Fig. 7.13), the plateau extends over an additional order of magnitude ($\sim 10^6$ MCS), consistent with the fact that for $q \to \infty$ (where the mean-field treatment becomes exact) the metastable lifetime is infinite.

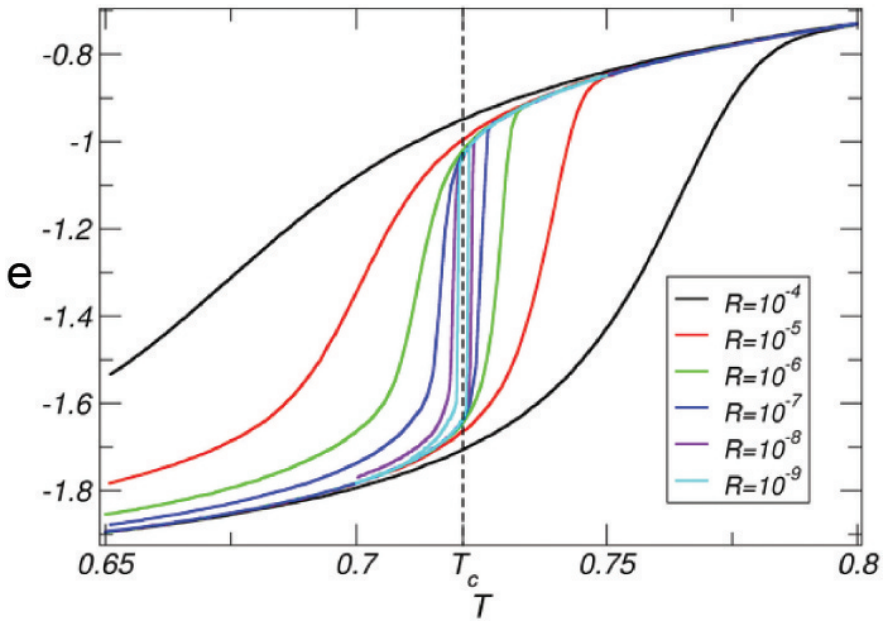


FIGURE 7.14: Energy per spin vs. temperature for various sweep rates R for $q = 9$ in a $N = 2048^2$ system. Curves were obtained with the GPU algorithm.

7.3.1 Hysteresis

Figure 7.14 shows hysteresis cycles with temperature for $q = 9$ in an $N = 2048^2$ system ($T_t(q = 9) = 0.72134\ldots$). The hysteresis loop area decreases as R decreases (slower sweep), but even for rates as small as $R = 10^{-9}$ and sizes as large as $N = 2048^2$, the area remains finite. This constitutes strong evidence of the presence of metastable states, in a narrow temperature window around T_t consistent with our STD estimate of the spinodal distance $(T_t - T_{\rm sp}^{(-)})/T_t \approx 0.0035$ for $q = 9$.

7.3.2 The Binder criterion and the two possible scenarios

In Ref. [106] Binder studied the static and dynamic behavior of model (3.12) for $q = 3, 4, 5, 6$. His analysis could not distinguish between two possible scenarios for the transition at $q \geq 5$ due to finite-size effects, illustrated in Fig. 7.15. In scenario A, the energy per spin reaches the transition temperature with a finite slope from both sides, projecting metastable branches to both sides of the transi-

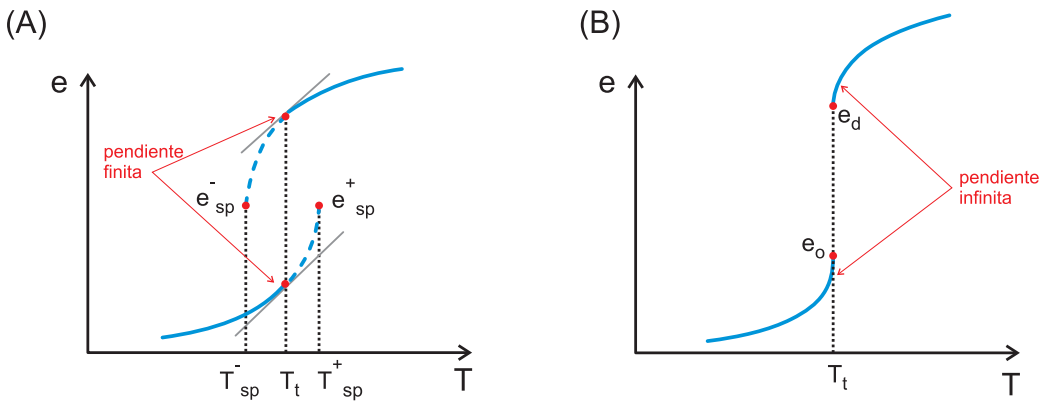


FIGURE 7.15: Schematic of the energy vs. temperature behavior for the case of pseudo-spinodal singularities (A) and for a true divergence of the specific heat at the first-order transition (B). (Adapted from [106]).

tion that end at temperatures T_{sp}^{+} and T_{sp}^{-} both distinct from T_t. In scenario B, the energy approaches T_t with an infinite slope, implying a true divergence at T_t.

7.3.3 Response to Binder's question about the existence of metastability

Based on the Binder criterion, we analyze the existence of metastability for $q > 4$ as we increase system size, using the GPU algorithm of Appendix C.

We compute the energy per spin above and below the transition, cooling (heating) from a disordered (ordered) initial state. Figure 7.16 shows equilibrium energy and magnetization for different q; for sufficiently large q the energy branches reach the transition temperature from both sides with a finite slope.

A power-law divergence of the specific heat at T_t would imply:

$$e_{T<T_t} = e_o - A^{-}(1 - T/T_t)^{1-\alpha_-}, \tag{7.8}$$

$$e_{T>T_t} = e_d - A^{+}(1 - T_t/T)^{1-\alpha_+}, \tag{7.9}$$

with $0 < \alpha_-, \alpha_+ < 1$. If instead metastable states exist with spinodals $T_{sp}^{\pm}$ distinct from T_t, the energy would show a crossover to slope ≈ 1 ($\alpha_\pm \approx 0$) as one approaches T_t — and this crossover should persist as L increases.

Figures 7.17 and 7.18 show the equilibrium energy curves above and below T_t. In both figures a crossover in the slope is observed as one approaches T_t for all values of q.

Sufficiently close to T_t, the curves for $q = 9, 15, 96$ show exponents $(1 - \alpha_\pm)$ indistinguishable from 1 ($\alpha_\pm = 0$), persistently as L grows (see inset of Fig. 7.17).

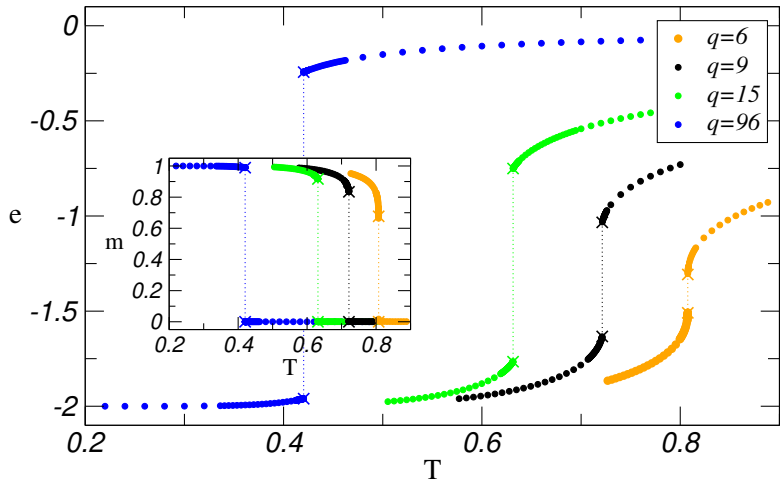


FIGURE 7.16: Energy per spin e and magnetization m (inset) as a function of temperature, for $q = 9, 12, 15, 96$. Crosses indicate exact values at the transition temperature from Eqs. (3.16), (3.19), and (3.20). Data are averages over 10 samples of linear size $L = 2048$.

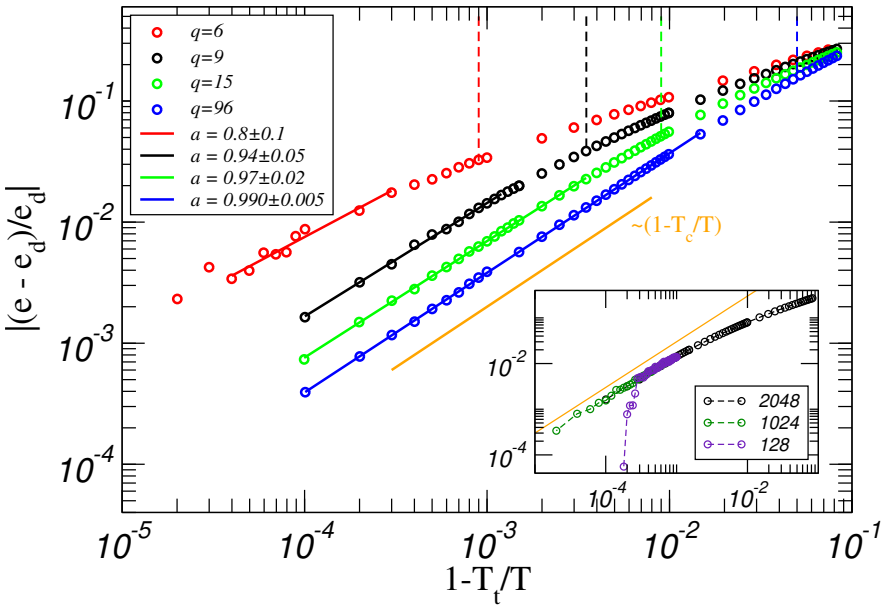


FIGURE 7.17: Log-log plot of $|(e - e_d)/e_d|$ vs. $(1 - T_t/T)$ for various q. Data: averages over 20 samples of $L = 2048$. Solid colored lines: power-law fits. Vertical dashed lines: $T = T_t + \Delta T(q)$ with $\Delta T = T_t - T_{sp}^-$ from Eq. (7.7). Inset: curves for $q = 9$ at different system sizes; solid orange line shows slope 1.

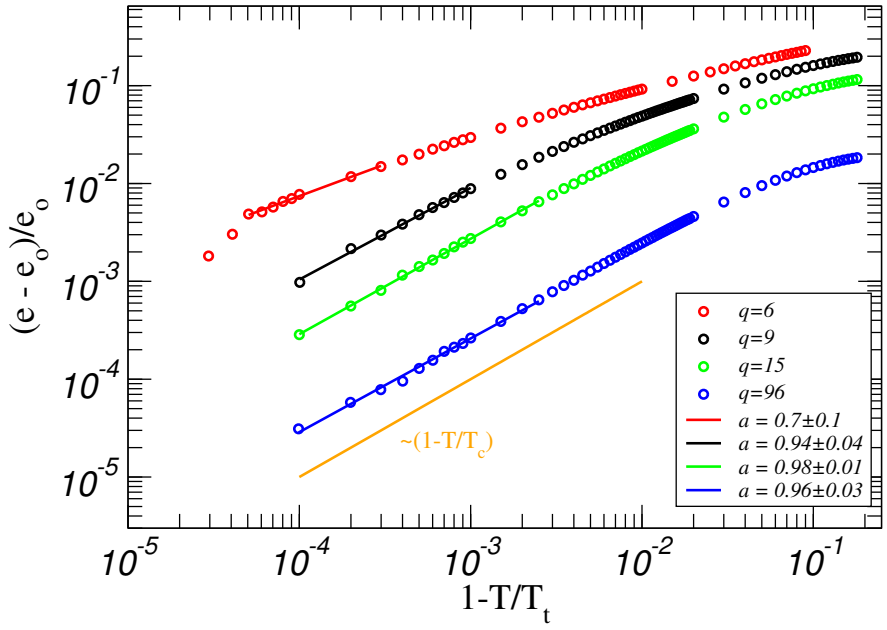


FIGURE 7.18: Log-log plot of $(e-e_o)/e_o$ vs. $(1-T/T_t)$ for various q. Data: averages over 20 samples of $L = 2048$. Solid colored lines: power-law fits $(e-e_o)/e_o = A(1-T/T_t)^a$.

This is consistent with divergences at spinodal temperatures distinct from T_t, at least for $q \geq 9$, and constitutes strong evidence for the existence of metastability.

The crossover occurs at temperatures consistent with our STD estimates: the vertical dashed lines in Fig. 7.17 correspond to $T = T_t + \Delta T(q)$ predicted by Eq. (7.7), in close agreement with the observed crossover points for all q.

Our results for $q = 6$ are not conclusive; statistical fluctuations at the required temperature resolution ($\Delta T/T_t \leq 10^{-4}$) are too large for a definitive determination. Larger systems and/or more samples would be needed. We cannot exclude the existence of a critical value $4 < q^* \leq 9$ below which metastability disappears.

7.4 Relaxation from the metastable state: nucleation

As discussed in [108] and illustrated in Figs. 7.4 and 7.13, the mechanism by which the system relaxes from the metastable state to equilibrium is *nucleation* (Section 4.1.4).

Figure 7.19 shows spatial correlations for $q = 24$ and $L = 200$ at various times during the relaxation after a quench to $T = 0.987\,T_t$. Just before nucle-

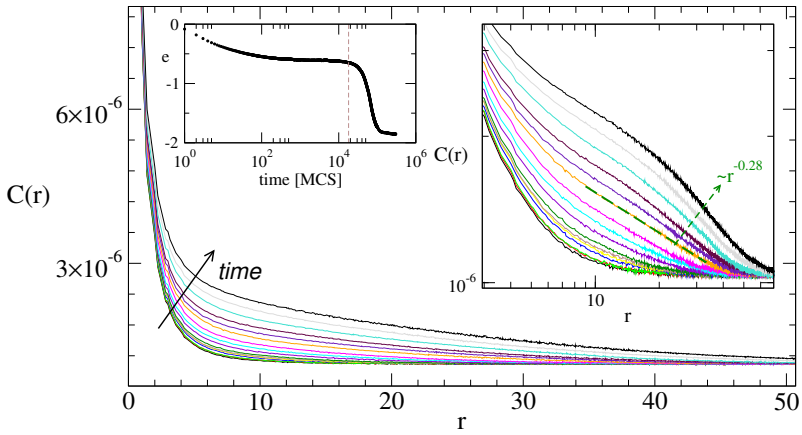


FIGURE 7.19: Spatial correlations as a function of distance for $L = 200$, $q = 24$, taken during relaxation after a quench to $T = 0.987\,T_t$. Curves correspond to different times between $t = 1000$ and $t = 30000$. Right inset: same curves on a log-log scale; dashed green line: power-law fit at $t_0 = 18000$. Left inset: energy relaxation vs. time; vertical dashed line at $t_0 = 18000$. Averages over 20 samples.

ation occurs, at time $t_0 = 18000$ MCS (left inset shows the energy drop at this time), the spatial correlations already display a power-law decay over more than a decade in distance (right inset). This suggests that spatial correlations begin to grow *before* the critical nucleus appears, constituting a strong "precursor effect" for nucleation.

To test this hypothesis more directly we performed simulations starting from a nearly disordered initial configuration in which a single ferromagnetic droplet of radius R_0 has been artificially planted.

According to Classical Nucleation Theory, the droplet should either shrink and dissolve (if $R_0 < R_c$) or grow immediately and fill the system (if $R_0 > R_c$). Contrary to this expectation, for intermediate R_0 we observe that the droplet neither vanishes immediately nor grows at once; instead, it persists for a time comparable to the nucleation time from a random initial state before eventually growing. Figure 7.20 illustrates this for $R_0 = 9$, $q = 96$, and $L = 200$, showing the bimodal distribution of relaxation times.

We define a crossover radius R^* such that droplets with $R_0 < R^*$ follow case (a) (the droplet disappears) and those with $R_0 > R^*$ follow case (b) (the droplet eventually grows). For $q = 96$, $L = 100$ and 200, we find the crossover region $7 \leq R^* \leq 10$.

These results suggest that what triggers relaxation from the metastable state is not simply the presence of a supercritical droplet, but rather the development

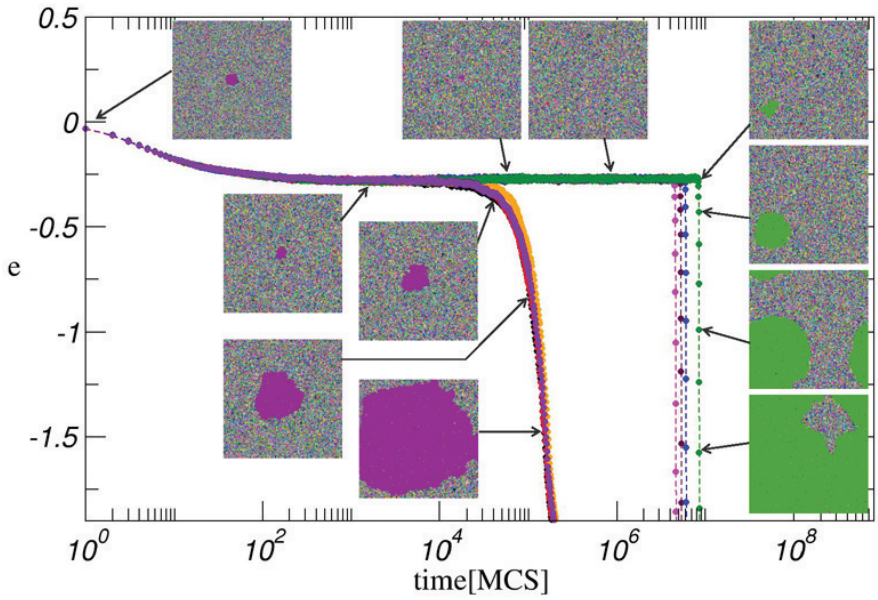


FIGURE 7.20: Relaxation for $q = 96$, $L = 200$ at $T = 0.975\,T_t$ from a disordered initial state with an ordered droplet of radius $R_0 = 9$. Different curves correspond to different thermal noise realizations; snapshots at various times are shown with spin states encoded by color.

of spatial correlations in the system reaching a level at which the growth of an ordered droplet becomes favorable. A systematic study of this phenomenon's dependence on q, T, and L remains to be done.

7.5 Chapter conclusions

- We demonstrated that STD provides a meaningful and practically useful definition of spinodal points for both mean-field and short-range systems, identifying the temperature at which the system exhibits critical-like short-time dynamical behavior.
- The spinodal temperatures $T_{SP}^{(\pm)}$ are distinct from T_t for all $q > 4$, delimiting a genuine metastability interval that survives in the thermodynamic limit.
- GPU-accelerated Monte Carlo simulations provide direct numerical evidence for the persistence of metastability in the thermodynamic limit, resolving a long-standing controversy in the literature.
- The relaxation from the metastable state proceeds via nucleation, with preliminary evidence for a collective precursor mechanism: spatial correlations grow before the critical nucleus appears, pointing toward a self-organized nucleation process rather than the purely random single-droplet picture of standard Classical Nucleation Theory.

The STD approach to spinodals has practical advantages beyond conceptual clarity: it avoids equilibration difficulties and may be applicable to systems with very slow dynamics (such as glass-forming liquids) where metaequilibrium measurements are out of reach. Our definition does not imply a thermodynamic singularity at the spinodal — it is fundamentally a dynamical definition.

CHAPTER 8

RELAXATION AT LOW TEMPERATURES IN THE TWO-DIMENSIONAL q-STATE POTTS MODEL

We now study the non-equilibrium dynamics of the q-state Potts model on the square lattice, after a quench to temperatures below the transition temperature. Using a Continuous-Time Monte Carlo algorithm, we analyze the long-time behavior of the energy and the relaxation time over a wide range of quench temperatures and system sizes. For $q > 4$ we find the existence of distinct dynamical regimes depending on the quench temperature range. At low (but finite) temperatures and very long times, Lifshitz–Allen–Cahn-type domain growth is interrupted with finite probability when the system becomes trapped in highly symmetric non-equilibrium metastable states[1] that induce thermally activated domain growth, in agreement with an old prediction of Lifshitz [77]. At even lower temperatures, the system always becomes trapped at early times in highly disordered metastable states with a finite lifetime, which have been identified as glassy states. We analyze in detail the finite-size scaling properties of the various relaxation times involved, as well as their temperature dependence.

This chapter is based primarily on [4]. Toward the end, a result related to the very-low-temperature state is part of a work in collaboration with Mr. Miguel Ibáñez de Berganza and Drs. Vittorio Loreto and Alberto Petri (Università di Roma, Italy) [Ibáñez de Berganza et al., *Eur. Phys. J. Special Topics* **143**, 273 (2007)].

8.1 Introduction

The problem of domain-growth kinetics in systems with degenerate ground states has attracted much attention [47,48,77,111–115]. In the early works on the subject, Lifshitz [77] and later Safran [111] opened the discussion about the effects of activated processes in domain growth. They suggested that d-dimensional systems with q-fold ground-state degeneracy could become trapped in local metastable states for $q \geq d + 1$, which would appreciably slow the relaxation kinetics. Their argument (in two dimensions) is that a honeycomb domain structure is stable against small interface distortions since such distortions do not increase the interfacial free energy. Large distortions produced by fluctuations are therefore needed to move the interfaces, making domain growth an activated process. The prototype of a system with these characteristics is precisely the q-state Potts model (in the absence of an external field) with Hamiltonian (3.12).

Sahni et al. [112, 113] performed Monte Carlo simulations with Glauber dynamics for q up to 64 on square and triangular lattices of up to $N = 200^2$ sites and timescales of order 10^4 MCS. On the square lattice they found evidence of

[1] in the purely kinetic sense, see Section 2.3.2

metastable configurations composed of squares of different colors (i.e., different spin values) that freeze the dynamics at $T = 0$.

Viñals and Grant [47] obtained similar results on the square lattice and postulated that frozen configurations only dominated effectively at $T = 0$, and that growth at finite temperatures was not limited by activated processes. For sufficiently long times, the characteristic domain size should therefore follow the Lifshitz–Allen–Cahn (LAC) law $\ell(t) \sim t^{1/2}$.

This appears to be the case for the triangular lattice, for which Grest et al. [48] reported MC results with $N = 1000^2$ sites up to 10^4 MCS, consistent with LAC behavior for any q. However, the timescales considered in those works are too short to exclude activated processes of the type predicted by Lifshitz [77] and Safran [111].

More recent work [116–118] on the frozen configurations found on the square lattice showed that the system becomes trapped in those states at timescales larger than 10^4 MCS. Trapping also occurs at low but finite temperatures [119], but in that case the metastable states have a finite lifetime that increases with q. Those works also show that the nature of the highly disordered metastable states is more akin to a glassy state [116–119] than to the configurations predicted by Lifshitz and Safran. We will refer to these as glassy states throughout.

We focus primarily on the case $q = 9$ (on the square lattice with $N = L \times L$ sites and periodic boundary conditions). Some complementary results are presented for other values of q. The implementation of a Continuous-Time ("n-fold way") Monte Carlo algorithm [120, 121] allowed us to analyze systems up to $L = 500$ and timescales of 10^9 to 10^{14} MCS with good statistics (see Appendix B).

The main results of this chapter can be summarized as follows: after a quench from infinite temperature to $T < T_t$, we identify different dynamical relaxation regimes depending on the quench temperature range.

There is a characteristic temperature $T^\dagger < T_t$ such that for $T^\dagger < T < T_t$ simple coarsening dominates the relaxation (following the LAC law even at long times), except very close to T_c where nucleation effects appear (as discussed in the previous chapter).

For $T < T^\dagger$ we find that, at large timescales (much larger than those considered in previous works), LAC relaxation is interrupted when the system becomes trapped in highly symmetric metastable blocked states with finite probability; i.e., for a significant fraction of thermal-noise realizations that does not decrease as system size increases.

We find two distinct types of blocked states: *stripe states*, composed of two macroscopic ferromagnetic domains separated by flat walls parallel to the coordinate axes; and *honeycomb-like* (Lifshitz) structures, composed of irregular hexag-

onal polygons of different colors. Stripe states have been previously observed in the Ising model ($q = 2$) at $T = 0$ [86, 122–125]. For $q \geq 3$ at $T = 0$ the probability of reaching a stripe state vanishes in the thermodynamic limit [86]; at low but finite temperatures it becomes finite.

We also study the inhomogeneous LAC growth at $T = 0$ and its behavior at low finite temperatures, as observed in [119] for $q = 7$.

8.2 Relaxation in the Potts model

We study the evolution under model-A dynamics (non-conserved order parameter) of the system described by Hamiltonian (3.12), after a quench from infinite temperature (completely random initial configuration) to temperatures below the critical temperature. Most analyses concentrate on $q = 9$, for which $T_t = 0.721347\ldots$ from Eq. (3.15). Complementary calculations were performed for $q = 2, 3, 4, 5, 15, 20, 30$, and 48.

We focus primarily on two quantities: the average energy per spin $e(t) \equiv \langle H(t)\rangle/N$ as a function of t, and the equilibration time τ, defined as the time at which the instantaneous energy falls below a threshold chosen as the equilibrium energy plus one standard deviation.

For comparison at different temperatures we introduce the normalized energy relaxation function (or normalized excess energy):

$$\phi_E(t) \equiv \frac{e(t) - e(\infty)}{e(0) - e(\infty)} \tag{8.1}$$

where $e(\infty)$ is the equilibrium energy.

Figure 8.1 shows the typical behavior of $\phi_E(t)$ for $L = 300$ and temperatures between 0.72 and 0.5 ($T_t = 0.721347\ldots$). For temperatures sufficiently close to T_t ($0.715 < T < T_t$) the system clearly halts in a high-energy metastable state (disordered paramagnetic), related to the first-order nature of the transition, which according to our numerical evidence persists in the thermodynamic limit. In the non-equilibrium dynamics, this metastable state manifests as a plateau in the energy vs. time curves, lasting for a period that can span several decades depending on T and q, after which the system relaxes via nucleation.

For temperatures $T < 0.715$, the metastability plateau disappears and the relaxation function decays (after a short transient) as $\phi_E(t) \sim t^{-1/2}$ for all temperatures. Since the excess energy relative to equilibrium in a domain-growth process is given by the average energy of domain walls, $\phi_E(t) \sim 1/\ell(t)$, so this behavior is consistent with the Lifshitz–Allen–Cahn law (Eq. 4.6 with $n = 1/2$).

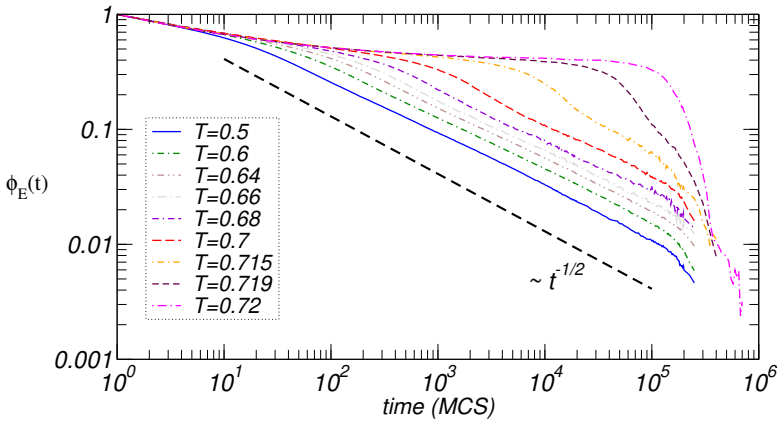


FIGURE 8.1: Relaxation function $\phi_E(t)$ for $L = 300$, $q = 9$, and temperatures between $T = 0.5$ (bottom) and $T = 0.72$ (top).

8.2.1 Relaxation at intermediate temperatures and blocked states: characterization and scaling

Figure 8.2 shows the typical behavior of $P(\tau)$ for $L = 100$ and different temperature ranges, already showing the distinct dynamical regimes:

Sufficiently close to T_t ($T = 0.719$), $P(\tau)$ exhibits a well-defined peak centered at $\tau_{nucl} \sim 10^5$ MCS, associated with the nucleation relaxation mechanism.

When the temperature drops below a characteristic temperature[2] T_n with $0.715 < T_n < T_t$, this peak is suddenly replaced by another centered at a characteristic value τ_1, about an order of magnitude smaller than τ_{nucl}, which remains nearly temperature-independent over $0.3 < T < 0.715$. Below T_n, $P(\tau)$ develops a long tail to the right; this tail becomes a distinct second peak centered at a new characteristic time τ_2, for temperatures $T < T^{\dagger} \approx 0.6$. This second peak grows exponentially as the temperature decreases.

Figure 8.3 summarizes the temperature behavior of τ_1 and τ_2 on a log-vs.-$1/T$ (Arrhenius) plot. We show that τ_1 is associated with simple coarsening following the LAC law at all times, while τ_2 is associated with processes in which the system becomes trapped in stripe metastable states (Fig. 8.4).

At finite temperature, domain walls in stripe states undergo random motion perpendicular to the walls. In a finite system, these states relax to equilibrium when both walls collapse. Spirin et al. [123] showed that the basic mechanism

[2] T_n represents the metastability limit (kinetic spinodal); it is bounded by $T_{sp}^{(-)}$ but not necessarily equal to it.

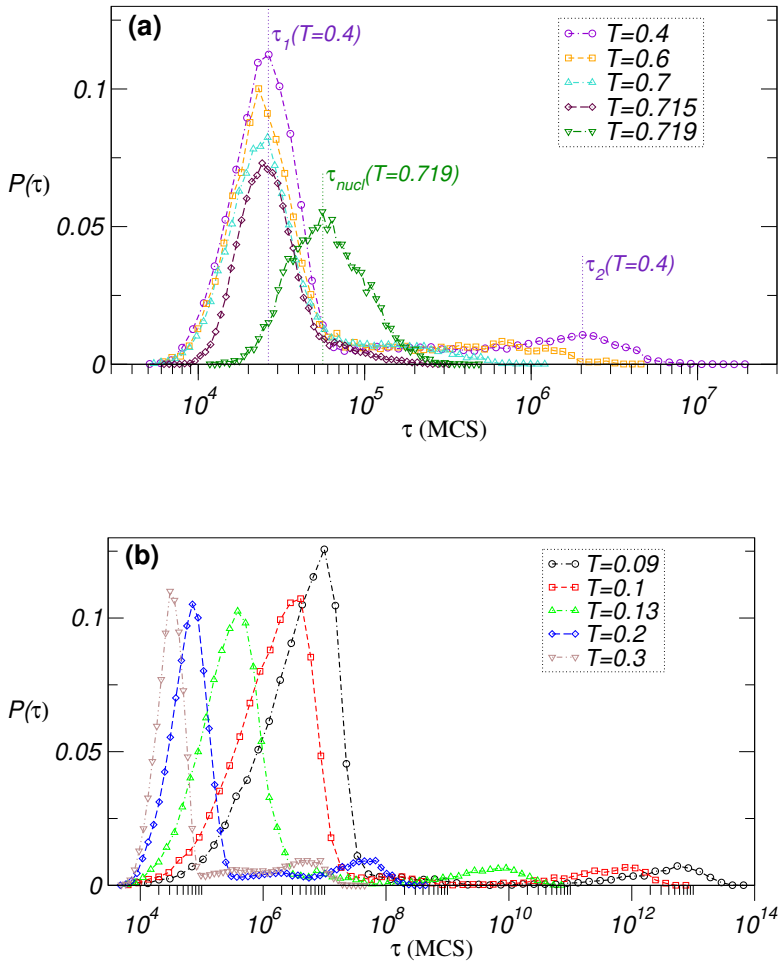


FIGURE 8.2: Probability distribution of the equilibration time $P(\tau)$ for $L = 100$ and $q = 9$. (a) Temperatures from $T = 0.4$ (top) to $T = 0.719$ (bottom); (b) temperatures from $T = 0.3$ (left) to $T = 0.09$ (right).

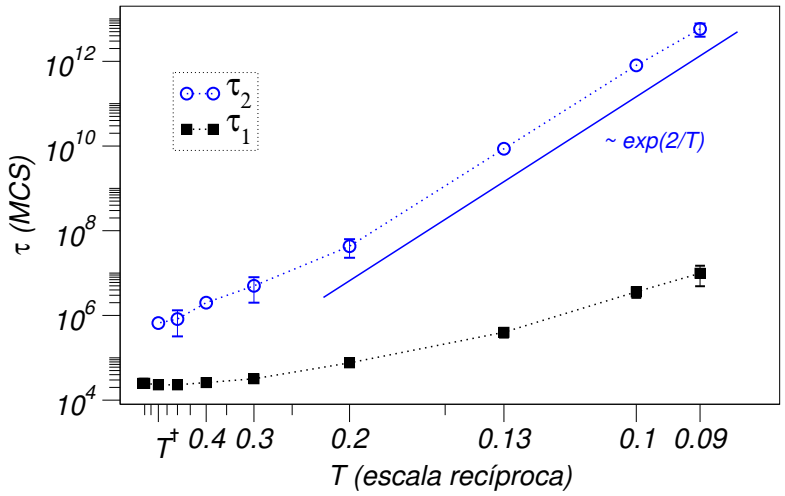


FIGURE 8.3: Characteristic relaxation times τ_1 and τ_2 vs. $1/T$ for $L = 100$ and $q = 9$; the same qualitative behaviors are observed for other system sizes. Solid lines are guides to the eye.

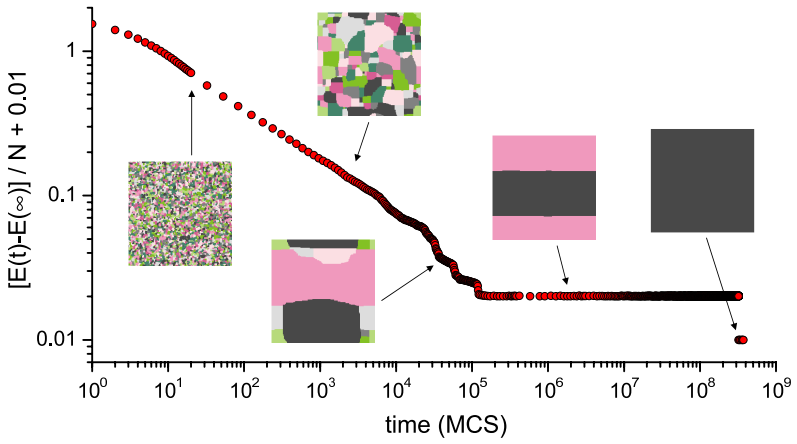


FIGURE 8.4: Energy per spin vs. time and typical configurations in a single stochastic realization when the system becomes trapped in a stripe configuration ($L = 200$, $q = 9$, and $T = 0.2$). Different colors encode different spin values $s_i = 1, \ldots, 9$.

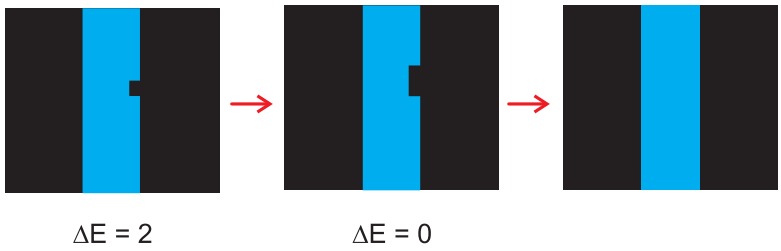


FIGURE 8.5: Relaxation of a stripe state at low but finite temperature. (left) nucleation of a tooth, energy cost $\Delta E = 2$; (center) diffusive growth of the tooth at zero energy cost; (right) the tooth spans the system, the wall advances one step. Adapted from [86].

for parallel motion of a flat domain wall is the creation of a "tooth" (the flip of a neighboring spin), with an energy cost of $2J$ (4 in Ising convention). For $q > 2$, any other flip (including to a third color) costs more energy. Once the stripe state is reached, the relaxation time is therefore basically independent of q, consistent with the Arrhenius behavior $\tau_2 \sim e^{2/T}$ in Fig. 8.3.

From Fig. 8.3 we also note that over a wide temperature range $T < T_n$ (roughly down to $T \approx 0.2$), τ_1 remains practically temperature-independent, consistent with ordinary coarsening. At lower temperatures a crossover to activated behavior appears, analyzed below.

Figure 8.6 shows $P(\tau)$ for different system sizes at $T = 0.2$. The double-peak structure survives in the large-L limit, with the ratio of areas under the two peaks becoming constant.

From Fig. 8.7 we see that $\tau_1 \sim L^2$ over a wide range of temperatures and sizes, consistent with the LAC law. As temperature decreases, the L^2 scaling breaks down due to the onset of activated processes.

The scaling of τ_2 with L is $\tau_2 \sim L^\omega e^{2/T}$ (consistent with the Spirin et al. analysis for stripe states), with ω varying between 2 and 4 depending on temperature, making τ_2 many orders of magnitude larger than τ_1 for large systems.

Careful inspection of individual processes in $P(\tau)$ shows that the broad right peak is associated with two different types of metastable configurations: the stripe states (already described) and honeycomb-like structures (the inset of Fig. 8.10). The latter are composed of macroscopic polygonal domains of different colors with six irregular sides, with angles at triple junctions fluctuating around $120°$. These states agree with a prediction of Lifshitz [77] for $q \geq 3$; we call them *Lifshitz states*.

By computing the equilibration time distribution starting directly from Lifshitz and stripe configurations, we verify (Fig. 8.10) that the broad peak is indeed

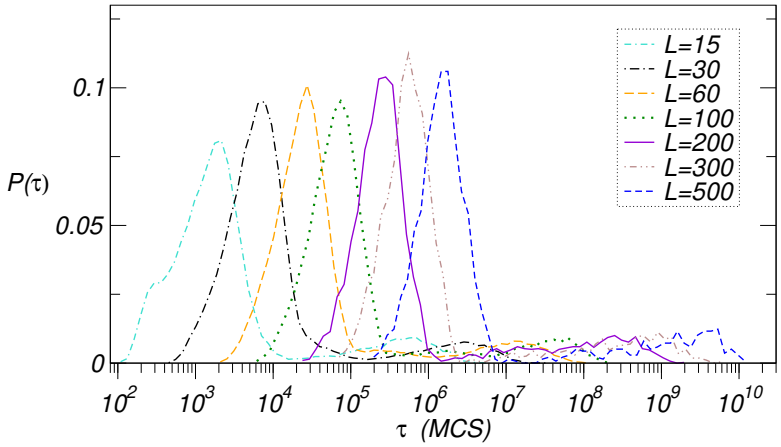


FIGURE 8.6: Probability distribution $P(\tau)$ for $T = 0.2$, $q = 9$, and system sizes from $L = 15$ (left) to $L = 500$ (right).

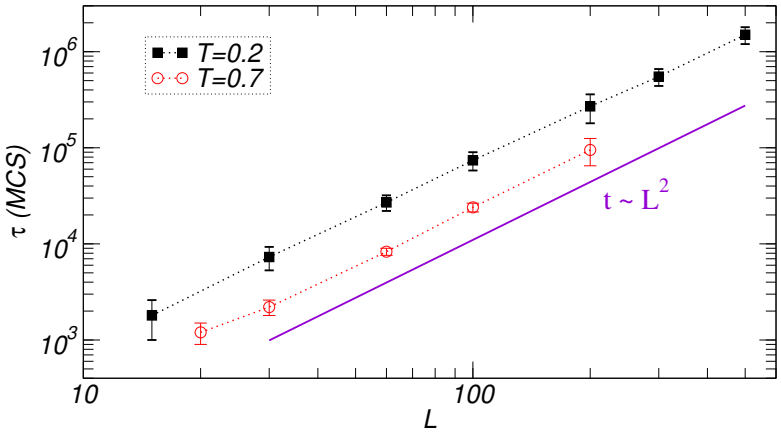


FIGURE 8.7: Characteristic relaxation time τ_1 vs. L for $q = 9$ and various temperatures. Dotted lines are guides to the eye.

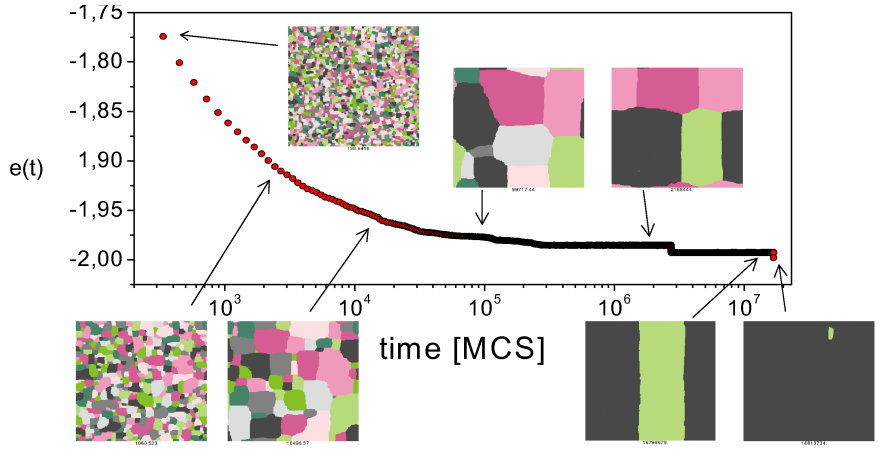


FIGURE 8.8: Energy per spin vs. time and typical configurations in a single realization where the system is trapped in a Lifshitz state and, upon escaping, becomes trapped again in a stripe state ($L = 300$, $q = 9$, $T = 0.3$). Different colors encode different spin values.

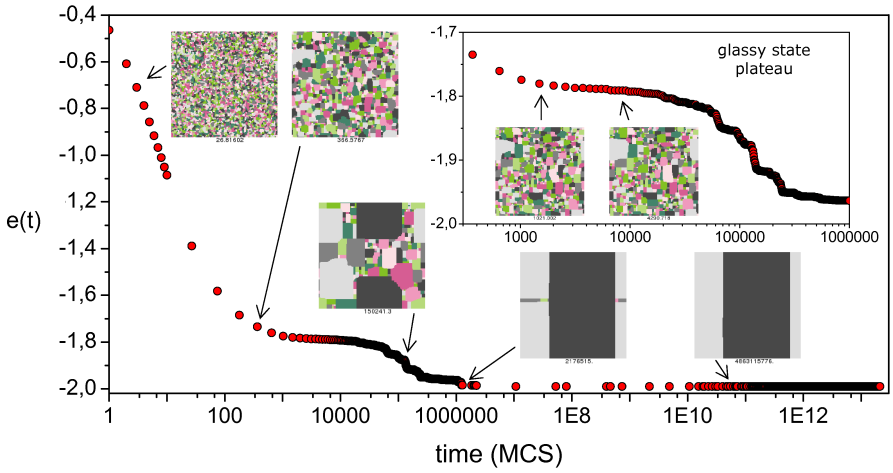


FIGURE 8.9: Energy per spin vs. time and typical configurations in a single realization when the system is trapped in the glassy state and, upon escaping, becomes trapped in a stripe state ($L = 200$, $q = 9$, $T = 0.09$). The inset shows a zoom of the glassy plateau.

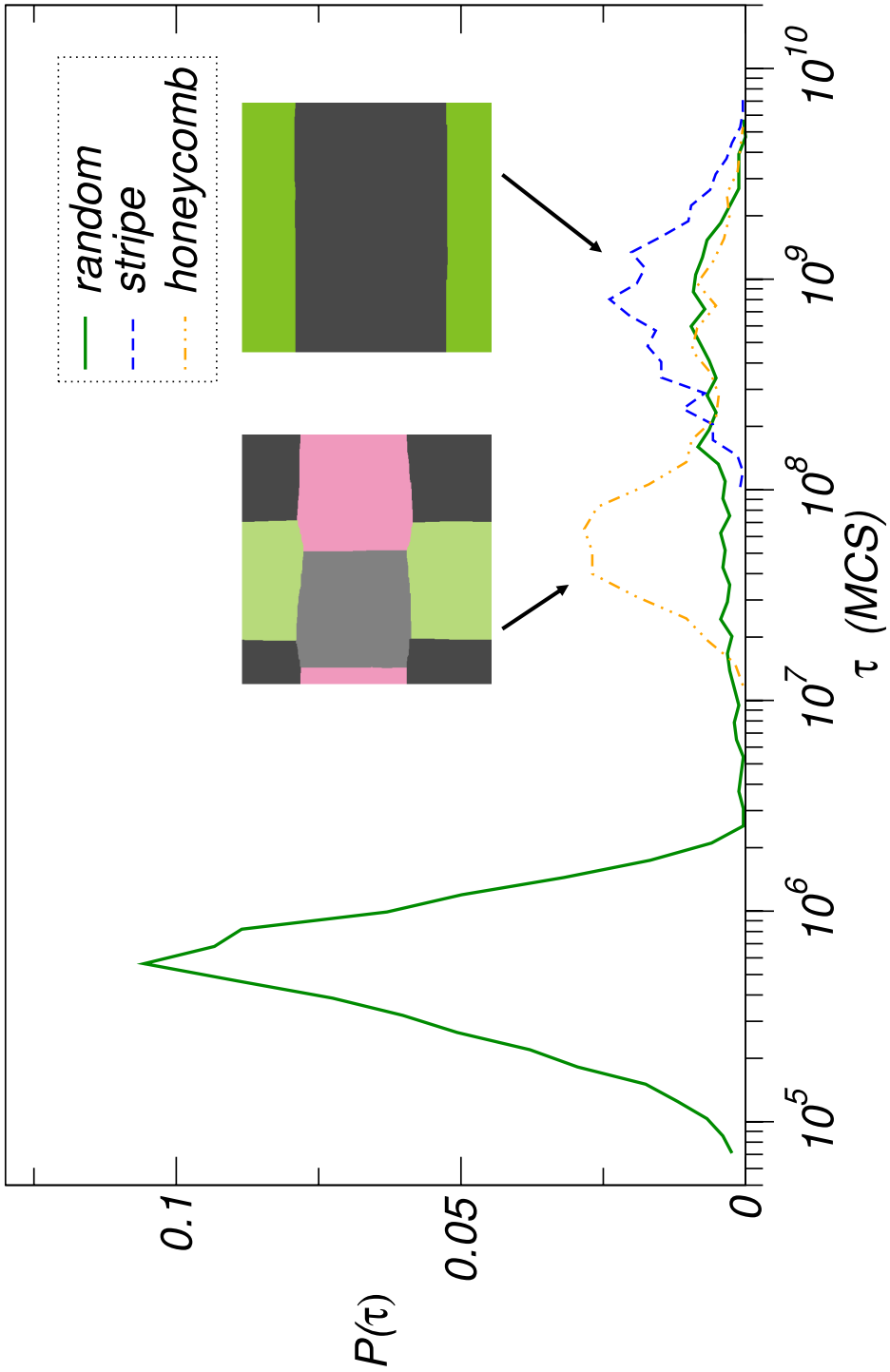


FIGURE 8.10: Probability distribution $P(\tau)$ starting from different initial configurations, for $L = 300$, $T = 0.2$, $q = 9$ (arbitrary normalization). Inset: typical blocked-state snapshots at the corresponding times.

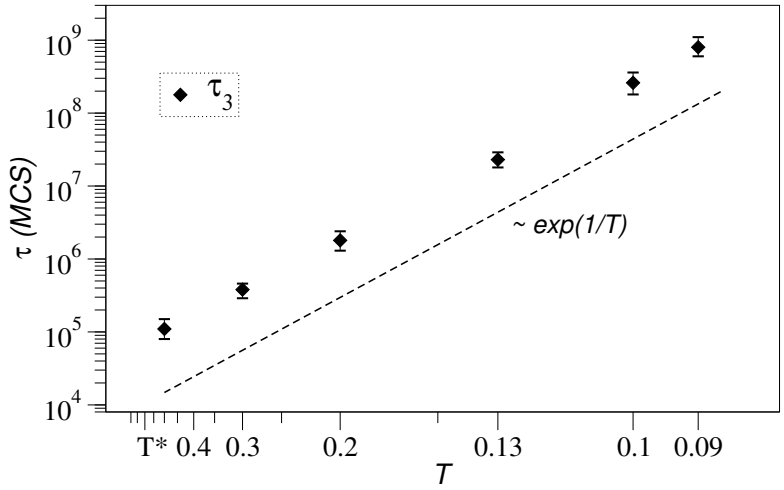


FIGURE 8.11: Characteristic relaxation time τ_3 vs. temperature for $q = 9$ and $L = 100$; dashed line is a guide to the eye.

a superposition of two peaks: τ_2 for stripe states and τ_3 for Lifshitz states. Lifshitz states are only detectable for $L \geq 100$.

Figure 8.11 shows $\tau_3(T)$ with a clear Arrhenius behavior and an activation barrier of 1 (one energy unit, the minimum possible spin-flip barrier). This can be understood from the basic relaxation mechanism of Lifshitz states: the motion of a vertex through the "tooth" mechanism begins with the flip of a neighboring spin at energy cost $1J$ (versus $2J$ for a flat domain wall), after which the tooth can propagate along the three converging walls at zero energy cost. The expected scaling is $\tau_3 \sim L^{\omega} e^{1/T}$.

8.2.2 Probability of blocked states

We analyze the trapping probability $P_b(q)$, defined as the probability of reaching a blocked state (one characterized by flat walls between different domains; for $q \geq 3$ this includes Lifshitz and stripe states).

Figure 8.13 shows results for $q = 9$. At $T > 0$, $P_b(9)$ saturates at a finite value for $L \geq 100$, indicating a finite probability in the limit $L \to \infty$. This probability goes to zero as $T \to 0$, consistent with Spirin et al. [86].

Figure 8.14 shows $P_b(q)$ as a function of q for $T = 0.15$. For $q \geq 3$, $P_b(q)$ falls below a temperature-dependent finite value that is practically independent of q and less than half of $P_b(2)$.

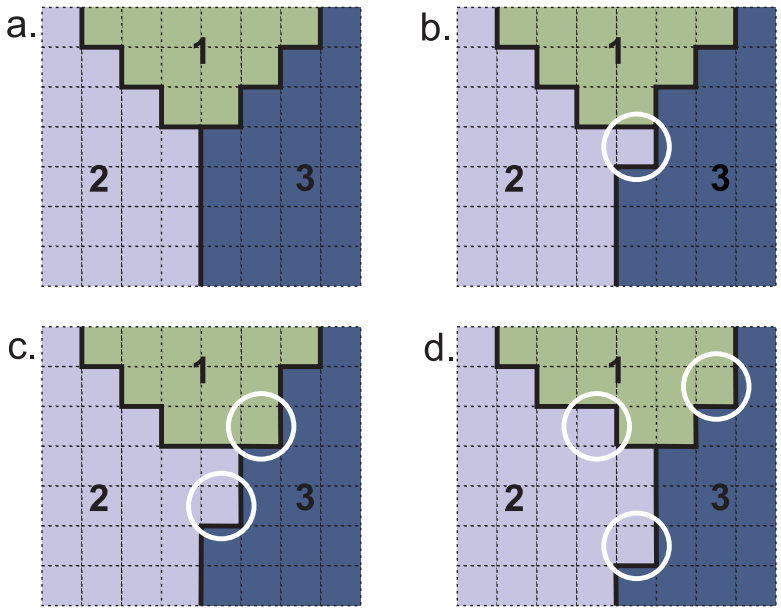


FIGURE 8.12: Basic relaxation mechanism of a Lifshitz state at low temperature. Circle in (b) highlights the creation of a tooth at the vertex in (a), flipping spin $2 \to 3$. Circles in (c) and (d) mark spins that can flip at zero energy cost along the three converging walls. The complete process leads to a jump of the whole structure and ultimately to the collapse of two vertices.

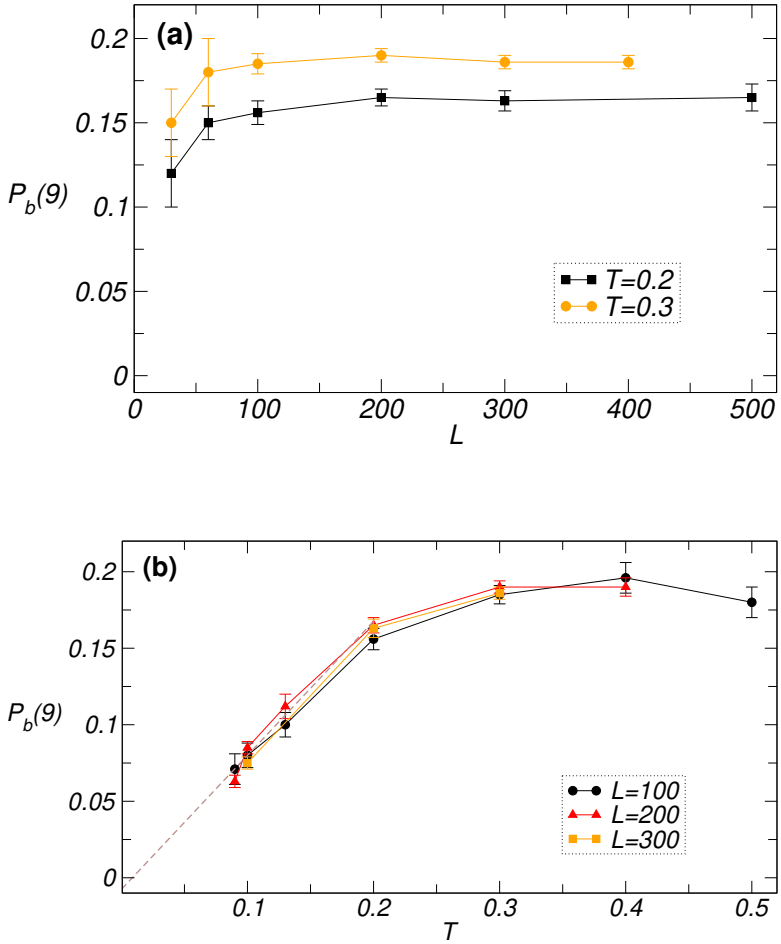


FIGURE 8.13: Trapping probability $P_b(q)$ for $q = 9$: (a) as a function of L for different temperatures; (b) as a function of T for different sizes. Dashed lines are linear fits for $L = 200$, giving an extrapolated value of 0.008 ± 0.01 at $T = 0$.

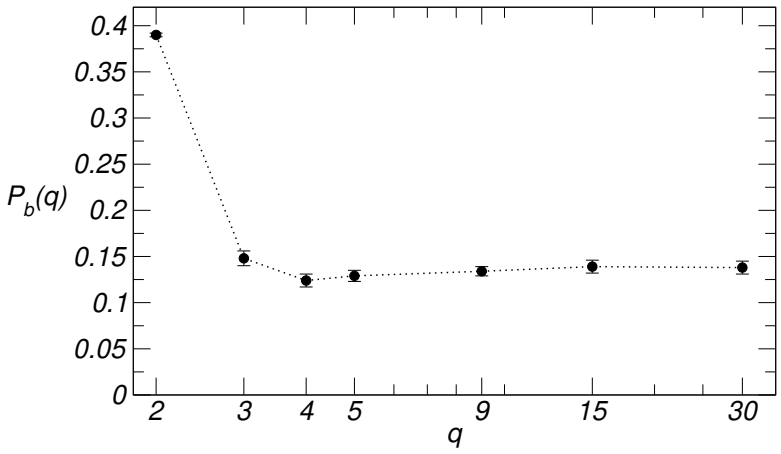


FIGURE 8.14: Trapping probability $P_b(q)$ for $L = 200$ and $T = 0.15$.

8.2.3 Relaxation at low temperatures: glassy state

The increase of τ_1 for $T < 0.2$ observed in Fig. 8.3 indicates that ordinary coarsening is affected by activated processes. This is associated with the plateau that appears in the relaxation function for $T < T_g$ (Fig. 8.15), where $0.1 < T_g < 0.2$ for $q = 9$. The plateau corresponds to a disordered metastable state — the glassy state — with nearly square domains of wide size distribution (see snapshots in Fig. 8.9 or inset in Fig. 8.16). This state has been identified as a glassy state [116–118] and only exists for [119] $q > 4$.

Figure 8.16 shows the relaxation function for $q = 9$, $T = 0.1$, and different system sizes. The relaxation time τ_1 does not depend on size for $L > 200$, showing that the glassy state lifetime remains finite in the thermodynamic limit.

Once the system relaxes from the glassy state it may either equilibrate directly or become trapped again in a blocked state (Fig. 8.9).

Relaxation law for the glassy state

At $T = 0$ the system converges asymptotically to a disordered stationary phase (the glassy phase) with excess energy $\Delta e^*(q)$ above the ground state for all $q > 4$. The works that first analyzed this phase [116,117,119] proposed that the ordering dynamics at $T = 0$, after a brief initial period, can be described by a power-law excess energy:

$$\Delta e(t, q) = \Delta e^*(q) + a(q)t^{-1/2}. \tag{8.2}$$

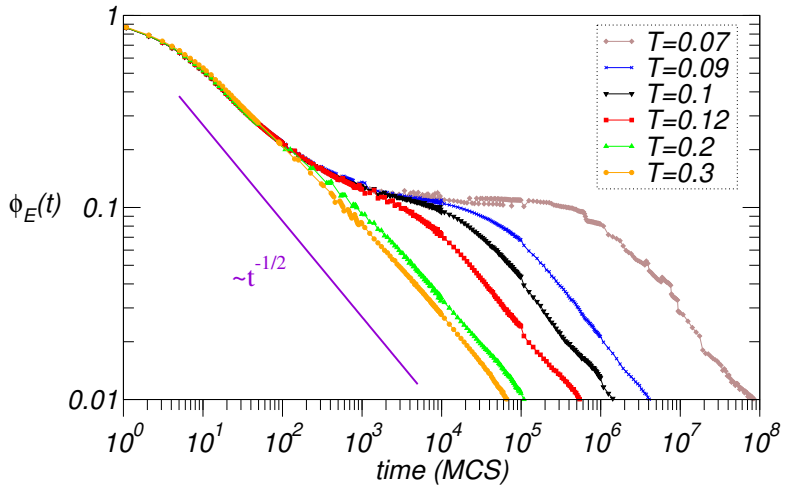


FIGURE 8.15: Relaxation function for $q = 9$, $L = 200$, and temperatures around T_g. Temperatures increase from right to left.

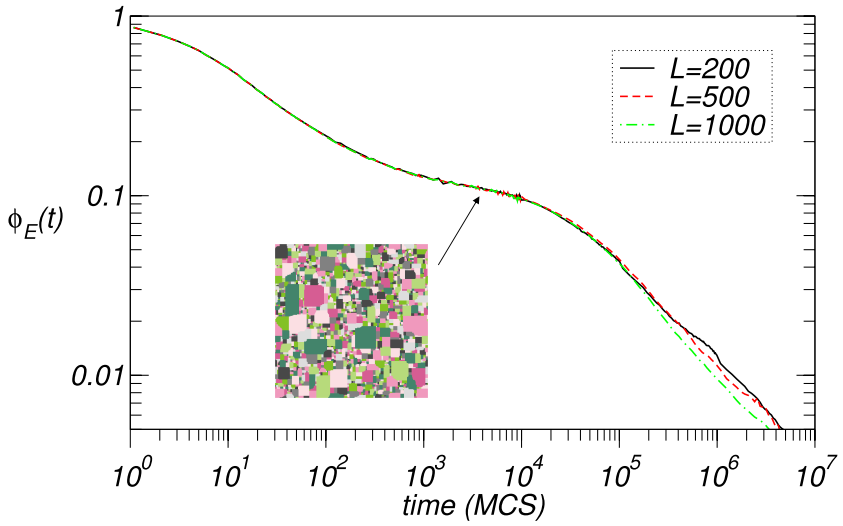


FIGURE 8.16: Relaxation function for $q = 9$, $T = 0.1$, and different L values. Inset: typical configuration of the glassy state associated with the plateau.

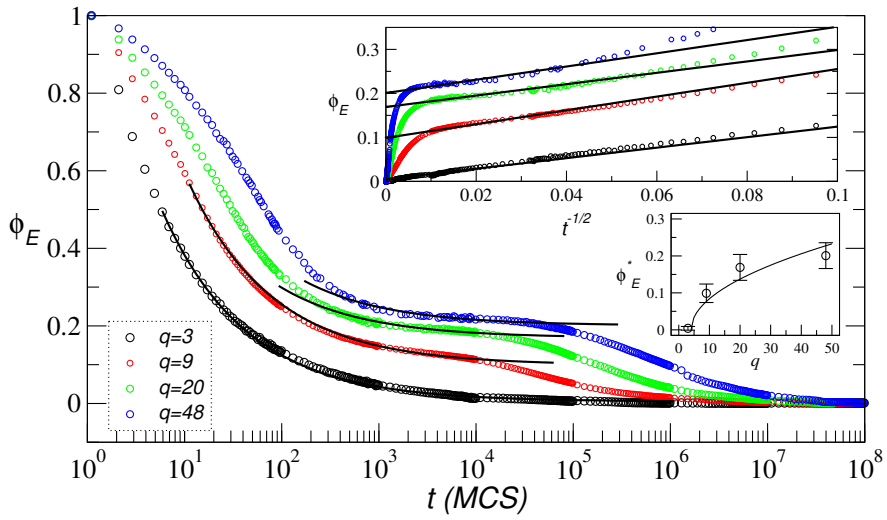


FIGURE 8.17: Normalized energy excess ϕ_E vs. time for $q = 3, 9, 20, 48$ (increasing energy order). Upper inset: Δe vs. $t^{-1/2}$ and fit with the inhomogeneous LAC law, Eq. (8.3). Lower inset: fit results $\phi_E^*(q)$ (circles), and the function $b(q-4)^{1/2}$ with $b = 0.034$, consistent with the zero-temperature result of [118] (line).

Since the energy excess is proportional to the interface perimeter, $\phi_E \sim \ell^{-1}$, this implies that domains do not grow indefinitely but that the characteristic size ℓ converges to a finite limit $\ell^*(q)$. Writing equivalently:

$$\phi_E(t, q) = \phi_E^*(q) + c(q)t^{-1/2}. \tag{8.3}$$

Ibañez de Berganza et al. [119] observed for $q = 7$ at $T = 0.1$ that the inhomogeneous Allen–Cahn law (8.2) (valid at $T = 0$) holds with the same functions $e^*(q)$ and $a(q)$, but only until an escape time $\tau_e(T, q)$, after which LAC growth resumes and the system equilibrates.

Figure 8.17 shows this phenomenology for $q = 3, 9, 20, 48$ after a quench to $T = 0.1$. The case $q = 3$ exhibits a pure power law with $\phi_E^*(q = 3) = 0$. For $q > 4$, $\phi_E^*(q) > 0$ and grows with q, following $\phi_E^*(q) = b(q-4)^{1/2}$ with $b = 0.034$ (consistent with [118]). The escape time $\tau_e(T, q)$ also grows with q. For large q (e.g., $q = 48$) the coefficient $c(q)$ is so small that the energy is practically constant in the interval $\tau_i(q) < t < \tau_e(q)$, suggesting the validity of the power-law form (8.3) would break down in the large-q limit.

De Oliveira [126] proposed a generalization of (8.2) for finite temperature,

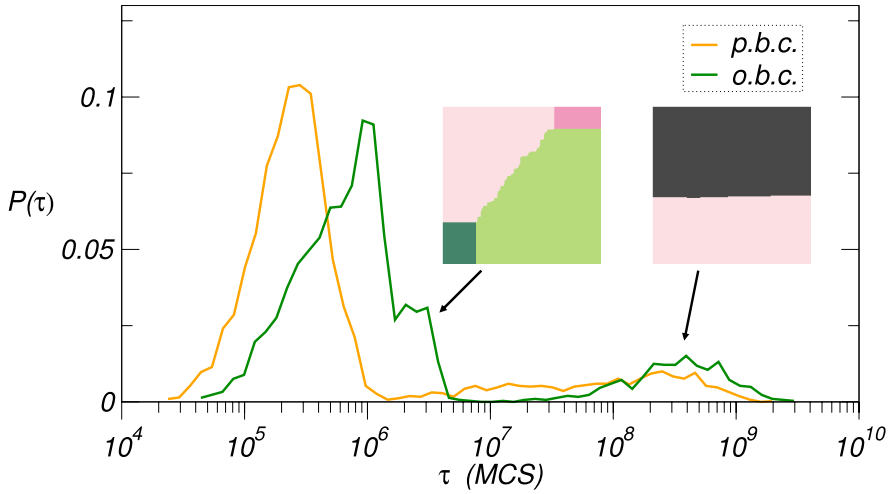


FIGURE 8.18: Probability distribution $P(\tau)$ for $q = 9$, $L = 200$, $T = 0.2$, with periodic (p.b.c.) and open (o.b.c.) boundary conditions. Inset images show typical blocked-state configurations with o.b.c.

valid for the glassy relaxation regime $T < T_g$:

$$\Delta e(t) = \frac{b}{\sqrt{\lambda_{co} t}} + \frac{b}{\sqrt{\lambda_{ac} t + 1}} \tag{8.4}$$

where λ_{co} and λ_{ac} (for *coarsening* and *activation*) are T-dependent parameters, and b is a constant. At low finite temperatures $\lambda_{ac} = e^{1/kT}/T$. This expression fits the curves of Figs. 8.15 and 8.17 acceptably.

8.2.4 Boundary conditions

Finally, we analyze the influence of boundary conditions. Repeating some calculations with open boundary conditions, we find that the complete relaxation scenario found with periodic boundary conditions is reproduced qualitatively. The relaxation times associated with stripe states are of the same order of magnitude. The Lifshitz states with open boundary conditions no longer consist purely of hexagons for relatively small sizes (due to the boundary effects), but we can clearly see the stable three-color vertices.

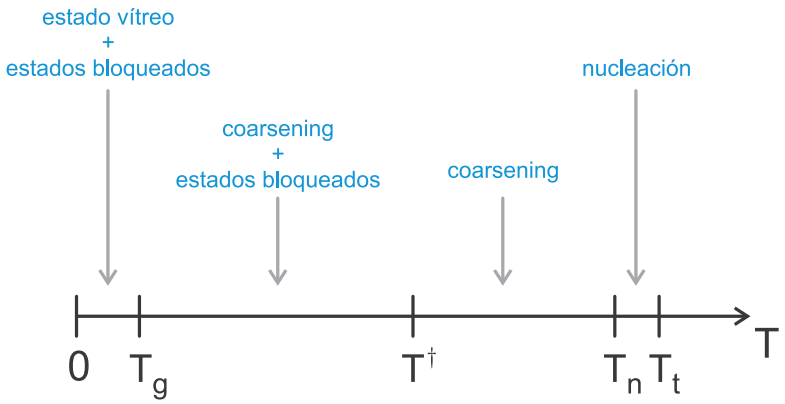


FIGURE 8.19: Dynamical regimes in the long-time relaxation of the q-state Potts model with $q > 4$ after a quench from infinite temperature to subcritical temperatures T.

8.3 Chapter conclusions

The main conclusion of this chapter is summarized in the schematic of Fig. 8.19. After a quench from infinite temperature to subcritical temperatures, the Potts model with spin-flip dynamics and $q > 4$ exhibits distinct relaxation regimes, determined by different characteristic crossover temperatures:

1. **High temperatures ($T^\dagger < T < T_t$):** simple LAC coarsening dominates, $\ell(t) \sim t^{1/2}$, leading to equilibrium for most realizations (except near T_t where nucleation effects appear).

2. **Intermediate temperatures ($T_g < T < T^\dagger$):** LAC coarsening is interrupted with finite probability by trapping in highly symmetric blocked states (stripe and Lifshitz configurations). Subsequent relaxation is thermally activated, with Arrhenius timescales $\tau_2 \sim e^{2/T}$ (stripe) and $\tau_3 \sim e^{1/T}$ (Lifshitz) much larger than those of ordinary coarsening.

3. **Low temperatures ($T < T_g$):** the system is always trapped at early times in glassy states — highly disordered metastable configurations with a finite, size-independent lifetime that diverges as $T \to 0$.

This three-regime picture directly refutes the simple two-scenario (nucleation or coarsening) picture prevalent in the literature, demonstrating that the dynamics of systems with degenerate ground states is significantly richer. The characteristic temperatures $T^\dagger$ and T_g, the trapping probabilities, and the various relax-

ation timescales all exhibit systematic dependence on q, with dynamical frustration growing stronger with increasing q. These findings have direct implications for the modeling of physical systems (grain growth in materials, soap foam dynamics, biological cell dynamics) based on the q-state Potts model.

Temperature has a dual role in the relaxation through blocked states: at short timescales it increases the probability of reaching those states (which is zero at $T = 0$), and at long timescales it allows the system to escape from them via activated processes.

The Lifshitz prediction [77] is confirmed in the q-state Potts model for $q \geq 3$ on the square lattice, provided the system size is sufficiently large. The finite-size effect is strong (large systems are needed to eliminate the influence of the square lattice symmetry) and one would expect it to be smaller on a lattice with 3-fold symmetry (e.g., triangular).

Additional material for this chapter (videos of numerical simulations) can be found at [127].

Part III

Conclusions

CHAPTER 9

CONCLUSIONS

The overarching aim of this thesis was to study relaxation in systems exhibiting first-order phase transitions and related phenomena (e.g., spinodal points), using the q-state Potts model as a paradigmatic and tractable framework.

One of the most important techniques employed was Short-Time Dynamics (STD), which rests on a dynamical extension of the static scaling hypothesis. Although the generalized STD scaling hypothesis had been corroborated numerically in many cases, it had not previously been validated analytically. To better understand the technique, we sought analytical solutions for the particular case of the Curie–Weiss model, which also exhibits a first-order transition (field-driven).

STD in mean-field models

Solving the associated Fokker–Planck equation, we obtained closed-form expressions for the first moments of the order parameter near both critical and spinodal points. This allowed us to confirm the STD scaling hypothesis analytically in both cases and to determine its domain of validity. In particular, we confirmed analytically — for the first time — the validity of the STD scaling hypothesis when the system starts from an ordered initial state. We also found that the diffusive scaling of the second moment holds for any initial value of the order parameter, with the diffusion coefficient exhibiting a crossover between two values at short and intermediate times within the STD regime.

The scaling of the first moment is governed primarily by the drift potential $V(m) = -\int D_1(m)\, dm$ and hence by the extended free energy $f_3(T, H, m)$, which has the same extremal structure as $V(m)$. The scaling of higher moments, on the other hand, originates in the Gaussian character of finite-size fluctuations near singular points.

Although our results were obtained for a specific mean-field model, they depend only on the form of $V(m)$ and the proportionality $D_2 \propto 1/N$, making them of broad applicability to generic mean-field models.

Spinodal points in the Potts model

We demonstrated that spinodal points can be defined from the STD behavior of short-range systems. The STD method detects a point in the phase diagram where the dynamics is critical (at least for a finite time). In mean-field systems this coincides with the thermodynamic spinodal (defined as the zero of the second derivative of the extended free energy); in finite-dimensional systems it provides a definition of the spinodal at a point where metaequilibrium measure-

ments are impossible (beyond the kinetic spinodal). For the 2D Potts model this dynamically defined spinodal coincides with the pseudospinodal obtained from extrapolations of metaequilibrium relaxation times, and our results are consistent with the scaling behavior expected of a growing correlation length.

For all $q > 4$, the STD method yields spinodal temperatures $T_{\mathrm{SP}}^{(\pm)}$ that are distinct from T_t, even in the thermodynamic limit. The apparent convergence of spinodal and transition temperatures for small q near the second-order boundary ($q = 4$) is thus attributable to the extreme weakness of the transition, not to the absence of a spinodal.

The STD approach to spinodals has practical advantages beyond conceptual clarity: it avoids equilibration difficulties and may be applicable to systems with very slow dynamics (such as glass-forming liquids) where metaequilibrium measurements are out of reach. We stress that our definition does not imply a thermodynamic singularity at the spinodal — it is fundamentally a dynamical definition, and in that sense is most accurately compared to the pseudospinodal, but determined in a way that avoids the pitfalls of equilibration and extrapolation.

Metastability and GPU simulations

To investigate metastability in the Potts model further, we implemented a highly optimized parallel GPU-based Monte Carlo algorithm. Using this algorithm, we simulated systems of up to $\sim 10^9$ spins with a speedup of up to $155\times$ over an optimized serial implementation, enabling us to apply the Binder criterion with high precision. Our results provide positive numerical evidence for the persistence of metastability in the thermodynamic limit for $q \geq 9$, consistent with the spinodal temperatures obtained from STD. For $q = 6$ the evidence is suggestive but not conclusive; we cannot exclude a critical value $4 < q^* \leq 9$ below which metastability disappears.

Regarding nucleation from the metastable state, we observe phenomena not fully captured by Classical Nucleation Theory. In general (except for very large q or very near T_t), spatial correlations begin to grow before the critical nucleus appears, leading to a collective, self-organized precursor mechanism. A systematic study exploring the full parameter space remains to be done.

Low-temperature relaxation dynamics

Finally, we conducted a systematic study of the low-temperature relaxation dynamics of the q-state Potts model after a quench to subcritical temperatures. The

main conclusions are encapsulated in the following picture of distinct dynamical regimes for $q>4$:

- For $T_n < T < T_t$ (near the transition): relaxation dominated by nucleation.
- For $T^* < T < T_n$ (intermediate): Lifshitz–Allen–Cahn coarsening, $\mathcal{L}(t) \sim t^{1/2}$, leading to equilibrium for most realizations.
- For $T_g < T < T^*$ (low temperatures): LAC coarsening is interrupted with finite probability by trapping in highly symmetric blocked states — stripe configurations and honeycomb (Lifshitz) configurations. Subsequent relaxation is thermally activated, with Arrhenius timescales much larger than those of ordinary coarsening.
- For $T < T_g$ (very low temperatures): the system is always trapped at early times in disordered glassy states with a finite, size-independent lifetime that diverges as $T \to 0$.

This multi-regime picture definitively replaces the simple two-scenario (nucleation or coarsening) picture prevalent in earlier literature. The dynamical frustration — induced by the high degeneracy of the Potts ground state and growing with q — generates a rich hierarchy of timescales and dynamical states in a simple ferromagnetic model, without any explicit disorder or competing interactions in the Hamiltonian. We believe that such dynamically emergent collective effects may be relevant to other spin models where complex phenomenology is commonly attributed to model-specific ingredients (imperfections, vacancies, competing couplings).

Technical contributions

On the technical side, our GPU-based Monte Carlo implementation demonstrated that graphics cards can serve as highly effective accelerators for Statistical Mechanics simulations, achieving an average spin-flip time of 0.147 ns and enabling simulation of $\sim 10^9$ spins with an average MCS time of ~ 0.15 s. The CUDA code is available for download under the GNU GPL 3.0 license. While the implementation was designed for a 2D nearest-neighbor model with a checkerboard update scheme, extension to 3D and/or longer-range interactions is straightforward.

Part IV

Appendices

APPENDIX A

SUPPLEMENTARY CALCULATIONS FOR STD IN MEAN-FIELD SYSTEMS

This appendix provides detailed calculations that complement Chapter 6.

A.1 Quartic potential approximation near the critical point

To analyze the effect of including the cubic correction in the drift coefficient Eq. (6.9), we evaluate the particular case of Eq. (6.3):

$$\langle m^n \rangle = \sum_{k\geq 0} [(-\omega m_0 - \kappa m_0^3)\partial_{m_0} + \epsilon \partial_{m_0 m_0}]^k \frac{m_0^n\, t^k}{k!}\,. \tag{A.1}$$

In the limit $|\lambda\, N| \gg 1$, we can neglect the diffusive term to leading order and compute:

$$\langle m \rangle \approx \sum_{k\geq 0} [(-\omega m_0 - \kappa m_0^3)\partial_{m_0}]^k \frac{m_0\, t^k}{k!}\,.$$

Iterating the operator k times and identifying the general form of the coefficients of t^k, with the aid of symbolic computation software, we obtain:

$$\begin{aligned}
\langle m \rangle &\approx m_0 \sum_{k,j\geq 0} \frac{(-\omega t)^k}{k!} \left(\begin{array}{c} 2j \\ j \end{array} \right) \left(-\frac{m_0^2 \kappa}{4\omega}\right)^j \sum_{i=0}^{j} \left(\begin{array}{c} j \\ i \end{array} \right) (-1)^i (2i+1)^k \\
&= m_0 \mathrm{e}^{-\omega t} \sum_{j\geq 0} \left(\begin{array}{c} 2j \\ j \end{array} \right) \left(-\frac{m_0^2 \kappa}{4\omega}(1-\mathrm{e}^{-2\omega t})\right)^j \\
&= \frac{m_0 \mathrm{e}^{-\omega t}}{\sqrt{1 + m_0^2 \kappa (1-\mathrm{e}^{-2\omega t})/\omega}}\,,
\end{aligned} \tag{A.2}$$

which coincides with the exact deterministic solution (6.17).

Fluctuations can be neglected as long as $\kappa, \omega \sim O(\epsilon^0)$. However, while 3κ remains of order one (except at extreme temperatures), typically $\omega \sim \lambda + \epsilon \ll 1$. We can then include a finite-size correction, keeping only terms of order ϵ and ω in each coefficient of t^k in Eq. (A.1). This procedure yields the correction:

$$\begin{aligned}
C_1(\epsilon) &= -\epsilon \kappa m_0 t^2 \sum_{k\geq 0} \left(\begin{array}{c} 2k \\ k \end{array} \right) (2k^2 + 6k + 3)(-z/2)^k \\
&= -\epsilon \kappa m_0 t^2 \frac{3 + 4z + 2z^2}{(1+2z)^{5/2}}\,,
\end{aligned}$$

where $z \equiv \kappa m_0^2 t$. The result is:

$$\begin{aligned} \langle m \rangle &= \frac{m_0(1-\omega t)}{(1+2z)^{1/2}} + \frac{m_0 \omega t\, z}{(1+2z)^{3/2}} \\ &\quad -\epsilon\kappa m_0 t^2 \frac{3+4z+2z^2}{(1+2z)^{5/2}} + \mathcal{O}(\epsilon^2, \epsilon\omega, \omega^2)\,. \end{aligned} \tag{A.3}$$

Note that the first two terms on the right-hand side come from the expansion of the deterministic equation Eq. (A.2) to first order in ω.

In particular, exactly at the critical point we have $\kappa = 1/3$ and $\lambda = 0$ (hence $\omega = \epsilon$). Thus, as in the Ornstein–Uhlenbeck approximation, we conclude that the magnetization remains $m \simeq m_0$ up to a characteristic time $\tau_0 \sim 1/\epsilon = N$.

Similarly, for $\langle m^2 \rangle$ we obtain the correction:

$$C_2(\epsilon) = \epsilon t \sum_{k\geq 0} (k+1)(k+2)(-2z)^k = \frac{2\epsilon t}{(1+2z)^3}\,,$$

which leads to:

$$\langle m^2 \rangle = \frac{m_0^2}{(1+2z)} - \frac{2\omega z(1+z)}{\kappa(1+2z)^2} + \frac{2\epsilon t}{(1+2z)^3} + \mathcal{O}(\epsilon^2, \epsilon\omega, \omega^2)\,. \tag{A.4}$$

Since in the deterministic limit $\langle m^n \rangle = \langle m \rangle^n$, the first two terms on the right-hand side come from the expansion to first order in ω of the square of Eq. (A.2).

In computing the centered second moment using Eqs. (A.3) and (A.4), the purely deterministic terms cancel to give Eq. (6.20).

A.2 Moment calculations near the spinodal

Setting $\epsilon = 0$, from Eq. (6.3) with $D_1 = -A(x^2 + 2A\alpha x - \alpha)$, $\alpha = \Delta h/(\beta J\, A)$, and $A \equiv \beta J\, m_{SP}$, the mean magnetization is:

$$\langle \Delta m \rangle = \sum_{k\geq 0} [-(x^2 + 2A\alpha x - \alpha)\, \partial_x]^k x\, (At)^k/k!\,, \tag{A.5}$$

where $x \equiv m_0 - m_{SP}$.
Completing the square and making the change of variables $u = (x + A\alpha)/\sqrt{\gamma}$ with $\gamma = \alpha + A^2\alpha^2$ we obtain:

$$\langle \Delta m \rangle = \sqrt{\gamma} \sum_{k\geq 0} [(1-u^2)\, \partial_u]^k u\, (\sqrt{\gamma} At)^k/k! - A\alpha\,. \tag{A.6}$$

Using the generating function for the tangent with the substitution $u = \tanh z$ we have [128,129]:

$$\begin{aligned}\sum_{n\geq 0}[(1-u^2)\partial_u]^n\, u\,\tau^n/n! &= \sum_{n\geq 0}[\partial_z]^n \tanh z\,\tau^n/n! \\ &= (u+\tanh\tau)/(1+u\tanh\tau)\,,\end{aligned}$$

from which Eqs. (6.23)–(6.24) follow.

To include finite-size effects, we must consider the full expression:

$$\langle \Delta m\rangle = \sum_{k\geq 0}[D_1\partial_x + D_2\partial_{xx}]^k \frac{x\,t^k}{k!}\,. \tag{A.7}$$

When $\Delta h = 0$, from Eq. (6.21), we have $D_2(x) \simeq \epsilon(ax^2+bx+c)$, with $a = \beta J - 2$, $b = -2m_{SP}$, $c = 1/\beta J$, and $D_1 = -Ax^2$. The order-ϵ contributions associated with each coefficient in the quadratic approximation of $D_2(x)$ are:

$$C_{1a} = -\frac{\epsilon a}{3A}\sum_{k\geq 2}(k^2-1)(-y)^k = -\frac{\epsilon a y^2(3+y)}{3A(1+y)^3}\,,$$

$$C_{1b} = \frac{\epsilon bt}{12}\sum_{k\geq 2}(k+1)(3k-2)(-y)^{k-1} = -\frac{\epsilon bty(6+4y+y^2)}{6(1+y)^3}\,,$$

$$C_{1c} = -\epsilon cAt^2\left(1+\frac{1}{10}\sum_{k\geq 2}(k+2)(2k+1)(-y)^{k-1}\right) = -\frac{\epsilon cAt^2(10+10y+5y^2+y^3)}{10(1+y)^3}\,,$$

where $y \equiv Axt$.

Adding the order-ϵ corrections $C_{1a}+C_{1b}+C_{1c}$ together with the deterministic term given by Eq. (6.25), we obtain:

$$\begin{aligned}\langle \Delta m\rangle &= \frac{x}{1+y} - \Big(\frac{c}{10Ax^2}(10+10y+5y^2+y^3)+ \\ &\quad +\frac{b}{6Ax}(6+4y+y^2)+\frac{a}{3A}(3+y)\Big)\frac{\epsilon\, y^2}{(1+y)^3}\,.\end{aligned} \tag{A.8}$$

Similarly we compute:

$$\langle (\Delta m)^2\rangle = \sum_{k\geq 0}[D_1\partial_x + D_2\partial_{xx}]^k \frac{x^2\,t^k}{k!}\,. \tag{A.9}$$

In this case the order-ϵ contributions are:

$$C_{2a} = -\frac{2ax}{A}\sum_{k\geq 1}\left(\begin{array}{c} k+2 \\ 3 \end{array}\right)(-y)^k = \frac{2axy}{A(1+y)^4}\,,$$

$$C_{2b} = -\frac{b}{12A}\sum_{k\geq 1}(k+1)(k+2)(3k+1)(-y)^k = \frac{by(12+6y+4y^2+y^3)}{6A(1+y)^4}\,,$$

$$C_{2c} = ct\left(2+\frac{1}{10}\sum_{k\geq 2}(k+1)(k+2)(2k+1)(-y)^{k-1}\right) = \frac{ct(10+10y+10y^2+5y^3+y^4)}{5(1+y)^4}\,.$$

Adding the corrections $C_{2a}+C_{2b}+C_{2c}$ together with the deterministic term (the square of Eq. (6.25)), we arrive at:

$$\begin{aligned}\langle(\Delta m)^2\rangle &= \frac{x^2}{(1+y)^2} + \Big(\frac{c}{5x}(10+10y+10y^2+5y^3+y^4)+ \\ &\quad +\frac{b}{6}(12+6y+4y^2+y^3)+2ax\Big)\frac{\epsilon\, y}{A(1+y)^4}\,. \qquad \text{(A.10)}\end{aligned}$$

Finally, the centered second moment is obtained as $\Delta m^{(2)} = \langle(\Delta m)^2\rangle - (\langle\Delta m\rangle)^2$. The purely deterministic terms cancel and, to first order in ϵ:

$$\begin{aligned}\Delta m^{(2)} &= \frac{\epsilon\, y}{30Ax(1+y)^4}\Big(20ax^2(3+3y+y^2)+ \\ &\quad +15bx(2+y)(2+2y+y^2)+ \\ &\quad +12c(5+10y+10y^2+5y^3+y^4)\Big)+\mathcal{O}(\epsilon^2)\,. \qquad \text{(A.11)}\end{aligned}$$

APPENDIX B

THE CONTINUOUS-TIME MONTE CARLO METHOD

This appendix describes the Continuous-Time Monte Carlo algorithm and its implementation for the q-state Potts model. This implementation was used to obtain the majority of the results published in [4] that are presented in Chapter 8.

B.1 Motivation

In the out-of-equilibrium relaxation measurements presented in Chapter 8, we analyze the evolution under model-A dynamics (non-conserved order parameter) of the system described by Hamiltonian (3.12), after a quench from infinite temperature (i.e., a completely random initial configuration) to temperatures below the critical temperature.

We are primarily interested in the late stages of the dynamics, when relatively large domains have already formed. In this regime, the computational cost of a *single spin flip* dynamics[1] becomes very high. This is because the flip probability of spins inside a domain (which constitute the majority) becomes very small, especially at low temperatures. The spins with the highest flip probabilities are those at domain interfaces or boundaries, where the relaxation dynamics mainly takes place. But boundary spins are far fewer in number than bulk spins (the former scale as L, the latter as L^2). Consequently, in practice, most of the simulation time is "wasted" attempting to flip spins that will almost certainly remain in their current state.

B.2 The n-fold way technique

An efficient way to avoid this problem — and thereby reach long time scales for reasonably large system sizes — is the use of the Continuous-Time Monte Carlo method, originally called *"the n-fold way"* by Bortz, Kalos, and Lebowitz [120].

This method is based on the fact that, at any given time, there is a small number n of spin "classes," distinguished according to their flip probability. For example, in the Ising model on the square lattice with periodic boundary conditions and nearest-neighbor interactions, there are only 10 spin classes[2], enumerated in Table B.1:

The standard single-spin-flip algorithm selects one site from the entire lattice with equal probability, determines which class the spin at that site belongs to (by checking its state and the instantaneous states of its neighbors), and then decides

[1] i.e., dynamics in which one spin is updated per iteration, for example, the standard Metropolis algorithm.

[2] In the presence of a magnetic field that breaks the symmetry, there are even fewer.

TABLE B.1: Spin classification in the 10-fold way. Table adapted from [120].

Class	Spin	# of UP neighbors
1	UP	4
2	UP	3
3	UP	2
4	UP	1
5	UP	0
6	DOWN	4
7	DOWN	3
8	DOWN	2
9	DOWN	1
10	DOWN	0

whether or not to flip it, computing a flip probability P[3] directly related to the class of the spin in question, and comparing it with a random number $r \in (0, 1)$.

The n-fold way, by contrast, selects sites with a weighted probability, such that the probability of choosing a given spin is proportional to its flip probability. Once a spin is selected, the flip is carried out immediately, without any random acceptance test.

The standard algorithm comes with an associated time unit called the *Monte Carlo step* (MCS), typically defined as N flip attempts, where N is the total number of spins. But N iterations of the n-fold way are not equivalent to N iterations of the standard algorithm and therefore do not constitute one MCS. It is necessary to recalculate the time increment associated with each flip.

In the n-fold way, a flip invariably occurs at each iteration, and the time that the occurrence of that event would have taken in a standard Monte Carlo algorithm is computed from the total flip probability associated with the instantaneous configuration. This computation is performed after each flip, and its result is added to the time variable. These time increments are in general fractional (real-valued), so the time variable must also be a real number — hence the name *Continuous-Time* Monte Carlo (CTMC), in contrast to the standard algorithm whose time variable is *discrete*.

[3]Note that the possible values of P can be known *a priori*, since they depend on the state of the site (before and after the potential flip) and those of its neighbors; in practice a precomputed lookup table of P values as a function of the energy change is typically used.

B.3 CTMC implementation for the q-state Potts model

We briefly describe the implementation of the Continuous-Time Monte Carlo (CTMC) algorithm for the q-state Potts model on the two-dimensional square lattice with nearest-neighbor interactions.

For a given spin configuration, we define "potential spins" as the $q-1$ possible spin states for each lattice site, i.e., the $N \times (q-1)$ possible different values not currently occupied at the N sites of that configuration.

All potential spins in the system are classified into lists, such that all members of the same list would produce the same change in the system's energy if chosen to replace the current spin at their site.

Upon flipping (changing) a spin in our model, there are only 9 possible energy changes ($\Delta E/J = -4, -3, -2, -1, 0, 1, 2, 3, 4$). This is independent of the value of q — they are simply the 9 possible differences between two quantities that are each the sum of four Kronecker deltas.

In the Metropolis algorithm, the probability that a potential spin of class l ($l = 1, \ldots, 9$) is actually chosen to occupy its site is:

$$p_l = \frac{n_l}{N(q-1)} \min\left[1, \exp\left(-\frac{\Delta E_l}{k_B T}\right)\right] \tag{B.1}$$

where n_l is the number of potential spins in class l. The total probability that any flip occurs at a given step is:

$$Q = \sum_l p_l \tag{B.2}$$

The algorithm then proceeds as follows: at each step, a list is chosen with probability (B.1), and from it a potential spin is chosen uniformly at random. The state of the corresponding site is updated by replacing the current spin with the chosen potential spin. The old spin now becomes a potential spin, and the chosen spin ceases to be one. The flip also affects the class membership of potential spins at neighboring sites, so those lists are updated as well. After updating the site state and the lists, the time is incremented by:

$$\Delta t = \frac{-\ln r}{NQ} \tag{B.3}$$

where r is a uniformly distributed random number in $(0, 1)$ and the time step Δt is measured in MCS.

B.3.1 Justification of the time increment

Suppose our lattice is immersed in a heat bath at fixed temperature T. The thermal bath generates flip attempts randomly in space and time, such that on average there is one attempt per site per time τ_0. We expect τ_0 to depend on the bath temperature and the nature of the system, but not (or only very weakly) on the state of the system. The probability of flipping *one* spin in a given random attempt is Q. Hence, the probability that some flip occurs in the system during the infinitesimal time interval dt is:

$$p\,dt = (QN/\tau_0)\,dt \tag{B.4}$$

We now compute the distribution of time intervals between flips. Let $P(\Delta t)$ be the probability that no new flips occur until time Δt has elapsed since the previous flip. The probability that no new flips occur until $\Delta t + dt$ must be less than $P(\Delta t)$ by the probability that no flip occurs before Δt but one occurs between Δt and $\Delta t + dt$, which is $P(\Delta t)\,p\,dt$. Hence:

$$P(\Delta t + dt) = P(\Delta t) - P(\Delta t)(QN/\tau_0)dt. \tag{B.5}$$

Rewriting (B.5) as a differential equation:

$$P'(\Delta t) = -(QN/\tau_0)P(\Delta t), \tag{B.6}$$

whose solution with boundary condition $P(0) = 1$ is:

$$P(\Delta t) = \exp(-QN\Delta t/\tau_0). \tag{B.7}$$

We now sample the stochastic time interval between flips: draw a random number r uniformly distributed in $(0, 1)$, set $P(\Delta t) = r$, and solve for Δt:

$$\Delta t = -(\tau_0/QN)\ln r. \tag{B.8}$$

Since τ_0 is assumed independent of the system state, the accumulated time t is approximately proportional to real time. τ_0 is merely a time scale (also present in the standard Monte Carlo algorithm), which we set to 1 for numerical simulations. With $\tau_0 = 1$ we recover Eq. (B.3).

B.4 Validation and performance

Although the Continuous-Time Monte Carlo technique has been widely used in various models (see e.g. [130]), its implementation for the Potts model required development of an original code, as it is not readily available in the literature.

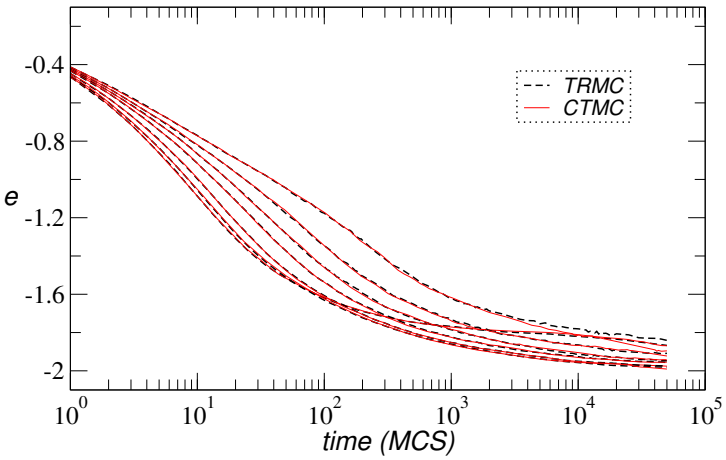


FIGURE B.1: Validation of the Continuous-Time Monte Carlo algorithm: relaxation curves of the energy per spin, for $q = 9$, $L = 300$, and several temperatures between $T = 0.65$ and $T = 0.1$ (top to bottom). Solid red curves correspond to the standard algorithm; dashed black curves correspond to the CTMC algorithm.

As a validation test, we compared simulations using the CTMC algorithm against the standard Metropolis algorithm. Figure B.1 shows energy vs. time curves for relaxation after a quench from infinite temperature to various temperatures T, for $q = 9$ and $L = 300$, obtained with both algorithms. We observe that both algorithms produce identical results at every temperature. We also performed non-equilibrium measurements up to 10^7 MCS and equilibrium measurements with both codes, and the results were identical.

Regarding performance: the speed advantage of the CTMC depends strongly on temperature. As noted, the technique is designed for when large ordered domains have formed. For sufficiently high temperatures, where fluctuations are large and domains form and dissolve rapidly, the technique becomes inefficient: the assumption that most spins have low flip probability no longer holds, and the list management overhead of the CTMC exceeds the per-step cost of the standard algorithm.

Figure B.2 compares execution times for a benchmark case: relaxation of systems with $q = 9$ and sizes $L = 150$ and $L = 300$ over 50000 MCS, at various subcritical temperatures ($T_t(q = 9) = 0.721347$). Both algorithms used the same compiler (*ifort*) with the same compilation options, and timing was measured with the same Fortran internal routine. We observe a speedup of $15\times$–$20\times$ at

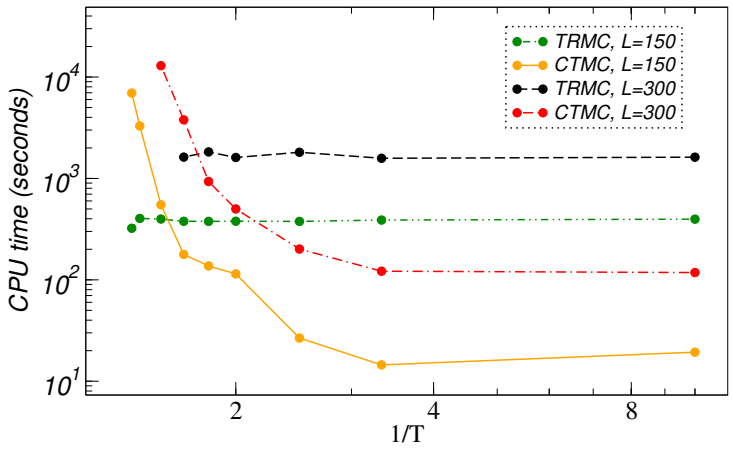


FIGURE B.2: Execution time for a benchmark case (see text) for the standard and continuous-time algorithms as a function of (fixed) simulation temperature, on a log–log scale. Temperatures range from $T = 0.1$ to $T = 0.72$ (right to left). At low temperatures the CTMC is more efficient; near the transition temperature the standard algorithm becomes more efficient.

low temperatures depending on system size — in practice, reducing a simulation that would take a month to less than two days. Moreover, this speedup is much larger (even orders of magnitude larger) for benchmarks involving several hundred million MCS. For instance, in cases where the system becomes trapped in a blocked state at low temperatures and we need to simulate very long time scales ($> 10^{10}$ MCS) to observe relaxation to equilibrium, standard MC simulation times become prohibitive in practice, while the CTMC algorithm delivers results in a reasonable time.

This implementation allowed us to perform simulations at time scales between 10^9 MCS (for sizes up to $L = 500$) and 10^{14} MCS (for sizes up to $L = 100$), with good sampling statistics — timescales not previously reached in spin lattice simulations to our knowledge. In individual runs we exceeded 10^{15} MCS on desktop computers.

APPENDIX C

GPU IMPLEMENTATION OF THE q-STATE POTTS MODEL

In this appendix we present a CUDA implementation for GPGPU computing of Monte Carlo simulations of the two-dimensional ferromagnetic q-state Potts model.

The tremendous progress enabled by numerical simulations in recent decades has elevated these techniques to the status of indispensable tools in modern Statistical Mechanics research. Nevertheless, many theoretical problems in the field remain challenging due to limitations in available computational resources. Among many others, topics that resist numerical treatment include systems with slow dynamics and/or strong finite-size effects, requiring fast simulations to reach different timescales and/or a large number of particles. Typical examples are spin glass transitions [131], glassy behavior [81,132], and domain growth [133]. In these types of problems, the state of the art is usually set by new numerical approaches or extensive simulations. In this sense, the advent of massive parallel computing capabilities continually opens new possibilities, while simultaneously creating a demand for new algorithms optimized for each architecture or parallelism platform.

In particular, the use of GPUs as parallel processing devices emerges as a powerful tool for numerical simulations in Statistical Mechanics systems [134–137], as well as in other areas of physics [138–140]. The model employed for this technology is based on the combined use of a CPU and a GPU in a heterogeneous coprocessing system. The sequential part of the program runs on the CPU, and the computationally heavy parts are accelerated on the GPU, which acts as a massively parallel processing peripheral. From the user's perspective, the application simply runs faster because it exploits the GPU's large capacity to multiply throughput.

This appendix is based on a work in collaboration with Mr. Juan Pablo De Francesco and Lic. Nicolás Wolovick of FaMAF [Ferrero et al., submitted to *Comp. Phys. Commun.* (2011)]. The code development and the results presented here are of shared authorship.

C.1 What is GPGPU? What is CUDA?

Originally designed and developed for the video game industry, graphics cards (commonly called GPUs, for Graphics Processing Units) currently possess computing power that substantially exceeds that of a CPU (Central Processing Unit). This capability results from the relative simplicity of a GPU's architecture compared to a CPU, combined with a large number of parallel processing units (cores)

on a single chip.

In 2006, NVIDIA, one of the leading GPU manufacturers, decided to adopt a new design path and launched the G80 graphics processing unit, moving away from the conventional rendering paradigm and transforming the GPU into a practically general-purpose computing unit. In 2007 NVIDIA launched the CUDA SDK, a software development kit designed for programming their G80 using the C language with some extensions. CUDA stands for Compute Unified Device Architecture, but the name CUDA is also used for the programming model associated with this architecture. The G80 hardware and the CUDA compiler quickly demonstrated a good ratio of GFLOPS per watt and GFLOPS per dollar for numerical algorithms. The architecture evolved in two generations: GT200 in 2008–2009, and GF100 in 2010 (also known as the Fermi architecture).

C.2 Device architecture and GPGPU programming overview

All NVIDIA GPU architectures share the same SIMT (*Single Instruction, Multiple Thread*) concurrency paradigm in order to exploit high parallelism (up to 512 computing cores) and large memory bandwidth (up to 177 GBps). The SIMT model is a convenient abstraction that sits between the traditional SIMD (*Single Instruction, Multiple Data*) and MIMD (*Multiple Instruction, Multiple Data*) paradigms.

Using the SIMT paradigm, parallel algorithm development changes appreciably, since it is possible to code for millions of threads in parallel. The overhead of creating, switching, and destroying threads is so low that multiplying a matrix by a scalar reduces to launching one kernel per matrix element — even for a 32768×32768 matrix (on the order of 1 GThread). In fact, launching as many threads as possible is advantageous since high global-memory latency (around 200 cycles) is hidden by swapping warps[1] that are waiting for memory responses.

The role of blocks in the SIMT model is important. Threads are divided into blocks, where each block of threads has two special characteristics: a private shared memory between its threads, and the ability to synchronize thread execution via barriers. Internally, cores in a GPU chip are organized in multiprocessors called SMs (*Streaming Multiprocessors*), and each block is assigned to a specific SM for execution. Shared memory can thus be used as a manually managed cache, which in many cases improves performance appreciably.

We used the GTX 280, GTX 470, and GTX 480 platforms. Table C.1 shows the relevant hardware parameters. The improvements of the Fermi architecture rely on new computing capabilities provided by an improved ISA (*Instruction Set*

[1] vectors of 32 threads executed synchronously

TABLE C.1: Main specifications of NVIDIA GTX 280, GTX 470, and GTX 480 boards

Board Model	GTX 280	GTX 470	GTX 480
Available	Q2 2008	Q1 2010	
GPU	GT200	GF100	
CUDA capability	1.3	2.0	
CUDA cores	240	448	480
Processor Clock	1.30GHz	1.22GHz	1.40GHz
Global Memory	1GB	1.25GB	1.50GB
Memory Bandwidth	141.7GBps	133.9GBps	177.4GBps
L1 Cache	N/A	16KB/48KB	
L2 Cache	N/A	768KB	
Max # of Threads per Block	512	1024	
Shared Memory per Block	16KB	48KB/16KB	
Max # of Registers per Block	16384	32768	

Architecture), doubled core count, inclusion of L1 and L2 caches, and increased parallelism and shared memory per block.

As with any modern computing architecture, the "memory wall" effect must be mitigated using a memory hierarchy (faster, more expensive and smaller at the top). The first level is global memory, accessible by all cores, with 1GB to 1.5GB capacity and a latency of around 200 cycles. The next level is shared memory, 16KB per block, with a latency of only 2 cycles. At the top there are 16384 registers per block. There are also fast memories for constant and texture registers with special addressing capabilities.

The programming interface for this architecture is "C for CUDA", an extension of the C programming language [141] that allows the CPU host to launch kernels on the GPU device [142]. A kernel is a typically small piece of code compiled by `nvcc`, NVIDIA's CUDA compiler, to the PTX assembler that the architecture can execute. The kernel is executed simultaneously by many threads organized logically in a 2D (grid, block) coordinate system. Thread position information is stored in special variables, the block and thread identifiers (bid, tid). Based on thread coordinates, the kernel obtains the memory locations of the data to operate on. At this abstraction level there is no need to worry about the number of GPU cores — all threads in a kernel call proceed in parallel for all practical purposes.

In addition to CUDA, a compiler for CUDA Fortran is commercially available, and wrappers exist for using the CUDA architecture from Python, Perl, Java, MATLAB, IDL, Mathematica, etc. Since 2008, a consortium led by Apple (The

Khronos Group) has been developing OpenCL, a programming environment for heterogeneous platforms comprising CPUs, GPUs, and other processors, which has been adopted by AMD/ATI for general-purpose GPU computing.

C.3 Optimized GPU-based Monte Carlo algorithm for the q-state Potts model

We developed a GPGPU-based code to simulate the statistical mechanics of the 2D Potts model (with Hamiltonian 3.12) using classical Metropolis dynamics on an $N = L \times L$ square lattice with periodic boundary conditions.

For spin updates we partition the lattice into two subsets (black and white sites), treating it as a large checkerboard. Since interactions are restricted to nearest neighbors, all sites of the same color can be updated fully asynchronously[2] This technique is also known as the Red-Black Gauss-Seidel scheme [143].

The algorithm allowed us to analyze equilibrium states of systems of up to $N = 32768 \times 32768$ ($2^{15} \times 2^{15} \approx 1.073 \times 10^9$ spins).

The typical simulation protocol is: starting from an ordered initial state ($s_i = 1$ for all i), fix the temperature at $T = T_{\min}$ (typically $T_{\min} < T_t$) and run for t_{tran} steps to equilibrate, then run for $t_{\max}$ steps taking a measurement every δt steps. The last configuration is used as the initial state for the next temperature $T = T_{\min} + \Delta T$. This process is repeated up to $T_{\max}$. The entire loop is repeated for many samples to average over different thermal noise realizations. Equilibrium measurements starting from a completely random state and sweeping from $T_{\max}$ to $T_{\min}$ are also performed.

Our code is divided into two main functions: spin update and computation of physical quantities. The update function is implemented in the host code `update`, which calls the device kernel `updateCUDA` twice (once for white cells, once for black cells). The computation of energy and magnetization is carried out by `calculate`, which calls the `calculateCUDA` kernel and two auxiliary kernels: `sumupECUDA` and `sumupMCUDA`.

C.3.1 Random Number Generator

The simulation requires a large number of random numbers: each cell being updated needs one random integer in $\{0, \ldots, q-1\}$ and possibly a second in $[0, 1)$ for the Metropolis acceptance step. A key performance factor is therefore a good **parallel** random number generator.

[2] i.e., all simultaneously without violating causality.

The ideal design is an independent generator per thread. Given the strong time and memory constraints, we concluded that the Multiply-With-Carry (MWC) generator [144] is ideal for our application: it is fast and uses very few variables per thread. The generator state is only 64 bits, and obtaining a new pseudo-random number amounts to computing $x_{n+1} = (x_n \times a + c_n) \bmod b$, where a is the multiplier, b the base, and c_n the carry from the previous modulo operation. We adopted the CUDAMCML [145] implementation, which fixes $b = 2^{32}$ to use bit masks for the modulo operation.

To obtain independent sequences, the MWC uses different multipliers that are "good" in the sense that $a \times b - 1$ must be a safe prime. With $b = 2^{32}$ fixed, finding safe primes reduces to testing primality of $goodmult(a) \equiv prime(a \times 2^{32} - 1) \wedge prime((a \times 2^{32} - 2)/2)$. The larger a is (closer to 2^{32}), the longer the MWC period (near 2^{64} for a near the maximum), so good multipliers should be sought from $2^{32} - 1$ downward.

We limit the number of independent RNGs to $512^2/2 = 131072$, below the 150000 good multipliers provided by CUDAMCML in `safe_primes_base32.txt`. The global generator state uses 12 bytes per independent RNG, totaling 1.5MB of global memory (less than 0.15% of the GTX 280's available total). This is a good balance between independence in random number generation and memory consumption. This design decision is crucial for parallelizing the spin update function: we subdivide the lattice into 512×512 frames to give each thread an independent RNG. As the lattice grows larger, each thread performs more work. We are well below the RNG cycle even for the longest simulations.

C.3.2 Spin update

In addition to the black-and-white partition, we tile the lattice into 512×512 frames (Fig. C.1, left), due to the limited number of independent RNGs available. A second step compresses the mapping of the four-point stencil (corresponding to a site's four neighbors) to save memory transfers. The row-column pair (i, j) is mapped to $(((i + j) \bmod 2 \times L + i)/2,\ j)$. This packs all white and black cells into contiguous memory locations, improving locality and allowing wide reads of 3 consecutive bytes (Fig. C.1, right).

Each spin is encoded in one byte, allowing simulations with $q \leq 256$ and $L^2 \leq$ available RAM. The largest simulations (in terms of memory) we performed were with $L = 32768$, $q = 45$ on the GTX 480; $L = 16384$ on the GTX 280; and $L = 32768$ on the GTX 470.

We do not use shared memory, as its use did not improve performance while reducing code readability. Texture memory was not used for the same reason.

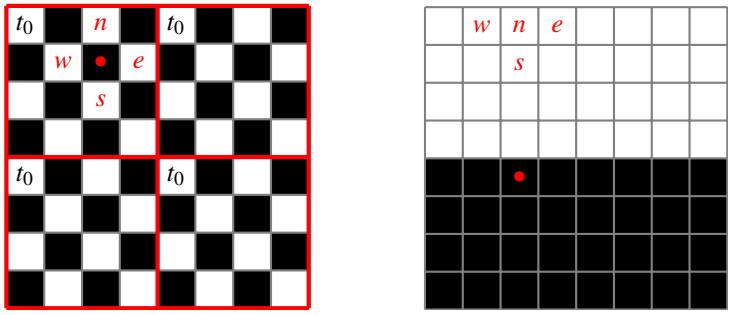


FIGURE C.1: Left: an 8×8 checkerboard tiled into 4×4 frames (marked in red). The cells updated by thread t_0 are indicated, along with the north, east, south, and west neighbors of cell •. Right: the remapped and packed checkerboard, showing where cells n, e, s, w ended up in the first half (white cells) and cell • in the second half (black cells).

C.3.3 Computation of energy, magnetization, and associated moments

During the system's evolution, two quantities are extracted periodically at specified times: the energy (Eq. 3.12) and the magnetization (Eq. 3.14). From these, the following quantities are accumulated in auxiliary variables: energy per spin $e = H/N$, e^2, e^4, magnetization m, m^2, and m^4, which are then averaged over time and over different samples (thermal noise realizations).

The `calculateCUDA` kernel computes e and m at a given instant. It partitions the cells into CUDA blocks, within each of which barrier synchronization and shared memory are easily accessible. Each block sums the energies of its cells and accumulates, in each entry i of a length-q vector, the number of spins in those cells in state i. This is done using atomic increments (*atomic adds*) to avoid race conditions. The block results are reduced in parallel using a butterfly algorithm [142] via the `sumupECUDA` and `sumupMCUDA` kernels, which leave partial energy sums and partial spin-count vectors (of order thousands of entries) to be completed on the CPU. The quantities e, e^2, e^4, m, m^2, and m^4 are accumulated on the CPU after each measurement.

Note that GPU memory consumption in this part of the code grows linearly not only with N but also with q.

C.4 Algorithm validation

To validate our CUDA code, we ran several typical simulations to measure well-known results.

TABLE C.2: Comparison between calculated and exact values of e_o, e_d, and Δm at the transition temperature for various q. Results are from curves averaged over 10 samples of linear size $L = 2048$, with equilibration and measurement times both above 5×10^5 MCS.

q	$-e_o$		$-e_d$		Δm	
	exact	calculated	exact	calculated	exact	calculated
6	1.508980...	1.51(2)	1.307516...	1.306(1)	0.677083...	0.674(2)
9	1.633167...	1.6332(5)	1.033499...	1.0334(5)	0.834019...	0.8338(4)
15	1.765905...	1.7659(2)	0.750492...	0.7509(4)	0.916693...	0.9167(3)
96	1.960306...	1.96030(3)	0.243817...	0.24382(4)	0.989247...	0.98924(2)

First, we computed the energy per spin and magnetization above and below the transition, cooling (heating) from a disordered (ordered) initial state. Table C.2 compares computed values with exact results (3.17), (3.18), and (3.20) at the exact transition temperature for each q. The agreement is excellent (note that these are direct readings from the curves in Fig. 7.16 at $T_t(q)$, not finite-size extrapolations).

We also computed the fourth-order energy cumulant [146, 147]:

$$V_L = 1 - \frac{\langle H^4 \rangle}{3\langle H^2 \rangle^2} \tag{C.1}$$

as a function of temperature for $q = 6$ and different system sizes. As well known, V_L is nearly constant far from the transition and exhibits a minimum at the pseudo-critical temperature:

$$T_c^*(L) = T_c + \frac{T_c^2 \ln(q e_o^2/e_d^2)}{e_d - e_o} \frac{1}{L^d} \tag{C.2}$$

where the minimum value, within the double-Gaussian approximation [146,147], is:

$$V_L^{min} = \frac{2}{3} - \frac{1}{3}\left[\frac{(e_d - e_o)(e_d + e_o)}{2 e_d e_o}\right]^2 + O(L^{-d}) \tag{C.3}$$

Figure C.2a shows $T_c^*(L)$ vs. $1/L^2$ for $q = 6$. The extrapolated value $T_c^*(L \to \infty) = 0.8078 \pm 0.0002$ agrees with the exact value $T_c = 0.8076068\ldots$ to within 0.025%. The extrapolated minimum value $V_L^{min}(L \to \infty) \approx 0.658 \pm 0.001$ agrees with the double-Gaussian prediction $V_L^{min} \approx 0.659774\ldots$.

Obtaining reliable cumulant measurements with single-spin-flip MC algorithms is difficult, since the system must be allowed to jump back and forth

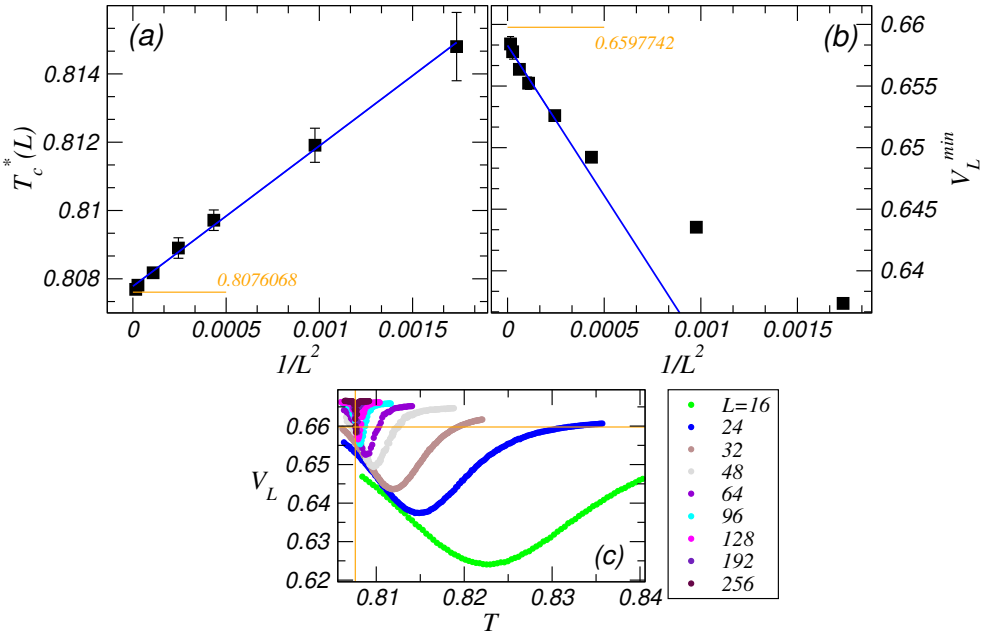


FIGURE C.2: Finite-size scaling of the fourth-order cumulant for $q = 6$. Bottom panel: V_L as a function of temperature for different system sizes (averages over 300–400 samples for the smallest sizes, 50 and 20 for $L = 128$ and $L = 256$). Orange lines indicate the analytically predicted minimum location in the thermodynamic limit. (a) Pseudo-critical temperature T_c^* vs. $1/L^2$. (b) V_L^{min} vs. $1/L^2$. Solid lines: linear extrapolations to $1/L \to 0$. Analytic results for T_c and V_{min} shown in orange.

across the energetic barrier between the two phases multiple times. For $q = 6$ and $L = 256$, simulation times of order 10^8 MCS per temperature are needed.

C.5 Algorithm performance

We profile the code using CUDA profiling tools. A profiling run for $q = 9$, $N = 2048 \times 2048$, sweeping $T \in [0.721200, 0.721347]$ in steps $\delta T = 10^{-5}$ with $t_{\text{tran}} = 10^5$ MCS, $t_{\max} = 10^4$ MCS, $\delta t = 500$ MCS, produced a 2.9 GB log file in a 12.6-hour computation. The profile confirms that approximately 32 million calls are made to `updateCUDA` and only a few thousand to the other three kernels; thus `updateCUDA` is the sole relevant target for performance optimization. Memory transfers between host and device are infrequent, which is welcome given the limited CPU-GPU bandwidth.

For the performance analysis we varied L from 512 to 32768 in powers of two, measuring the average execution time per spin flip (*spin flip time* in ns). We compared the three GPU platforms against a sequential CPU version compiled on an Intel Core 2 Duo (E8400, Q1 2008) using GCC 4.4.5 with aggressive optimization flags (`-O3 -ffast-math -march=native -funroll-loops`). We also varied $q \in \{6, 8, 9, 12, 15, 24, 48, 96, 192\}$ and found no significant performance variation with q.

Figure C.3 shows that the CPU version runs at a flat ~ 22.8 ns, independent of system size. The GPU versions show variation with L:

- GTX 280: spin flip times $[0.48, 0.54]$ ns — speedup $47\times$ to $42\times$.
- GTX 470: $[0.21, 0.30]$ ns — speedup $108\times$ to $76\times$.
- GTX 480: $[0.18, 0.24]$ ns — speedup $126\times$ to $95\times$.
- GTX 480 (CC 2.0 optimized[3]): 0.147 ns — speedup $155\times$.

Even modern CPU architectures such as Nehalem (X5550, Q1 2009) only reduce the CPU spin flip time by about 2 ns; the Intel C++ compiler (ICC) offers no further improvement.

The variation of spin flip time with L for GPU cards arises from two competing factors in the update kernel loop. One factor decreases with L: since there is one RNG per thread, global memory is read once at the beginning and written once at the end, so as L increases this fixed latency is amortized over more sites.

[3] 1024 threads per block, L1 cache disabled for marginal performance improvement.

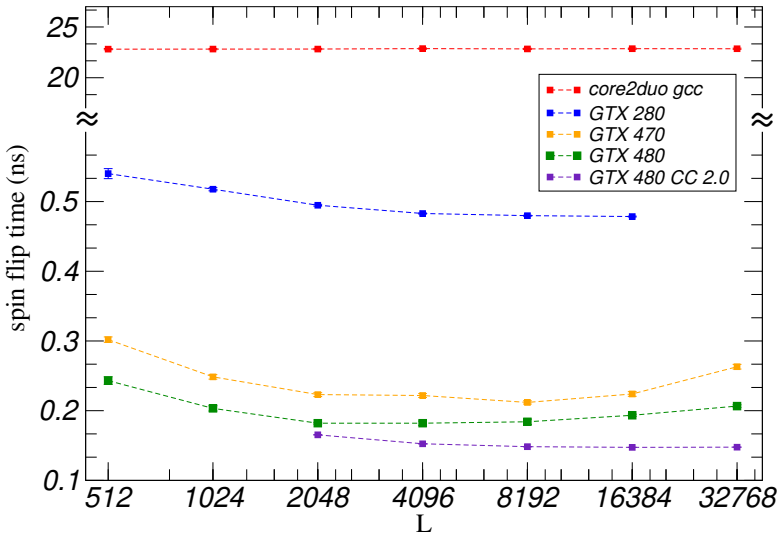


FIGURE C.3: Spin flip time (ns) as a function of linear lattice size L, for an Intel Core 2 Duo E8400@3.0GHz CPU and NVIDIA GTX 280, GTX 470, and GTX 480 GPUs. Averages over 400 GPU samples and 60 CPU samples. Error bars are smaller than symbol size.

The other factor increases with L: the inherent loop overhead (comparisons and branches), which for $L = 32768$ loops up to 4096 times.

Testing 256×256 and 1024×1024 frames instead of 512×512, we find a 25% performance penalty and a 2% gain, respectively. This confirms that the 512×512 frame size is a good compromise between RNG memory consumption and code speed.

A complete end-to-end benchmark with $q = 9$, $L = 1024$, 3 samples, $T \in [0.71, 0.73]$, $\delta T = 0.002$, $t_{\text{tran}} = 2000$, $t_{\max} = 8000$, $\delta t = 50$ gives 193 s on the GTX 280 versus 8115 s on the Intel Core 2, a global speedup of $42\times$ — consistent with the kernel-level measurement.

To our knowledge, this is the first GPU implementation of the q-state Potts model, so no direct performance comparison is possible. For context: Preis et al. [134, 135] achieved 0.12 ns/flip for the 2D/3D Ising model using multi-spin coding on a GT200; Weigel [148] reached 0.034 ns/flip using a multi-hit technique ($k = 100$ re-updates per cell); Belletti et al. [136] simulated a Heisenberg spin glass with floating-point spins at 0.67 ns/flip on GF100; a GPU parallelization of the Cellular Potts Model achieved $\sim 80\times$ speedup [149]. More recently, Weigel [150] reported 0.18 ns/flip for the 2D Heisenberg model ($1029\times$ speedup) and 2.3 ps/flip for an Edwards-Anderson spin glass with multi-spin updates ($80\times$ speedup), both on GF200 architecture.

C.6 Appendix summary

We implemented a CUDA-based Monte Carlo algorithm running in parallel on GPUs to simulate the statistical mechanics of the q-state Potts model.

The code achieves speedups (compared to an optimized serial CPU implementation) of $42\times$ on the GTX 280 up to $155\times$ on the GTX 480, with average spin flip times of 0.54 ns and 0.147 ns respectively. These times are of the same order as recent implementations for the simpler Ising model, obtained without resorting to sophisticated techniques such as multi-spin coding.

Beyond raw speedup, the algorithm can simulate very large systems in short times: for example, $\sim 10^9$ spins with an average time per MCS of 0.15 s. This performance is practically independent of q. The keys to reaching these times are: an independent RNG per thread that is fast and uses few registers; a frame scheme that increases the computation performed per thread while bounding the number of independent RNGs needed; and cell packing mappings that order memory accesses.

The availability of high-speed simulations for sufficiently large system sizes allowed us to study the problem of metastability in the Potts model based on Binder's criterion, as presented in Chapter 7.

While this implementation was developed for a two-dimensional model with nearest-neighbor interactions and a checkerboard update scheme, generalization to three-dimensional and/or longer-range interaction systems is straightforward by adjusting some aspects. For 3D, the checkerboard scheme defining two independent sublattices persists, but the cell packing scheme must be rewritten. For 2D with first- and second-neighbor interactions, nine independent sublattices arise instead of two. Both generalizations can be combined directly.

As noted in Chapter 3, beyond its theoretical interest the q-state Potts model is widely used to simulate the dynamics of a variety of systems (see Section 3.2). The present GPU implementation, or simple modifications of it, may prove useful for some of these applications. Moreover, the ability to simulate larger sizes and obtain results faster can be welcome in the statistical physics community.

We adhere to the practice of publishing code [151], following the approach of [134, 135, 152], believing that it will benefit from community debugging and development and may be useful to others. Our CUDA code is freely available under the GNU GPL 3.0 license at [153].

References

Bibliography

[1] E. E. Ferrero, J. P. De Francesco, N. Wolovick, and S. A. Cannas. "q-state Potts model metastability study using optimized GPU-based Monte Carlo algorithms". arXiv:1101.0876 · 2011.

[2] C. Anteneodo, E. E Ferrero, and S. A. Cannas. "Short-time dynamics of finite-size mean-field systems". *Journal of Statistical Mechanics: Theory and Experiment* · 2010, P07026 · 2010.

[3] E. S. Loscar, E. E. Ferrero, T. S. Grigera, and S. A Cannas. "Nonequilibrium characterization of spinodal points using short time dynamics". *Jour. Chem. Phys.* · 131, 024120 · 2009.

[4] E. E. Ferrero and S. A Cannas. "Long-term ordering kinetics of the two-dimensional q-state Potts model". *Phys. Rev. E* · 76, 031108 · 2007.

[5] M. Ibañez de Berganza, E. E. Ferrero, S. A. Cannas, V. Loreto, and A. Petri. "Phase separation of the Potts model in the square lattice". *Eur. Phys. J. Special Topics* · 143, 273 · 2007.

[6] P. Ehrenfest. "Phase changes in the ordinary and extended sense classified according to the corresponding singularities of the thermodynamic potential". *Proc. Acad. Sci., Amsterdam* · 36, 147 · 1933.

[7] P. M. Chaikin and T. C. Lubensky. *Principles of Condensed Matter Physics*. Cambridge University Press · 2000.

[8] N. Goldenfeld. *Lectures on Phase Transitions and the Renormalization Group*. Addison-Wesley Publishing Company · 1992.

[9] J. J. Binney, N. J. Dowrick, A. J. Fisher, and M. E. J. Newman. *The Theory of Critical Phenomena*. Oxford University Press, New York · 1992.

[10] P. G. Debenedetti. *Metastable Liquids*. Princeton University Press · 1996.

[11] K. Binder. "Theory of first order phase transitions". *Rep. Prog. Phys.* · 50, 783 · 1987.

[12] K. Binder. "Time-Dependent Ginzburg-Landau Theory of Nonequilibrium Relaxation". *Phys. Rev. B* · 8, 3423 · 1973.

[13] R. J. Glauber. "Time-dependent statistics of the Ising model". *J. Math. Phys.* · 4, 294 · 1963.

[14] K. Kawasaki. "Kinetics of Ising models". In *Phase Transitions and Critical Phenomena, vol. 2* · page 443. New York: Academic · 1972.

[15] K. Binder and H. Müller-Krumbhaar. "Investigation of metastable states and nucleation in the kinetic Ising model". *Phys. Rev. B* · 9, 2328 · 1974.

[16] W. Paul, D. W. Heermann, and K. Binder. "Relaxation of metastable states in finite mean-field kinetic Ising systems". *Journal of Physics A: Mathematical and General* · 22, 3325 · 1989.

[17] K. Binder. "Double-well thermodynamic potentials and spinodal curves: how real are they?". *Philos. Mag. Lett.* · 87, 799 · 2007.

[18] W. Kauzmann. "The nature of the glassy state and the behavior of liquids at low temperatures". *Chem. Rev.* · 43, 219 · 1948.

[19] A. Z. Patashinskii and B. I. Shumilo. "Theory of relaxation of metastable states". *Sov. Phys. JEPT* · 50, 712 · 1979.

[20] A. Z. Patashinskii and B. I. Shumilo. "Metastable systems near the instability region". *Sov. Phys. Solid State* · 22, 655 · 1980.

[21] S. B. Kiselev and J. F. Ely. "Curvature effect on the physical boundary of metastable states in liquids". *Physica A* · 299, 357 · 2001.

[22] D.W. Herrmann, W. Klein, and D. Stauffer. "Spinodals in a Long-Range Interaction System". *Phys. Rev. Lett.* · 49, 1262 · 1982.

[23] L. A. Fernández, J. J. Ruiz-Lorenzo, M. P. Lombardo, and A. Tarancón. "Weak first order transitions. The two-dimensional Potts model". *Physics Letters B* · 277, 485 · 1992.

[24] J. D. Gunton and M. C. Yalabik. "Renormalization-group analysis of the mean-field theory of metastability: A spinodal fixed point". *Phys. Rev. B* · 18, 6199 · 1978.

[25] F. Y. Wu. "The Potts model". *Rev. Mod. Phys.* · 54, 235 · 1982.

[26] L. Mittag and M. J. Stephen. "Dual Transformation in Many-Component Ising Models". *J. Math. Phys.* · 12, 441 · 1971.

[27] W. Klein. "Percolation, Droplet Models, and Spinodal Points". *Phys. Rev. Lett.* · 47, 1569 · 1981.

[28] R. B. Potts. "Some generalized order-disorder transformations". *Proc. Camb. Phill. Soc.* · 48, 106 · 1952.

[29] E. Ising. "Beitrag zur Theorie des Ferromagnetismus". *Z. Phys.* · 21, 613 · 1925.

[30] J. Ashkin and E. Teller. "Statistics of Two-Dimensional Lattices with Four Components". *Phys. Rev.* · 64, 178 · 1943.

[31] T. Kihara, Y. Midzuno, and T. Shizume. "Statistics of Two-Dimensional Lattices with Many Components". *J. Phys. Soc. Japan* · 9, 681 · 1954.

[32] R. J. Baxter. "Potts model at the critical temperature". *J. Phys. C* · 6, L445 · 1973.

[33] R. J. Baxter. "Corner Transfer Matrices of the Eight-Vertex Model". *J. Stat. Phys.* · 15, 485 · 1976.

[34] H. A. Kramers and G. H. Wannier. "Statistics of the Two-Dimensional Ferromagnet. Part I". *Phys. Rev.* · 60, 252 · 1941.

[35] R. J. Baxter. "Derivation of the Order Parameter of the Chiral Potts Model". *Phys. Rev. Lett.* · 94, 130602 · 2005.

[36] D. J. A. Welsh and C. Merino. "The Potts model and the Tutte polynomial". *J. Math. Phys.* · 41, 1127 · 2000.

[37] S. Murthy, S. Challa, P. Landau, and K. Binder. "Finite-size effects at temperature-driven first-order transitions". *Phys. Rev. B* · 34, 1841 · 1986.

[38] R. J. Baxter. "Magnetisation discontinuity of the two-dimensional Potts model". *J. Phys. A* · 15, 3329 · 1982.

[39] F. Y. Wu. *Exactly Solved Models: A Journey In Statistical Mechanics*. World Scientific Publishing Company · 2009.

[40] S. Alexander. "Lattice gas transition of He on Grafoil. A continuous transition with cubic terms". *Phys. Lett. A* · 54, 353 · 1975.

[41] E. Domany and E. K. Riedel. "Phase Transitions in Two-Dimensional Systems". *J. Appl. Phys.* · 42, 1315 · 1978.

[42] A. N. Berker, S. Ostlund, and F. A. Putnam. "Renormalization-group treatment of a Potts lattice gas for krypton adsorbed onto graphite". *Phys. Rev. B* · 17, 3650 · 1978.

[43] D. Mukamel, M. E. Fisher, and E. Domany. "Magnetization of Cubic Ferromagnets and the Three-Component Potts Model". *Phys. Rev. Lett.* · 37, 565 · 1976.

[44] B. Barbara, M. F. Rossignol, and P. Bak. "First-order transitions and tricritical points in DyAl 2 : A realisation of the three-state Potts model". *Journal of Physics C: Solid State Physics* · 11, L183 · 1978.

[45] A. Aharony, K. A. Müller, and W. Berlinger. "Trigonal-to-Tetragonal Transition in Stressed SrTiO3: A Realization of the Three-State Potts Model". *Phys Rev. Lett.* · 38, 33 · 1977.

[46] B. Cerruti and E. Vives. "Statistics of microstructure formation in structural transitions studied using a random-field Potts model with dipolar-like interactions". *Journal of Statistical Mechanics: Theory and Experiment* · 2009, P05009 · 2009.

[47] J. Vinals and M. Grant. "Role of activated processes and boundary conditions in the domain growth of the Potts model". *Phys. Rev. B* · 36, 7036 · 1987.

[48] G. S. Grest, M. P. Anderson, and D. J. Srolovitz. "Domain-growth kinetics for the Q-state Potts model in two and three dimensions". *Phys. Rev. B* · 38, 4752 · 1988.

[49] C. Sire and S. Majumdar. "Coarsening in the q-state Potts model and the Ising model with globally conserved magnetization". *Phys. Rev. E* · 52, 244 · 1995.

[50] M. P. O. Loureiro, J. J. Arenzon, L. F. Cugliandolo, and A. Sicilia. "Curvature-driven coarsening in the two-dimensional Potts model". *Phys. Rev. E* · 81, 021129 · 2010.

[51] J. Meunier and A. Morel. "Condensation and metastability in the 2D Potts model". *Eur. Phys. J. B* · 13, 341 · 2000.

[52] S. Rutkevich. "Monte Carlo Simulation of Nucleation in the Two-Dimensional Potts Model". *Int. Jour. Mod. Phys.* · 13, 495 · 2002.

[53] B. Bauer, E. Gull, S. Trebst, M. Troyer, and D. A. Huse. "Optimized broad-histogram simulations for strong first-order phase transitions: droplet transitions in the large-Q Potts model". *Journal of Statistical Mechanics: Theory and Experiment* · 2010, P01020 · 2010.

[54] A. J. Guttmann and I. G. Enting. "The phase transition of the 3-dimensional 3-state potts model". *Nuclear Physics B - Proceedings Supplements* · 17, 328 · 1990.

[55] H. Meyer-Ortmanns. "Phase transitions in quantum chromodynamics". *Rev. Mod. Phys.* · 68, 473 · 1996.

[56] F. Karsch and S. Stickan. "The three-dimensional, three-state Potts model in an external field". *Physics Letters B* · 488, 319 · 2000.

[57] H. Arkin and T. Çelik. "Study of phase conversition in 3D q=3 potts model". *Inter. J. Mod. Phys. C* · 11, 1313 · 2000.

[58] A. Velytsky, B. Berg, and U. Heller. "Dynamics of the 2d Potts model phase transition". *Nucl. Phys. B (Proc. Suppl.)* · 119, 861 · 2003.

[59] S. Kim, P. de Forcrand, S. Kratochvila, and T. Takaishi. "The 3-state Potts model as a heavy quark finite density laboratory". *PoS* · LAT2005, 166 · 2006.

[60] A. Bazavov, B. A. Berg, and S. Dubey. "Phase transition properties of 3D Potts models". *Nuclear Physics B* · 802, 421 – 434 · 2008.

[61] J. Langelage and O. Philipsen. "The deconfinement transition of finite density QCD with heavy quarks from strong coupling series". *Journal of High Energy Physics* · 2010, 1 · 2010.

[62] C. Bonati and M. D'Elia. "Three-dimensional, three-state Potts model in a negative external field". *Phys. Rev. D* · 82, 114515 · 2010.

[63] J. A. Glazier and D. Weaire. "The kinetics of cellular patterns". *J. Phys: Condens. Matter* · 4, 1867 · 1992.

[64] S. Sanyal and J. A. Glazier. "Viscous instabilities in flowing foams: A Cellular Potts Model approach". *Journal of Statistical Mechanics: Theory and Experiment* · 2006, P10008 · 2006.

[65] K. S. Korolev, M. Avlund, O. Hallatschek, and D. R. Nelson. "Genetic demixing and evolution in linear stepping stone models". *Rev. Mod. Phys.* · 82, 1691 · 2010.

[66] F. Graner and J. A. Glazier. "Simulation of biological cell sorting using a two-dimensional extended Potts model". *Phys. Rev. Lett.* · 69, 2013 · 1992.

[67] S. Turner and J. A. Sherratt. "Intercellular Adhesion and Cancer Invasion: A Discrete Simulation Using the Extended Potts Model". *Journal of Theoretical Biology* · 216, 85 · 2002.

[68] F. Bentrem. "A Q-Ising model application for linear-time image segmentation". *Central European Journal of Physics* · 8, 689 · 2010.

[69] V. Kryzhanovsky. "Modified q-State Potts Model with Binarized Synaptic Coefficients". In *Artificial Neural Networks - ICANN 2008* · volume 5164 of *Lecture Notes in Computer Science* · page 72. Springer Berlin - Heidelberg · 2008.

[70] C. Schulze. "Potts-like Model for Ghetto Formation in Multi-Cultural Societies". *Central European Journal of Physics* · 16, 351 · 2005.

[71] V. A. Traag and J. Bruggeman. "Community detection in networks with positive and negative links". *Phys. Rev. E* · 80, 036115 · 2009.

[72] L. Cugliandolo. "Dynamics of glassy systems". In *Lecture notes in Slow Relaxation and non equilibrium dynamics in condensed matter* · Les Houches Session 77.

[73] A. J. Bray. "Theory of phase-ordering kinetics". *Advances in Physics* · 51, 481 · 2002.

[74] P. C. Hohenberg and B. I. Halperin. "Theory of dynamic critical phenomena". *Rev. Mod. Phys.* · 49, 435 · 1977.

[75] S. Allen and J. Cahn. "Microscopic theory for antiphase boundary motion and its application to antiphase domain coarsening". *Acta Metall.* · 27, 1085 · 1979.

[76] A. J. Bray. "Theory of phase-ordering kinetics". *Advances in Physics* · 43, 357 · 1994.

[77] I. Lifshitz. "Kinetics of ordering during second-order phase transitions". *Sov. Phys. JEPT* · 15, 939 · 1962.

[78] M. Grousson, G. Tarjus, and P. Viot. "Monte Carlo study of the three-dimensional Coulomb frustrated Ising ferromagnet". *Phys. Rev. E* · 64, 036109 · 2001.

[79] I. Lifshitz and V. Slyozov. "The kinetics of precipitation from supersaturated solid solutions". *J. Phys. Chem. Solids* · 19, 35 · 1961.

[80] Z. W. Lai, G. F. Mazenko, and O. T. Valls. "Classes for growth kinetics problems at low temperatures". *Phys. Rev. B* · 37, 9481 · 1988.

[81] K. Binder and W. Kob. *Glassy Materials and Disorder Solids*. World Scientific Publishing Company · 2005.

[82] P. A. Rikvold and B. M. Gorman. "Recent Results on the Decay of Metastable Phases". In *Annual Reviews of Computational Physics I* · page 149. World Scientific - Singapore · 1994.

[83] Hanna Vehkamäki. *Classical Nucleation Theory in Multicomponent Systems*. Springer - Berlin · 2006.

[84] K. Binder and A. Young. "Spin glasses: Experimental facts, theoretical concepts, and open questions". *Rev. Mod. Phys.* · 58, 801 · 1986.

[85] M. E. Fisher and W. Selke. "Infinitely Many Commensurate Phases in a Simple Ising Model". *Phys. Rev. Lett.* · 44, 1502 · 1980.

[86] V. Spirin, P. L. Krapivsky, and S. Redner. "Freezing in Ising ferromagnets". *Phys. Rev. E* · 65, 016119 · 2001.

[87] J. Olejarz, P. L. Krapivsky, and S. Redner. "Zero-Temperature Freezing in Three-Dimensional Kinetic Ising Model". arXiv:1011.2903 · 2010.

[88] E. A. Goremychkin, R. Osborn, B. D. Rainford, R. T. Macaluso, D. T. Adroja, and M. Koza. "Spin-glass order induced by dynamic frustration". *Nature Physics* · 4, 766 · 2008.

[89] K. Binder and D. W. Heerman. *Monte Carlo Simulation in Statistical Physics*. Springer - Verlag · second edition edition · 1992.

[90] H. K. Janssen, B. Schaub, and B. Schmittmann. "New Universal Short-Time Scaling Behavior of Critical Relaxation Processes". *Z. Phys. B: Condens. Matter* · 73, 539 · 1989.

[91] V. V. Prudnikov, P. V. Prudnikov, I. A. Kalashnikov, and S. S. Tsirkin. "Renormalization-Group Description of Nonequilibrium Critical Short-time Relaxation Processes: A Three-Loop Approximation". *J. Exp. Theor. Phys.* · 106, 1095 · 2008.

[92] David A. Huse. "Remanent magnetization decay at the spin-glass critical point: A new dynamic critical exponent for nonequilibrium autocorrelations". *Phys. Rev. B* · 40, 304 · 1989.

[93] K. Humayun and A. J. Bray. "Non-equilibrium dynamics of the Ising model for T =¡ Tc". *Journal of Physics A: Mathematical and General* · 24, 1915 · 1991.

[94] L. Schuelke and B. Zheng. "The short-time Dynamics of the Critical Potts Model". *Phys. Lett. A* · 204, 295 · 1995.

[95] B. Zheng. "Monte Carlo Simulations of Short-time Critical Dynamics". *International Journal of Modern Physcis B* · 12, 1419 · 1998.

[96] E. V. Albano, M. A. Bab, G. Baglietto, R. A. Borzi, T. S. Grigera, E. S. Loscar, D. E. Rodríguez, M. L. Rubio Puzzo, and G. P. Saracco. "Study of phase transitions from short-time non-equilibrium behaviour". *Reports on Progress in Physics* · 74, 026501 · 2011.

[97] B. Zheng. "Numerical Simulations of Critical Dynamics far from Equilibrium". In *in Computer simulation studies in condensed-matter physics* · page 25. Springer, New York · 2006.

[98] L. Schuelke and B. Zheng. "Determination of the Critical Point and Exponents from short-time Dynamics". *Phys. Lett. A* · 215, 81 · 1996.

[99] Z. B. Li, L. Schülke, and B. Zheng. "Dynamic Monte Carlo Measurement of Critical Exponents". *Phys. Rev. Lett.* · 74, 3396 · 1995.

[100] P. Hanggi, H. Grabert, P. Talkner, and H. Thomas. "Bistable systems: Master equation versus Fokker-Planck modeling". *Phys. Rev. A* · 29, 371 · 1984.

[101] M. A. Muñoz and P. L. Garrido. "A test for two Fokker-Planck modellings of a master equation". *Journal of Physics A: Mathematical and General* · 28, 2637 · 1995.

[102] A. Pikovsky and S. Ruffo. "Finite-size effects in a population of interacting oscillators". *Phys. Rev. E* · 59, 1633 · 1999.

[103] F. T. Arecchi and A. Politi. "Generalized Fokker-Planck equation for a nonlinear Brownian motion with fluctuations in the control parameter". *Optics Communications* · 29, 361 · 1979.

[104] T. Mori, S. Miyashita, and P. A. Rikvold. "Asymptotic forms and scaling properties of the relaxation time near threshold points in spinodal-type dynamical phase transitions". *Phys. Rev. E* · 81, 011135 · 2010.

[105] H. Risken. *The Fokker-Planck Equation:Methods of Solutions and Applications*. Springer, Berlin · 1984.

[106] K. Binder. "Static and Dynamic Critical Phenomena of the Two-Dimensional q-State Potts Model". *J. Stat. Phys.* · 24, 69 · 1981.

[107] A. Petri, M. Ibañez de Berganza, and V. Loreto. "Ordering dynamics in the presence of multiple phases". *Philosophical Magazine* · 88, 3931 · 2008.

[108] E. E. Ferrero. "Metaestabilidad en el modelo de Potts de q estados". Master's thesis · Universidad Nacional de Córdoba, Argentina · 2005.

[109] L. Schuelke and B. Zheng. "Dynamical approach to weak first-order phase transitions". *Phys. Rev. E* · 62, 7482 · 2000.

[110] P. A. Pearce and R. B. Griffiths. "Potts model in the many-component limit". *Journal of Physics A: Mathematical and General* · 13, 2143 · 1980.

[111] S. A. Safran. "Domain Growth of Degenerate Phases". *Phys. Rev. Lett.* · 46, 1581 · 1981.

[112] S. Sahni, D. Srolovitz, G. Grest, M. Anderson, and S. Safran. "Kinetics of ordering in two dimensions. II. Quenched systems". *Phys. Rev. B* · 28, 2705 · 1983.

[113] M. P. Anderson, D. J. Srolovitz, G. S. Grest, and P. S. Sahni. "Computer simulation of grain growth. I. Kinetics". *Acta Metallurgica* · 32, 783 · 1984.

[114] S. Kumar, J. D. Gunton, and K. K. Kaski. "Dynamical scaling in the Q state Potts model". *Phys. Rev. B* · 35, 8517 · 1987.

[115] C. Sire and S. N. Majumdar. "Correlations and Coarsening in the q-State Potts Model". *Phys. Rev. Lett.* · 74, 4321 · 1995.

[116] A. Petri. "Lattice models of disorder with order". *Braz. Journ. Phys.* · 33, 521 · 2003.

[117] M. de Oliveira, A. Petri, and T. Tomé. "Crystal vs. glass formation in lattice models with many coexisting ordered phases". *Physica A* · 342, 97 · 2004.

[118] M. Oliveira, A. Petri, and T. Tomé. "Glassy states in lattice models with many coexisting crystalline phases". *Europhys. Lett.* · 65, 20 · 2004.

[119] M. Ibañez de Berganza, V. Loreto, and A. Petri. "Phase ordering and symmetries of the Potts model". *Phylosophical Magazine* · 87, 779 · 2007.

[120] A. Bortz, M. Kalos, and J. Lebowitz. "A new algorithm for Monte Carlo simulation of Ising spin systems". *J. Comp. Phys.* · 17, 10 · 1975.

[121] M. A. Novotny. "Monte Carlo Algorithms with Absorbing Markov Chains: Fast Local Algorithms for Slow Dynamics". *Phys. Rev. Lett.* · 74, 1 · 1995.

[122] A. Lipowski. "Anomalous phase-ordering kinetics in the Ising model". *Physica A* · 268, 6 · 1999.

[123] V. Spirin, P. L. Krapivsky, and S. Redner. "Fate of zero-temperature Ising ferromagnets". *Phys. Rev. E* · 63, 036118 · 2001.

[124] P. Sundaramurthy and D. L. Stein. "Zero temperature dynamics of 2D and 3D Ising ferromagnets". *J. Phys. A: Math. Gen.* · 38, 349 · 2005.

[125] P. M. C. de Oliveira, C. M. Newman, V. Sidoravicious, and D. L. Stein. "Ising ferromagnet: zero temperature dynamic evolution". *J. Phys. A: Math. Gen.* · 39, 6841 · 2006.

[126] M. J. de Oliveira. "Glassy states in the stochastic Potts model". *Computer Physics Communications* · 180, 480 – 484 · 2009.

[127] E. E. Ferrero. *Videos sobre la relajación del modelo de Potts*. `http://www.famaf.unc.edu.ar/~ferrero/tesis/videos.html` · 2011.

[128] M.E. Hoffman. "Derivative polynomials, Euler polynomials, and associated integer sequences". *Electron. J. Combin.* · 6, R21 · 1999.

[129] D. Cvijovic. "Derivative polynomials and closed-form higher derivative formulae". *Applied Mathematics and Computation* · 215, 3002 · 2009.

[130] M. E. J. Newman and G. T. Barkema. *Monte Carlo Methods in Statistical Physics*. Oxford University Press - USA · 1999.

[131] K. H. Fischer and J. A. Hertz. *Spin Glasses*. 1993.

[132] W. Kob. "Supercooled liquids, the glass transition, and computer simulations". In *Slow relaxations and nonequilibrium dynamics in condensed matter* · Les Houches Session LXXVII · page 199. Springer - Berlin · 2003.

[133] L. F. Cugliandolo. "Topics in coarsening phenomena". *Physica A: Statistical Mechanics and its Applications* · 389, 4360 · 2010.

[134] B. Block, P. Virnau, and T. Preis. "Multi-GPU accelerated multi-spin Monte Carlo simulations of the 2D Ising model". *Computer Physics Communications* · 181, 1549 · 2010.

[135] T. Preis, P. Virnau, W. Paul, and J. J. Schneider. "GPU accelerated Monte Carlo simulation of the 2D and 3D Ising model". *Journal of Computational Physics* · 228, 4468 · 2009.

[136] M. Bernaschi, G. Parisi, and L. Parisi. "The Heisenberg spin glass model on GPU: myths and actual facts". arXiv:1006.2566 · 2010.

[137] K. Hawick, A. Leist, and D. Playne. "Regular Lattice and Small-World Spin Model Simulations Using CUDA and GPUs". *International Journal of Parallel Programming* · page 1 · 2010.

[138] F. Herrmann, J. Silberholz, M. Bellone, G. Guerberoff, and M. Tiglio. "Integrating post-Newtonian equations on graphics processing units". *Classical and Quantum Gravity* · 27, 032001 · 2010.

[139] R. Ginjupalli and G. Khanna. "High-Precision Numerical Simulations of Rotating Black Holes Accelerated by CUDA". arXiv:1006.0663v1 · 2010.

[140] M. Sawerwain and R. Gielerak. "GPGPU based simulations for one and two dimensional quantum walks". arXiv:1003.3779v1 · 2010.

[141] B. W. Kernigham and D. M. Ritchie. *The C Programming Language*. PRENTICE-HALL, INC. · Englewood Cliffs, NJ · 1978.

[142] D. B. Kirk and W. W. Hwu. *Programming massively parallel processors: a hands-on approach*. Morgan Kaufmann Publishers · 2010.

[143] W.H. Press et al. *Numerical Recipes in C (Second Edition)*. Cambridge University Press · 1992.

[144] G. Marsaglia. "Random Number Generators". *Journal of Modern Applied Statistical Methods* · 2, 2 · 2003.

[145] E. Alerstam, T. Svensson, and S. Andersson-Engels. *CUDAMCML User manual and implementation notes* · 2009.

[146] W. Janke. "Accurate first-order transition points from finite-size data without power-law corrections". *Phys. Rev. B* · 47, 14757 · 1993.

[147] K. Binder. "Applications of Monte Carlo methods to statistical physics". *Rep. Prog. Phys.* · 60, 487 · 1997.

[148] M. Weigel. "Simulating spin models on GPU". *Computer Physics Communications* · In Press, Corrected Proof, – · 2010.

[149] J. J. Tapia and R. M. D'Souza. "Parallelizing the Cellular Potts Model on graphics processing units". *Computer Physics Communications* · In Press, Accepted Manuscript, – · 2010.

[150] M. Weigel. "Performance potential for simulating spin models on GPU". arXiv:1101.1427 · 2011.

[151] N. Barnes. "Publish your computer code: it is good enough". *Nature* · 467, 753 · 2010.

[152] M. Weigel. *Simulating spin models on GPU site*. `http://www.cond-mat.physik.uni-mainz.de/~weigel/research/gpu-computing` · 2010.

[153] E. E. Ferrero, J. P. De Francesco, N. Wolovick, and S. A. Cannas. *q-State Potts model for CUDA site*. `http://www.famaf.unc.edu.ar/grupos/GPGPU/Potts/CUDAPotts.html` · 2010.

Acknowledgements

Many people and institutions contributed, in one way or another, to this thesis — giving it its origin, its opportunity to grow, and finally the form in which it appears here. As the author, I believe all of them are indispensable participants in this manuscript and in the journey that led to it.

First and foremost, I wish to thank Dr. Sergio A. Cannas, advisor and guide throughout my doctoral work, a master of physics in the broadest sense, and beyond that, a true friend and an extraordinary person. To Sergio: my gratitude, my affection, and my admiration.

I wish to thank Drs. José Luis Iguaín, Marisa Frechero, and Pablo Serra, the evaluators of this thesis, for the time they dedicated to critical reading, for their valuable observations and comments, and for helping to improve this manuscript. Thanks also to Lic. Nicolás Wolovick for his corrections and comments on the final appendix.

I am grateful to all the collaborators on the works that form the basis of this thesis. To Mr. Miguel Ibañez de Berganza for our long discussions about the dynamics of the Potts model; to Drs. Ernesto Loscar and Tomás Grigera for their warmth and excellence as colleagues and researchers, and especially for introducing me to Short-Time Dynamics; to Dr. Celia Anteneodo for her trust, patience, and intensive collaboration; and to my colleagues in the FaMAF GPGPU-Computing group, Juan Pablo De Francesco and Nicolás Wolovick, for embarking with us on a genuinely interdisciplinary endeavor without precedent in the field, for long hours of programming and debugging, and for their infinite patience.

Thanks also to Drs. Orlando Billoni, Alejandro Kolton, and Francisco Tamarit,

with whom I collaborated over these years on a line of work that for practical reasons did not become part of this thesis. Many thanks to the researchers and colleagues at the GTMC for countless hours of discussions and consultations, and for the camaraderie of day-to-day work.

Several institutions supported my doctoral training financially and logistically: CONICET, FaMAF, SeCyT-UNC, ANPCyT, and the many Argentine and international universities that allowed me to participate in workshops, conferences, and schools. A special acknowledgement goes to the Faculty of Mathematics, Astronomy and Physics (FaMAF) of the Universidad Nacional de Córdoba — public, free, and committed to equality — which was my second home for many years, and to which this thesis belongs as part of its heritage.

The completion of this chapter of my life would not have been possible without the daily support of friends, family, and all the people who care. A particularly heartfelt thanks goes to my partner, Vero Duprez, who supported me throughout the entire doctorate — with everything that implies — and never stopped taking care of me. Thank you, Ve.

Many colleagues shared these doctoral years with me, and their company and support have been fundamental. Thanks especially to Juan Perotti, Santiago Pighin, Marianela Carubelli, Federico Pont, Yamila Garro, Any Zwick, Axel Dente, Hernán Calvo, Eugenia Gabach, Germán Maglione, Carolina Tauro, Alejandro Ferrón, and a very heartfelt thanks to Belén Franzoni, my academic mirror throughout these years and a great friend.

To my many good friends and to the companions of everyday life — of the office, the hallways, the lunches, the football, the singing, and the activism — thank you for always being there and for creating the moments of respite that made it possible to arrive here.

Last but not least, my deepest gratitude to my parents, siblings, aunts, uncles, cousins, and grandparents, who, without always understanding exactly what I was doing, applauded and encouraged me with unwavering and unconditional confidence.

This thesis is dedicated to my grandparents — Tela, Lita, Rodolfo, and Luis.

Ezequiel Ferrero, March 2011